An Experimental Characterization of Atmospheric Turbulence Effects on Millimeter Wave Propagation in a Controlled Environment

Thesis by
Shawn JiaXiang Sheng

In Partial Fulfillment of the Requirements for the
Degree of
Doctor of Philosophy

CALIFORNIA INSTITUTE OF TECHNOLOGY
Pasadena, California

2026
Defended November 21, 2025

Shawn JiaXiang Sheng
ORCID: 0009-0004-5478-7184

ACKNOWLEDGEMENTS

A person grows a lot throughout the course of a PhD. One lesson that has really resonated with me during my time at Caltech is that it is not about the pursuit of happiness, but the happiness of pursuit — the journey is more important than the destination. Embracing this philosophy has fueled me throughout my studies. It reminds me to remain a lifelong learner, strive to be better every day, and keep pushing forward. While the journey of life continues long after a PhD, it is important to acknowledge and celebrate the achievement of reaching this milestone. I could not have reached this point without the guidance, encouragement, and support of many people.

First and foremost, I would like to express my deepest gratitude and appreciation for my PhD advisor, Prof. Azita Emami. Thank you for giving me the opportunity to work at this incredible institution and for your invaluable guidance and support. You have pushed me to do the best I can and believed in me even when I did not always believe in myself. You have taught me to be take initiative, think outside the box, tackle challenges, and inspired me to never give up.

I would like to sincerely thank the members of my thesis committee: Prof. P. P. Vaidyanathan, Prof. Charles Elachi, and Dr. Ken Cooper. Thank you for taking the time to serve on my committee and for the constructive feedback on my research. Special thank you to Ken for letting me use the W-band radar for so many years and providing invaluable technical inputs at the start of my research. I also appreciate Prof. Alireza Marandi for serving on and being the chair of my candidacy committee.

The progress of my PhD would not have been possible without the help of Dr. Omkar Pradhan. Thank you for being such a great mentor to me and for all your efforts from the very inception of this project. Your patience, kindness, and constant support have meant so much to me. You always explained complex technical concepts with clarity, and I have learned an incredible amount from you. I am truly grateful for the time you dedicated to this work.

I would like to thank all of my collaborators for their invaluable knowledge and support throughout this work. To Prof. Roni Goldshmid, thank you for the many long days we spent conducting experiments together, and for helping me navigate through and better understand the complexities of turbulence. To Dr. Simone Tanelli, thank you for your expertise and inputs in our meetings. To Dave Sar

and Dave Manzi, thank you for all of your insights and experience, which were instrumental in advancing and shaping this research.

To all of the past and present members of the MICS lab: Dr. Xavier Chen, Dr. Arian Hashemi, Dr. Saransh Sharma, Dr. Fatima Aghlmand, Dr. Benyamin Haghi, Dr. Steven Bulfer, Ting-Yu Cheng, Mohamadamin Panahandeh, Dr. Jihong Min, Shengsheng Wang, Dr. Ziyi Chang, Jahan Razavi, Dr. Loai Danial, Garrett Knuf, Chase Blanchette, Fangyao Huang, Christopher Pope, and Christine Chang. Thank you for making the MICS lab such a great place to work, and keeping the office lively and fun. I appreciate all of the great memories, group outings, and long conversations about research and life.

The support of all of the administrative professionals are immensely appreciated. Thank you to Michelle Chen, Tanya Owen, Mabby Howard, Christine Garske, Caroline Murphy, and others for helping to keep everything running smoothly.

My work would not have been possible without the collaboration of the Center for Autonomous Systems and Technologies (CAST). Thank you to Prof. Mory Gharib, Noel Esparza-Duran, Reza Nemovi, Karima Guthrie, Joshua Gurovich, and others for all of your support in my work and helping make CAST such a great research facility on campus.

I would like to thank Dr. Matthew Yao, Dr. Seola Lee, and Dr. Melinda Chan for being in Team DFA. I appreciate all of the fun times and unforgettable meme-ories from the very start of our PhD journeys. It is crazy to think all the way back to international student orientation (bless Laura Flower Kim) and how we all finally made it out of here.

Thank you to all of the members of the Caltech Badminton Club. I am grateful to have rekindled my love for badminton during my time at Caltech, and I truly appreciate all of the fun and competitive games. Having something to look forward to every Tuesday and Friday provided a much-needed balance and a welcome break from the stresses of research.

One of the main reasons I decided to pursue graduate school was for my love of teaching. Throughout my PhD, it has been my honor to have been a TA for EE45 from 2021 to 2025, as well as EE/MedE 124 in 2025. Thank you to each and every student for asking questions in office hours, attending review sessions, and writing amazing TQFR comments. Special thanks to Rahul Chawlani, Eilleen Zhang, and Yiyi Cai for nominating me for an ASCIT teaching award.

I would not have been here without the unwavering support of my family. Thank you Mom for your endless love and encouragement. You have taught me the value of hard work, perseverance, and to always try my best. I have always said the number one thing that I miss about home is my Mom's cooking, so thank you for always cooking me the most delicious food whenever I come home. Thank you Dad for teaching me patience, kindness, respect, and that you need the right tools to do the right job. Thank you to my siblings, James and Emily, for always being there to answer my call and talk about anything and everything.

Last but not least, to my partner, Scarlett. Thank you for always putting a smile on my face, believing in me, and inspiring me to be better every day. Your love and support mean the world to me, and I cannot wait to start the next chapter of our lives together.

ABSTRACT

Atmospheric turbulence significantly affects electromagnetic (EM) wave propagation, especially at millimeter-wave (mmWave) frequencies, resulting in scintillation. Developing a statistical channel model to characterize these effects is crucial for accurate prediction and mitigation across various applications. In radar and satellite systems, turbulence can degrade signal quality and reduce accuracy. As telecommunications advance toward higher EM frequencies, turbulence will significantly influence signal performance. Moreover, statistical analysis of a propagating EM wave provides a unique opportunity for the remote sensing of atmospheric turbulence dynamics. The push towards an improved understanding of the planetary boundary layer on a global scale motivates the development of next generation measurement techniques.

This thesis presents a novel approach for studying and characterizing the physical effects of atmospheric turbulence on mmWave propagation in a controlled laboratory environment. The method combines theoretical modeling and experimental validation to link meteorological parameters and turbulence dynamics to the scintillation effects on the power spectrum of a radio frequency (RF) signal. The experimental setup employs a versatile fan array wind tunnel to generate repeatable and controllable turbulent flows. A W-band (95GHz) transceiver is used to propagate EM energy through the turbulent flow, with the received signal analyzed to characterize the effects of turbulence-induced scintillation. Additional components include utility heaters for generating strong temperature gradients, a thermal screen and infrared camera to measure the temperature profile of the flow with high spatial resolution, a high-speed anemometer for turbulence spectrum characterization, and barometers and hygrometers for pressure and humidity measurements.

The effects of temperature gradients and wind speeds are shown to increase and shift the power spectrum of the RF signal across multiple turbulent scales. Meteorological and RF measurements are directly linked through an empirical model that builds upon existing theoretical frameworks to accurately determine flow dynamics based on the characteristics of the received signal. The results are shown to be consistent and repeatable across multiple days, ambient conditions, and experimental configurations. Improvements and future directions are discussed, including extending this experimental setup to practical applications and leveraging the controllability to develop more sophisticated models that advance the understanding of scintillation.

PUBLISHED CONTENT AND CONTRIBUTIONS

[1] S. Sheng, O. Pradhan, R. Goldshmid, S. Tanelli, K. Cooper, and A. Emami, "An experimental characterization of atmospheric turbulence effects on millimeter wave propagation in a controlled environment," *IEEE Transactions on Antennas and Propagation*, 2025, (Under Review),
S.S. participated in the conception of the project, theoretical analysis, simulations, design and implementation of the experimental setup, performing experiments, processing data, and writing the manuscript.

[2] S. Sheng, O. Pradhan, R. Goldshmid, K. Cooper, and A. Emami, "Experimentally characterizing millimeter wave propagation in random media using a fan array wind tunnel," in *2025 IEEE International Symposium on Antennas & Propagation and North American Radio Science Meeting*, 2025,
S.S. participated in the conception of the project, theoretical analysis, simulations, design and implementation of the experimental setup, performing experiments, processing data, and writing the manuscript.

[3] S. Sheng, O. Pradhan, K. Cooper, R. Goldshmid, and A. Emami, "Experimentally characterizing atmospheric turbulence effects on millimeterwave propagation," in *2024 IEEE International Geoscience and Remote Sensing Symposium*, 2024, pp. 6835–6838. DOI: 10.1109/IGARSS53475.2024.10640477,
S.S. participated in the conception of the project, theoretical analysis, simulations, design and implementation of the experimental setup, performing experiments, processing data, and writing the manuscript.

TABLE OF CONTENTS

LIST OF ILLUSTRATIONS

LIST OF TABLES

Chapter 1

INTRODUCTION

The application of electromagnetic (EM) waves is ubiquitous in modern society. Atmospheric effects on EM wave propagation has been studied for centuries, and developing accurate models is crucial for the design and optimization of countless applications and fundamental to the advancement of technology. This thesis presents a novel experimental setup for studying and characterizing atmospheric turbulence effect on EM wave propagation, particularly in the millimeter wave (mmWave) regime. This setup employs a programmable fan array wind tunnel (FAWT) to generate turbulent conditions in a controlled laboratory environment. The work encompasses the theoretical analysis, design, implementation, iterative refinements, and measurement results of this first-of-its-kind system.

This thesis is organized as follows. Chapter 2 provides background information on the study of atmospheric turbulence effects on mmWave propagation. It outlines the importance of accurate modeling and the associated challenges, and discusses the limitations of prior experimental studies that motivate the development of next-generation measurement techniques. The chapter also highlights the various applications that are severely impacted by atmospheric turbulence, further underscoring the need for more sophisticated modeling approaches.

Chapter 3 introduces the theoretical framework for modeling and analytically characterizing scintillation. A line-of-sight (LoS) propagation model is presented, and well-established theory for scintillation and EM wave propagation in the lower troposphere are applied in the context of the experimental setup. The modeling of turbulence across different scales is also introduced. This theoretical analysis is used to motivate the design and implementation choices of the experimental setup.

Chapter 4 details the experimental setup, describing the equipment, instruments, and components used, along with their respective benefits and drawbacks that motivated iterative improvements. The 2 core branches of the experimental setup are outlined: the EM wave aspect and the meteorological aspect. The EM wave branch focuses on the transceiver hardware used to propagate EM energy through the turbulent flow, along with supplementary components that ensure accurate beam measurement and analysis. The meteorological branch addresses the generation and

measurement of key parameters such as temperature, humidity, and wind speed. Methods for inducing temperature and humidity gradients, as well as configurations for creating different turbulent flow dynamics are highlighted. Measurement instruments and methodologies employed are summarized for the characterization of these meteorological parameters.

Chapter 5 presents the measurement results obtained from the experimental setup. The chapter begins with an overview of unsuccessful experiments, explaining why those configurations were ineffective, the lessons learned, and iterative improvements that followed. Verification of the experimental setup's ability to generate and observe scintillation is demonstrated. Then the 2 primary heater configurations are examined: heaters positioned in front of the FAWT to create a uniform temperature gradient along the propagation path of the beam, and heaters placed on the sides of the FAWT to allow for unobstructed flow. The benefits and drawbacks of each configuration are summarized, as well as the corresponding measurements results and insights gained. Comparisons are made with theory to establish an empirical model, tying together the EM wave measurement results and the meteorological measurement results. The consistency and repeatability of the experimental setup is also demonstrated.

Finally, Chapter 6 provides the conclusion, summarizing the key contributions of this thesis. It also outlines improvements and directions for future work to further advance the experimental setup described. An appendix is included of additional experiments and their measurement results, which do not alter the main conclusions of this thesis.

Chapter 2

BACKGROUND

The modeling of EM wave propagation encompasses the prediction, calculation, and analysis of how the amplitude and phase of waves evolve and interact across various media and environmental conditions. Propagation models for EM waves can be broadly catagorized into 2 domains: deterministic and stochastic. The most fundamental deterministic model is the Friis transmission formula, which calculates the received signal power for a propagating EM wave under idealized LoS conditions:

$$P_R = P_T G_R G_T \left(\frac{\lambda}{4\pi R}\right)^2 \tag{2.1}$$

where P_R and P_T are the power levels at the receiving and transmitting antennas, respectively, G_R and G_T are the gains of the receiving and transmitting antennas, respectively, λ is the wavelength, and R is the LoS propagation distance.

This basic model only provides information on the amplitude (intensity) of the propagating wave, and is only applicable in free space. In the atmosphere, interactions with molecules and other particles give rise to scattering, refraction and absorption. The Liebe mmWave propagation model (MPM) comprehensively accounts for these atmospheric effects, calculating the attenuation and delay across frequencies from 0-1000GHz [1]. This deterministic model takes meteorological parameters such as temperature (T), relative humidity (RH), pressure (P), and rainfall rate (R) as inputs, and computes the resulting complex refractivity, which can be used to determine the attenuation (Fig. 2.1) and delay (Fig. 2.2) experienced by a propagating EM wave.

While the MPM is comprehensive, its accuracy depends on precise meteorological data along the entire propagation path. Furthermore, it does not take into account random atmospheric fluctuations introduced by turbulence. Therefore, a stochastic model for characterizing the effects of turbulence is needed, which is where scintillation becomes a central consideration.

Scintillation is an important phenomenon that has been studied for many decades, and is defined as the random fluctuations in the amplitude and phase of an EM signal due to atmospheric turbulence. Shear forces in the atmosphere cause temperature

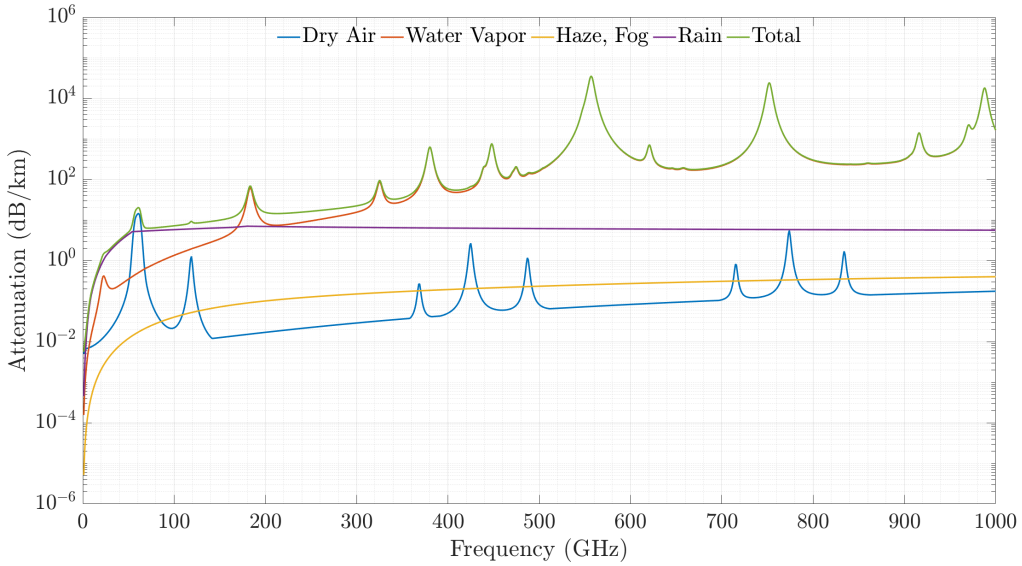

Figure 2.1: Simulated attenuation per kilometer of a propagating EM wave for different contributing factors from 0-1000GHz with T=20°C, RH=99%, P=1013.25mbar, and R=0mm/hr, using the Liebe MPM. The resonant peaks from nitrogen, oxygen, and water vapor are calculated from theory as well as empirical data.

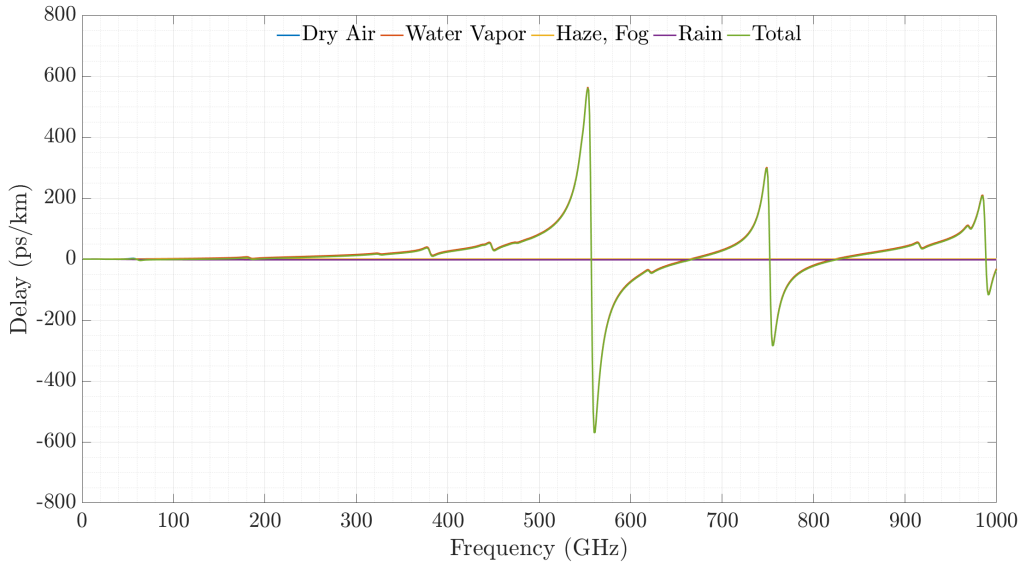

Figure 2.2: Simulated delay per kilometer of a propagating EM wave for different contributing factors from 0-1000GHz with T=20°C, RH=99%, P=1013.25mbar, and R=0mm/hr. The resonant peaks from nitrogen, oxygen, and water vapor are calculated from theory as well as empirical data.

and humidity gradients to undergo turbulent mixing, leading to random variations in the refractive index that result in scintillation. The effects of scintillation impacts a wide range of applications, motivating the study and characterization to improve modeling, prediction, and compensation methods (Fig. 2.3).

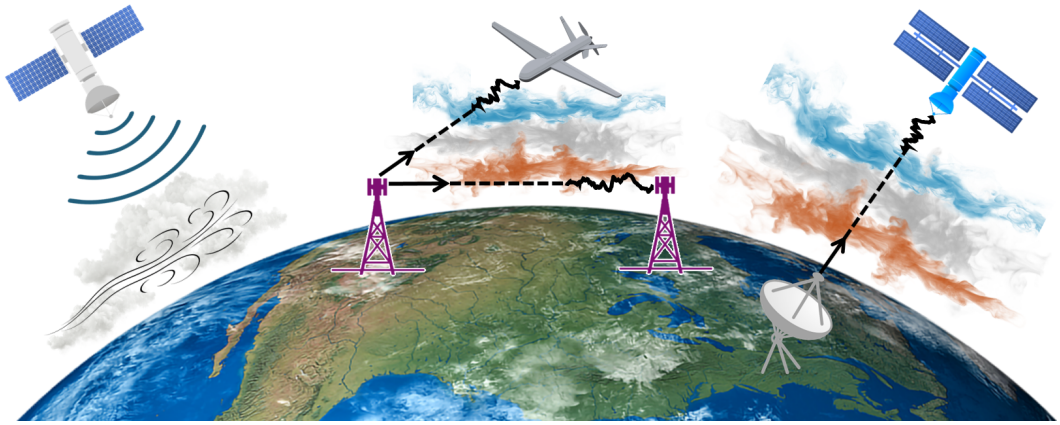

Figure 2.3: Atmospheric turbulence impacts many different applications, including remote sensing, radar systems, and terrestrial, aerial, and satellite communications.

The study of atmospheric turbulence critical, as it strongly influences local and meso-scale weather patterns [2], especially in the planetary boundary layer (PBL). The need for a deeper understanding of the PBL at a global scale has been extensively discussed in [3], motivating the development of next-generation measurement techniques. A powerful approach for remotely characterizing turbulence dynamics is to study its impact on LoS EM signals. Statistical analyses of the scintillation reveal structural and dynamical properties of turbulence within the propagation medium. Thus, the study of scintillation provides a unique opportunity for the remote sensing of atmospheric turbulence [4]. Terrestrial, aerial, and satellite communications are all affected by atmospheric turbulence. Scintillation causes the degradation in the signal quality, impacting accuracy [5]. As wireless communications advance, the push towards higher frequencies in the EM spectrum is inevitable to achieve larger bandwidths and lower latency [6] [7], [8]. These signals are high susceptible to scintillation, making them difficult to analyze and predict with the accuracy required for reliable performance, especially as communications continue to advance towards terahertz bands and free-space optical domains. These future applications emphasize the importance of analyzing, characterizing, and developing sophisticated models for scintillation.

Past experiments have focused on the measurement of atmospheric scintillation, with the simultaneous probing of meteorological parameters. These experimental setups rely on naturally occurring turbulence. Many experiments have been conducted using elevated LoS propagation paths between the islands in Hawaii at frequencies up to 40GHz [9], [10], [11], [12], [13], [14]. These studies examined time variations of the refractive index, the power density spectra and correlation functions of phase

fluctuations, as well as amplitude scintillations. From measured data, they quantified refractive index fluctuations and verified theoretical models of phase and amplitude scintillations. The experiments focused on several radio frequencies, including 9.55, 19.1, 22.2, 25.4, and 33.3 GHz, selected for their relevance to water vapor absorption, and analyzed both scintillation and fading effects. The results confirmed that higher frequencies generally exhibit stronger scintillation.

Extensive studies over 1.4km in a very flat farm land near Flatville, Illinois at frequencies of 116, 140, 173, and 230 GHz is summarized in [15], [16], [17], [18], [19], [20]. These experiments validate the theoretical models of turbulence between scintillation and meteorological measurements. These experiments measure fluctuations in mmWave signals due to atmospheric turbulence, precipitation, and fog. The meteorological measurements are near the same height as the mmWave beam at 3 locations along the path.

Experiments done along a 4.1km LoS propagation path across London at 36GHz and 110GHz are done in [21], [22], [23], [24], [25]. These measurements results occur over the span of 2 years, and collect the amplitude scintillation data at the 2 frequencies under various atmospheric conditions. Massive amounts of data to provide empirical behavior for characterizing atmospheric effects. They also use the data to derive the value of C_n^2. They compare the amplitude scintillation at these two wavelengths as well.

Amplitude and phase scintillation experiments on a 30GHz over 8.2km LoS propagation link in the Netherlands was done [26], [27], [28]. The results are compared with weak-scattering theory, and compare favorably. They also use the scintillation measurements as a proxy for the remote sensing of turbulence. They measure the meteorological parameters at a single point around midway on the propagation path.

Amplitude scintillations studied through a satellite link are explained in [29], [30], [31]. These studies present amplitude scintillation measurements from satellite communication links for prediction, link planning, mitigation, and robustness.

The previous experimental setups highlight several difficulties and challenges. First, there is imperfect *a priori* knowledge of how natural turbulence is generated. This results in very inconsistent and unpredictable conditions, which make characterization very challenging. These experiments focus on measurement, and tying together EM signal measurements with meteorological measurements, as well as verifying theory. However, the measurement process is purely passive, depending on the

natural conditions which are uncontrollable and inconsistent. The required capital to perform the experiments is also significant and requires a lot of manpower to establish the LoS propagation link. Finally, the characterization of meteorological parameters is limited to the endpoints of the transceiver, or a single point midway along the propagation path. This only provides a rough estimate of the dynamics of the entire channel, and showcases the difficulty of characterizing the meteorological parameters along the entire LoS propagation path as multiple concurrently operating *in-situ* sensors are needed. So, these reasons motivate the development of this novel experimental setup presented in this thesis.

Chapter 3

THEORETICAL ANALYSIS

Turbulence-induced scintillations in a propagating EM wave manifest as random amplitude and phase fluctuations (Fig. 3.1). In this chapter, the received signal model and associated power spectrum are introduced. The power spectrum is the primary measured quantity containing the combined effects of scintillation and system noise. Analytical expressions relating meteorological and turbulent dynamics parameters to measured amplitude and phase scintillations are also outlined.

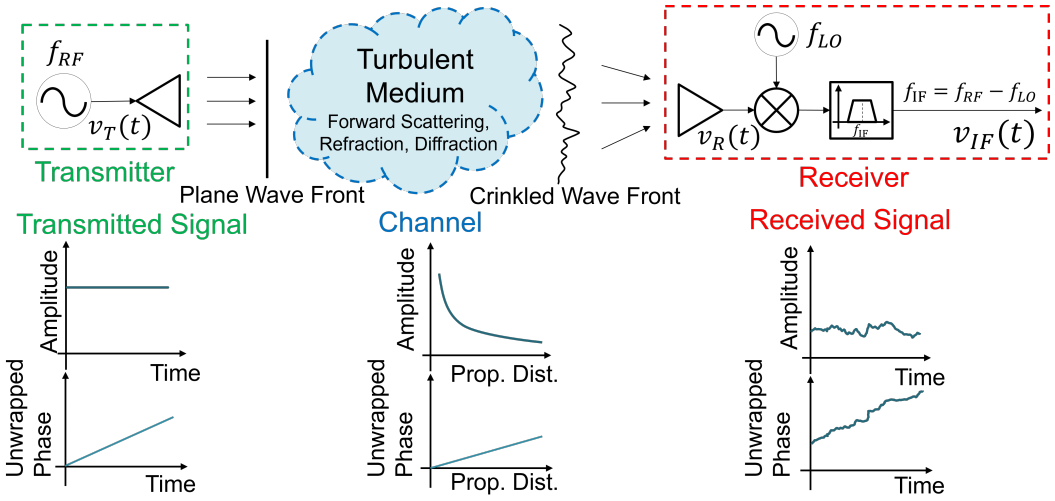

Figure 3.1: System overview to model atmospheric turbulence effects on EM wave propagation in a typical heterodyne architecture.

3.1 LoS Propagation Model for EM Scintillation

An EM signal in a LoS propagation link at the intermediate frequency (IF) output of a typical heterodyne receiver can be expressed as:

$$v_{IF}(t) = Ae^{\chi(t)}e^{j(2\pi f_{IF}t+\varphi(t)+\phi(t))} \tag{3.1}$$

where t is time, A is the amplitude of the signal without scintillation, f_{IF} is the IF frequency, $\chi(t)$ and $\varphi(t)$ are the log-amplitude and phase scintillations, respectively, and $\phi(t)$ is the system phase noise. The system phase noise is dominated by the oscillator phase noise from the frequency sources, but also includes contributions from mechanical vibrations and thermal noise. In this experiment, the impact of

$\chi(t)$ and $\varphi(t)$ on the received signal are measured and characterized. The primary frequencies of interest are close-in frequencies, which are predominantly affected by colored $(1/f)$ noise, so white noise is neglected. In addition, system amplitude noise is assumed to be minimal and is considered negligible.

3.2 Spectrum of Received Signal

In the lower troposphere, weak scattering is assumed, which implies that $\langle\chi^2\rangle << 1$ and $\langle\varphi^2\rangle << 1$ [32]. The first-order Taylor expansion can thus be applied so that:

$$v_{IF}(t) \approx A(1+\chi(t))e^{j2\pi f_{IF}t}(1+j\varphi(t))(1+j\phi(t)) \tag{3.2}$$

The auto-correlation function of the received signal is:

$$\begin{aligned} R_{IF}(\tau) &= \mathbb{E}[v_{IF}(t)v_{IF}^*(t-\tau)] \\ &= A^2 e^{j2\pi f_{IF}\tau}\mathbb{E}[(1+\chi(t))(1+\chi(t-\tau))(1+j\varphi(t)) \\ &\quad \times (1-j\varphi(t-\tau))(1+j\phi(t))(1-j\phi(t-\tau))] \end{aligned} \tag{3.3}$$

Simplifications to $R_{IF}(\tau)$ can be made by first modeling $\chi(t), \varphi(t)$, and $\phi(t)$ as zero-mean random processes. Second, cross terms of the form $\mathbb{E}[\chi(\cdot)\phi(\cdot)]$ and $\mathbb{E}[\varphi(\cdot)\phi(\cdot)]$ are zero, since the scintillation processes are uncorrelated with the system phase noise processes. Third, the log-amplitude and phase scintillation cross-terms cancel:

$$\begin{aligned} \mathbb{E}[\chi(t)\varphi(t)] - \mathbb{E}[\chi(t-\tau)\varphi(t-\tau)] = 0 \\ \mathbb{E}[\chi(t-\tau)\varphi(t)] - \mathbb{E}[\chi(t)\varphi(t-\tau)] = 0 \end{aligned} \tag{3.4}$$

The scintillation processes are assumed to be stationary, and they are real processes thus their cross-correlation function is real and even about the origin. Finally, it is assumed that higher-order moments of the form $\mathbb{E}[\chi(\cdot)\chi(\cdot)\varphi(\cdot)]$, $\mathbb{E}[\chi(\cdot)\varphi(\cdot)\varphi(\cdot)]$, and $\mathbb{E}[\chi(\cdot)\chi(\cdot)\varphi(\cdot)\varphi(\cdot)]$ are much smaller compared to the second-order moments and thus are ignored. From the above assumptions, $R_{IF}(\tau)$ can be simplified and written in terms of the auto-correlation functions of each individual process:

$$\begin{aligned} R_{IF}(\tau) = A^2 e^{j2\pi f_{IF}\tau}(1 + R_\chi(\tau) + R_\varphi(\tau) + R_\phi(\tau) \\ + R_\phi(\tau)(R_\chi(\tau) + R_\varphi(\tau))) \end{aligned} \tag{3.5}$$

Applying the Wiener-Khinchin theorem, the power spectral density (PSD) of the received IF signal is:

$$\begin{aligned} S_{IF}(f) = A^2[\delta(f-f_{IF}) + S_\chi(f-f_{IF}) + \\ S_\varphi(f-f_{IF}) + S_\phi(f-f_{IF}) + \\ S_\phi(f-f_{IF}) * (S_\chi(f-f_{IF}) + S_\varphi(f-f_{IF}))] \end{aligned} \tag{3.6}$$

The resulting PSD of the received signal is the sum of individual PSDs of the carrier, $\chi(t)$, $\varphi(t)$, and $\phi(t)$, along with a convolution term. This convolution is typically several orders of magnitude smaller than the previous terms and is therefore assumed to be effectively negligible. In order to independently observe and characterize the effects of scintillation, its intensity must dominate over the system phase noise.

3.3 Spectrum of Turbulence Induced Scintillations

For homogeneous and isotropic media in the lower troposphere, the PSD for log-amplitude and phase scintillations (χ and φ, respectively), are given by [33], [34]:

$$S_\chi(f) = 8\pi^2 R k^2 \int_{2\pi f/v}^{\infty} \frac{d\kappa \kappa \Phi_n(\kappa) F_\chi(\kappa)}{(\kappa^2 v^2 - (2\pi f)^2)^{\frac{1}{2}}} \tag{3.7}$$

$$S_\varphi(f) = 8\pi^2 R k^2 \int_{2\pi f/v}^{\infty} \frac{d\kappa \kappa \Phi_n(\kappa)}{(\kappa^2 v^2 - (2\pi f)^2)^{\frac{1}{2}}} \tag{3.8}$$

where$R$ is the LoS propagation distance, $k = 2\pi f_{RF}/c$ is the wavenumber of propagation, f_{RF} is the RF carrier frequency, c is the speed of light in a vacuum, v is the mean wind speed, and f is frequency offset from the carrier. The function $F_\chi(\kappa)$ is the amplitude-variance spectral weighting function, and for plane waves is:

$$F_\chi(\kappa) = \frac{1}{2}\left(1 - \frac{\sin(R\kappa^2/k)}{R\kappa^2/k}\right) \tag{3.9}$$

$\Phi(\kappa)$ is the refractive index wavenumber spectrum of irregularities, defined as the Fourier transform of the spatial autocorrelation function of refractive index fluctuations. Using the von Karman model, it is expressed as:

$$\Phi(\kappa) = \frac{0.033 C_n^2}{(\kappa + \kappa_0)^{11/3}} \mathcal{F}(\kappa\eta) \tag{3.10}$$

where κ is the wavenumber, $\kappa_0 = 2\pi/L_0$ is the outer scale wavenumber of turbulence, L_0 is the outer scale length of turbulence, $\mathcal{F}(\kappa\eta)$ is the dissipation function, and η is the Kolmogorov microscale. Analytical expressions for the log-amplitude and phase scintillation PSDs have been derived in the inertial subrange of turbulence:

$$S_\chi(f) = 1.096 \frac{R k^2 C_n^2 v^{\frac{5}{3}}}{(2\pi f)^{\frac{8}{3}}} \mathbb{P}\left(\frac{f}{f_F}\right) \tag{3.11}$$

$$S_\varphi(f) = 2.192 \frac{R k^2 C_n^2 v^{\frac{5}{3}}}{\left((2\pi f)^2 + \kappa_0^2 v^2\right)^{\frac{4}{3}}} \tag{3.12}$$

where $f_F = \frac{v}{2\pi}\sqrt{\frac{k}{R}}$ is the Fresnel frequency, and the function $\mathbb{P}(\xi)$ is defined as:

$$\mathbb{P}(\xi) = 1 - \frac{1.053}{\xi^2}\mathcal{I}[e^{j\xi^2}U(1/2, -4/3; -j\xi^2)] \tag{3.13}$$

where $U(a, b; z)$ is the Kummer function, and $\mathcal{I}[\cdot]$ specifies the imaginary part. These expressions were originally used to model the scintillation in the inertial subrange. However, inclusion of the dissipation region necessitates the use of numerical methods to calculate the PSDs.

3.4 Refractive Index Structure Constant Model

The gradient method is used to model C_n^2 [35]. This approach is applicable to conservative passive additives in a turbulent flow. In this context, being conservative means the additive does not change when the volume of air is shifted in space, and being passive means that it does not affect the turbulent dynamics of the flow itself. For a conservative passive additive, the structure constant can be expressed as:

$$C_n^2 = a^2 L_o^{\frac{4}{3}} \left(\frac{\partial n}{\partial z}\right)^2 \tag{3.14}$$

where $a^2 = 2.8$ is an empirically determined constant and z is altitude. For microwave frequencies less than 100GHz, the refractive index is related to meteorological parameters as [36]:

$$n = 1 + \frac{77.6 \times 10^{-6}}{T}\left(P + 4810\frac{e}{T}\right) \tag{3.15}$$

where T is the absolute temperature, P is the barometric pressure, and e is the water vapor partial pressure. However, T and e are not conservative quantities, but the potential temperature, $\theta = T(1000/P)^{0.286}$, and the specific humidity, $q = \frac{0.622e}{P - 0.378e}$, are conservative. By approximating $q \approx \frac{0.622e}{P}$, the refractive index gradient can then be calculated as:

$$\frac{\partial n}{\partial z} = -77.6 \times 10^{-6}\frac{P}{T}\left(1 + 15600\frac{q}{T}\right)\frac{1}{\theta}\frac{\partial \theta}{\partial z} + 77.6 \times 10^{-6}\frac{P}{T^2}(7800)\frac{\partial q}{\partial z} \tag{3.16}$$

In this particular scenario, P is constant due to the lack of significant elevation, so the refractive index gradient can be simplified:

$$\frac{\partial n}{\partial z} = -77.6 \times 10^{-6}\frac{P}{T^2}(1 + 15600)\frac{\partial T}{\partial z} + 77.6 \times 10^{-6}\frac{P}{T^2}(7800)\frac{\partial q}{\partial z} \tag{3.17}$$

In cases where the specific humidity gradient is assumed to be negligible, such a when no moisture is added to or removed from from the flow, the refractive index gradient can be further simplified as:

$$\frac{\partial n}{\partial z} = -77.6 \times 10^{-6} \frac{P}{T^2}(1 + 15600\frac{q}{T})\frac{\partial T}{\partial z} \tag{3.18}$$

Thus, by measuring T, P, and q, along with the temperature gradient, the refractive index gradient and C_n^2 can be calculated. In this experimental setup, the total gradient orthogonal to LoS propagation path is used, rather than only the vertical component, which is dominant in the atmospheric conditions from which this model is derived.

Applying this model to weather conditions in Pasadena (Feb 1, 2021: $T = 292K$, $RH = 43\%$, $P = 1019.64mb$), with temperature gradient data from [37] ($\partial\theta/\partial z = 0.00329K/m$), and specific humidity gradient data from the Weather Researching and Forecasting model data ($\partial q/\partial z = -2.67 \times 10^{-6} kg/(kg \cdot m)$), the expected value of C_n^2 in the lower troposphere is on the order of $10^{-14} m^{-2/3}$. The resulting values of $S_\chi(f)$ and $S_\varphi(f)$ are shown for different mean wind speeds (Fig. 3.2). The effect of the mean wind speed on the shape of the PSD is an important feature that will be characterized in future measurements.

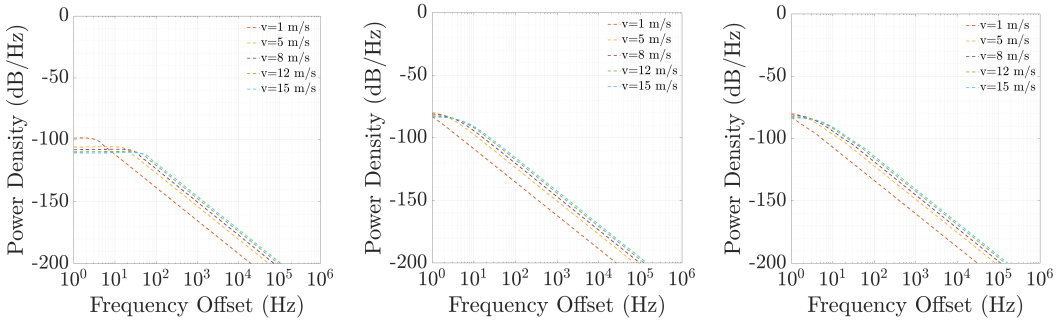

Figure 3.2: Theoretical model plots of (a) $S_\chi(f)$, (b) $S_\varphi(f)$, and (c) total ($S_\chi(f)$ + $S_\varphi(f)$) with different v. The traces demonstrate the rightward shift of the PSD for higher v due to the faster flow and higher frequency turbulent eddies. The overall area under each curve, summing to the variance, remains constant [33], [34].

For proper observation and characterization, the intensity of scintillation must dominate over system phase noise. As discussed in the following chapter, the phase noise at the receiver of a heterodyne system with a common local oscillator (LO) source is dominated by the IF oscillator. In this experiment, the IF frequency is 3GHz, so the phase noise of a 3GHz PLDRO (Microwave Dynamics PLO-3000) is considered

the dominant source of system phase noise. A comparison between the PSD of the PLDRO and scintillation motivates 2 approaches to achieve a measurement setup for more readily observable scintillation: (i) create scenarios with artificially enlarged values of C_n^2, and/or (ii) reduce the system phase noise (Fig. 3.3). The gradient method (Eq. 3.14) is analyzed to determine the required specific humidity gradient $\partial q/\partial t$, and temperature gradient $\partial T/\partial z$ required to achieve the target C_n^2 values (Fig. 3.4), while the addition of a second heterodyne stage to reduce the system phase noise is introduced in the following chapter.

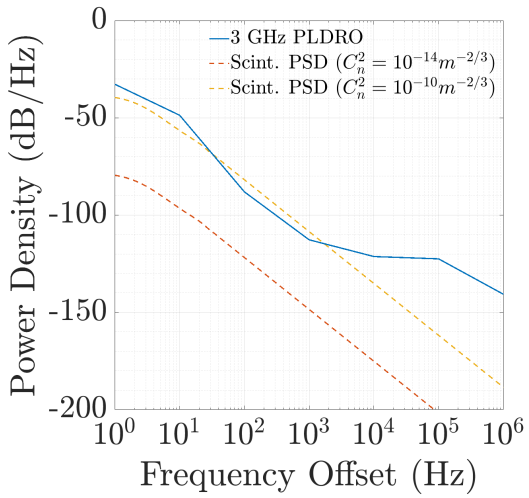

Figure 3.3: PSD of 3GHz PLDRO versus PSD of scintillation for typical C_n^2 values in the lower trophosphere ($10^{-14} m^{-2/3}$) and required artificial values to achieve comparable PSD with the PLDRO ($10^{-10} m^{-2/3}$).

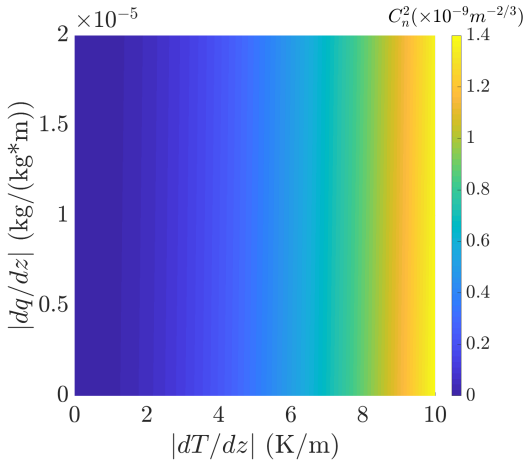

Figure 3.4: C_n^2 for different temperature and specific humidity gradients calculated using the gradient method (Eq. 3.14).

3.5 Turbulent Scales

The different scales of turbulence play a significant role and must be considered for experiments done in CAST. The refractive index spectrum of irregularities, $\Phi_n(\kappa)$ comprehensively describes the turbulent regions and scales (Fig. 3.5).

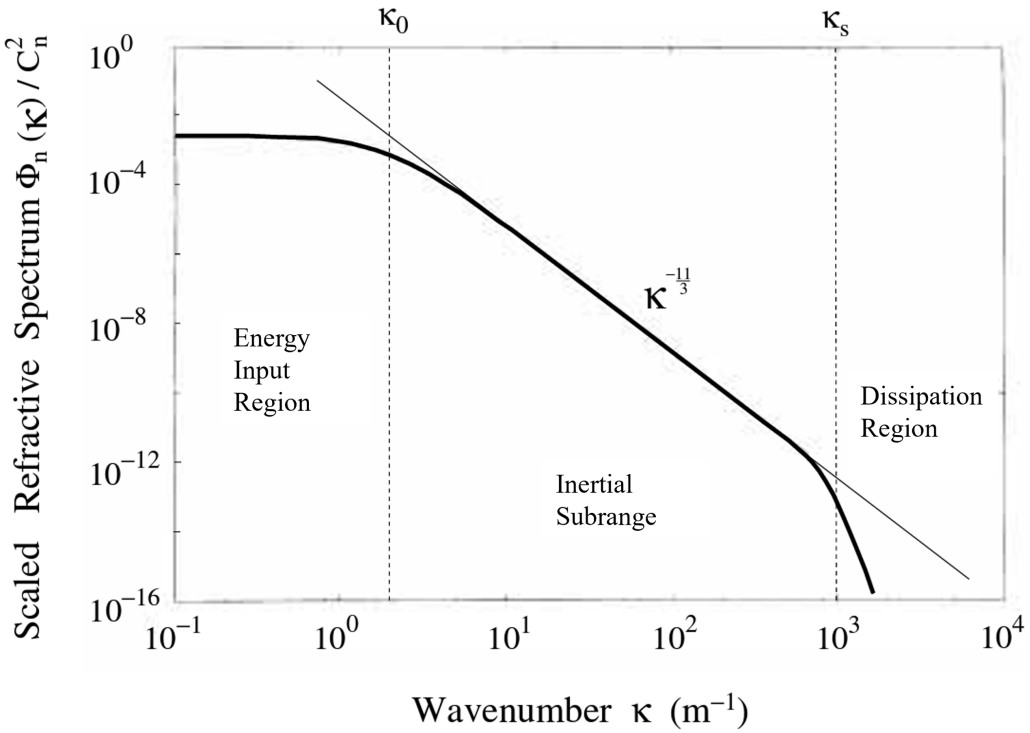

Figure 3.5: Theoretical plot of the refractive index spectrum of irregularities, illustrating the different turbulent regimes. The energy input region is where large eddies form and begin to break down. The inertial subrange is the most predictable region of turbulence, characterized by an energy cascade in which eddies progressively break down into smaller scales, governed by the Kolmogorov model. Finally, the dissipation region occurs when eddies become sufficiently small and dissipate into heat due to viscous forces, modeled as an exponential dropoff in the spectrum [32].

For velocity fluctuations, a model spectrum is used [38]:

$$E(\kappa_v) = C\varepsilon^{2/3}\kappa_v^{-5/3} f_L(\kappa_v L) f_\eta(\kappa_v \eta) \tag{3.19}$$

where κ_v is the velocity wavenumber, C is an empirical constant with a value of 0.5 for 1-dimensional analyses, ε is the energy dissipation rate, f_L and f_η are specified non-dimensional functions specifying the shape of the energy input and dissipation regions, respectively, L is energy input region length scale, and η is the Kolmogorov length scale. The velocity energy spectrum exhibits similar turbulent regions as $\Phi_n(\kappa)$ (Fig. 3.6).

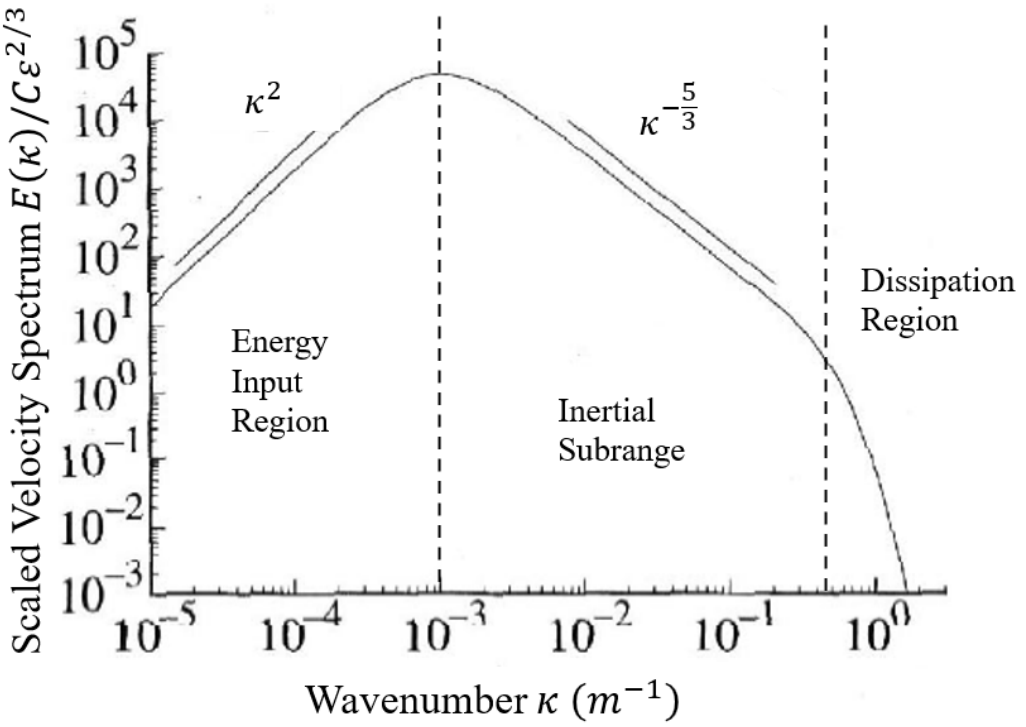

Figure 3.6: Model spectrum for velocity fluctuations showing the different scales of turbulence. Similar to Fig. 3.5, the key difference is that this model is for velocity fluctuations, which is a vector, while the spectrum for refractive index is for a scalar.

The model for the velocity dissipation function is:

$$f_\eta(\kappa_v \eta) = e^{-\beta \kappa_v \eta} \tag{3.20}$$

Several experiments have empirically determined a value of $\beta = 5.2$. For refractive index, which is a passive scalar, the turbulent regions mirror those of velocity. The energy input region is modeled by the Von Karman spectrum. The inertial subrange follows a power law with slope of $-11/3$, and the dissipation region is similarly represented by an exponential dropoff:

$$\mathcal{F}(\kappa\eta) = e^{-\alpha \kappa \eta} \tag{3.21}$$

The primary difference between the turbulent spectra of velocity and a passive scalar, such as refractive index, lies in the transition region between the inertial subrange and dissipation region. This transition is captured by the Schmidt number, defined as the ratio of kinematic viscosity ν to mass diffusivity D. For temperature, Hill

developed an empirical model which incorporates these difference and validated it using optical measurements [32]:

$$\mathcal{F}(x) = [1 + 0.70937x + 2.8235x^2 - 0.28086x^3 + 0.08277x^4]e^{-1.1090x} \quad (3.22)$$

In this work, the simplified model for the dissipation region is used (Eq. 3.21), and the parameter α is kept as an empirically determined constant. The effect of energy redistribution at the intersection of the inertial subrange and dissipation region is assumed to be negligible. While future experiments can investigate this phenomenon in more detail, the preliminary measurement results presented here are not sensitive enough to resolve these differences.

The theoretical analysis presented in this chapter informed the design and implementation choices of the experimental setup in the following chapter, guiding iterative improvements that enabled observable scintillation, along with accurate characterization and modeling.

Chapter 4

EXPERIMENTAL SETUP

This chapter describes the experimental setup conducted in CAST, outlining the components and devices used to establish the environment. It also details the evolution of various experimental techniques, emphasizing the benefits, drawbacks, and iterative improvements made throughout the process. The overall setup and measurement methodology are divided into 2 parts: transceiver measurements and meteorological measurements (Fig. 4.1).

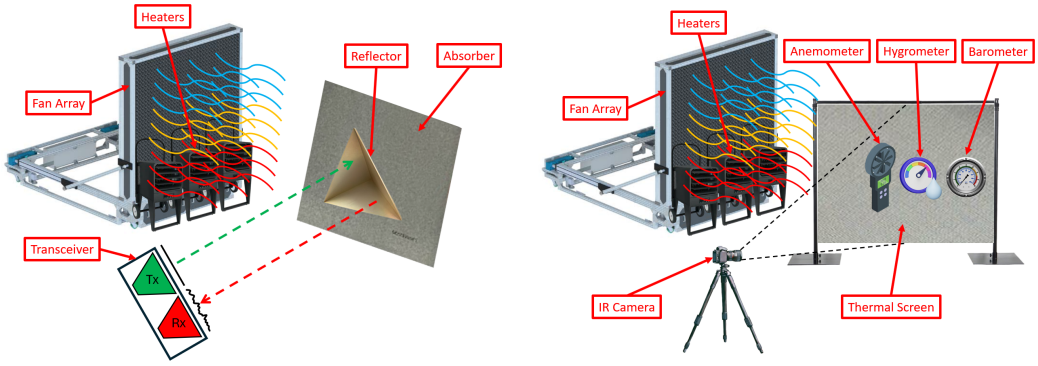

(a) (b)

Figure 4.1: Overview of the experimental setup in CAST for studying atmospheric turbulence effects on mmWave propagation in a controlled laboratory environment. The experiment is divided into (a) transceiver measurements, and (b) meteorological measurements, which are performed sequentially rather than concurrently to ensure that no obstructions interfere with the LoS propagation path of the EM beam.

4.1 Fan Array Wind Tunnel

The CAST FAWT consists of an array of 36x36 individually programmable dual-fan units (Fig. 4.2). Each unit consists of 2 counter-rotating fans that, along with a honeycomb mesh, create a swirl-free flow under uniform conditions. The fan units can be programmed to generate spatiotemporally varying wind flows, with the fan intensity set by a corresponding duty cycle ranging from 0-100% achieving maximum wind speeds up to 15m/s. Each fan unit is 80x80mm, and the total array dimensions are 2.88x2.88m. The overall facility is 15.2x9.1x12.2m high.

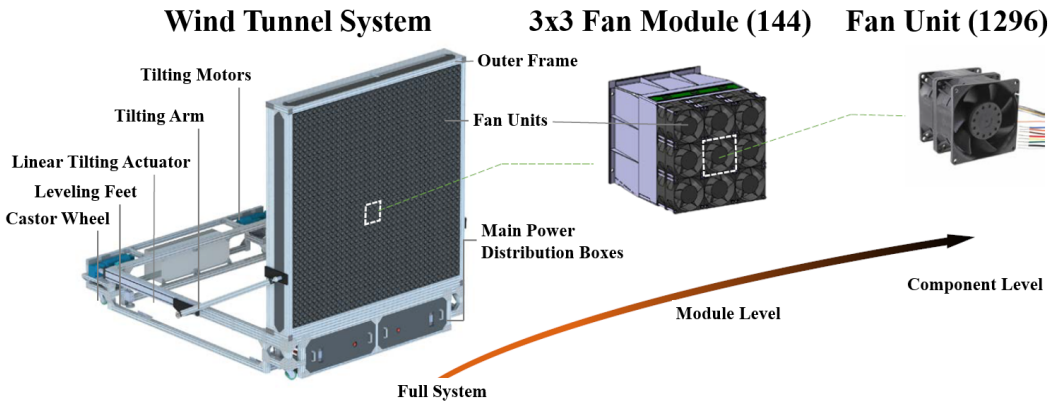

Figure 4.2: Overview of the CAST FAWT. The FAWT consists of an array of 36x36 individually programmable dual-fan units. Each fan unit is programmed with a duty cycle intensity from 0-100%, which directly determines the fan speed.

4.2 W-band Transceiver

W-band Stage

A 95GHz Doppler radar developed at the Jet Propulsion Laboratory (JPL) is used to propagate mmWave EM energy through the turbulent flow (Fig. 4.3) [39]. This particular hardware was chosen due to its ready availability. In this work, the radar is not used for ranging, but rather as a single tone continuous wave transceiver. The 95GHz RF output applies optical duplexing techniques, enabling a single parabolic reflector to be used for both transmit and receive.

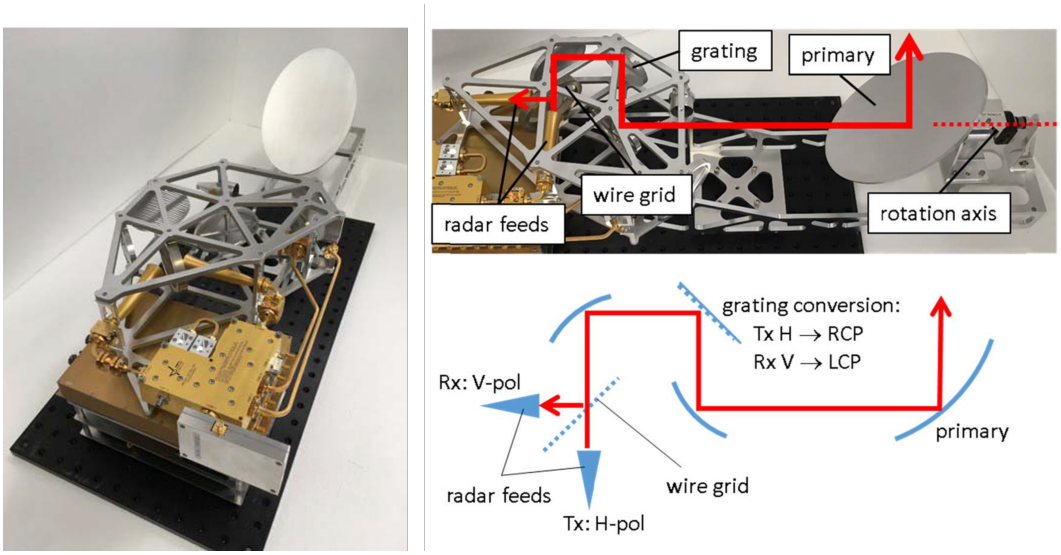

Figure 4.3: The W-band transceiver used to propagate mmWave EM energy through the turbulent flow, and optical duplexing mechanism. The PSD of the received signal is analyzed to characterize the turbulent effects of scintillation on the EM signal.

The transmitter (Tx) horn antenna propagates a vertically polarized wave through a wire grid, which is converted into left-hand circular (LHC) polarization by a metal grating before being reflected off the main reflector. Upon reflection from the target, the wave changes to right-hand circular (RHC) polarization, and is subsequently converted into horizontal polarization from the grating in the return path. The horizontally polarized wave is reflected (rather than transmitted) by the wire grid, directing the returned signal to enter the receiver (Rx) horn antenna. An optional low noise amplifier (LNA) can be included at the front end of the Rx branch to minimize the noise figure and amplify the received signal. However, in this work the LNA is omitted because the short propagation distance results in relatively high Rx power levels, and including the LNA could saturate the receiver.

The W-band transceiver utilizes a single heterodyne architecture with a 92GHz local oscillator (LO) and 3GHz IF (Fig. 4.4). The generation of the 92GHz LO signal originally came from a voltage-controlled oscillator (VCO), followed by a complementary metal-oxide-semiconductor (CMOS) synthesizer to multiply up the 47.92MHz VCO output to 92GHz. The absence of a phase-locked loop (PLL) meant that the VCO exhibited very poor phase noise performance, and consequently the phase noise of the 92GHz LO also suffered. Although the phase noise would be self-cancelled at the Rx output of the heterodyne stage, the excessive phase noise still leaked through and contributed significantly to the system phase noise of the receivd signal. The 3GHz IF is generated from a phase locked dielectric resonator oscillator (PLDRO) from Microwave Dynamics (PLO-3000).

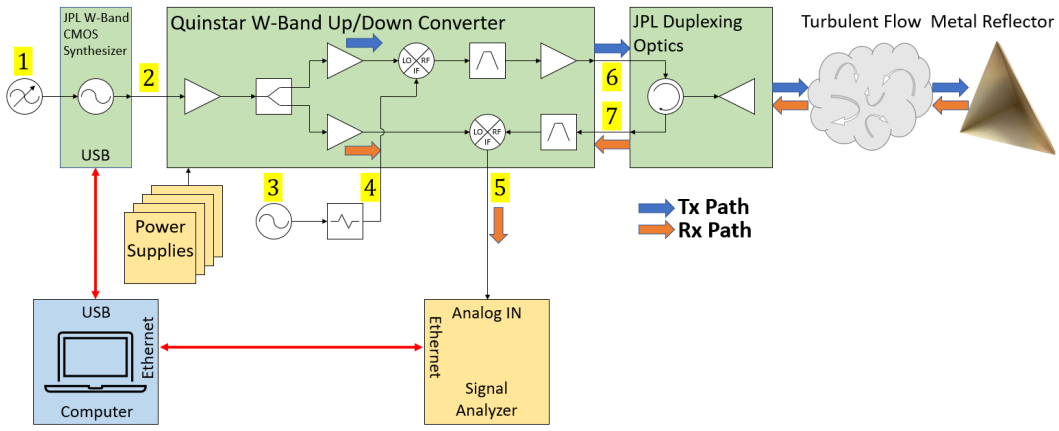

Figure 4.4: Single heterodyne stage transceiver architecture with 92GHz LO generated from a CMOS synthesizer, sourced by a VCO, and 3GHz IF generated by a PLDRO. The frequency and power levels at each highlighted point in the architecture are summarized in Table 4.1.

Position	Frequency (GHz)	Power (dBm)
1	0.04792	9
2	92.0	0
3	3.0	15
4	3.0	-4
5	3.0	-
6	95.0	18
7	95.0	-

Table 4.1: Frequency and power levels at highlighted positions in the single heterodyne architecture (Fig. 4.4).

The advantage of this monostatic heterodyne architecture, which employs a common LO source for both the Tx and Rx branches, is the close-in phase noise self-cancellation of the 92GHz source. The self-cancellation effect can be better understood by noting that in a transceiver with a shared LO source, the LO phase noise in the Rx branch is a time-shifted copy of the LO phase noise in the Tx branch. Therefore, the total phase noise at the receiver is:

$$\phi(t) = \phi_{LO}(t - \tau_R) - \phi_{LO}(t) + \phi_{IF}(t - \tau_R) \tag{4.1}$$

where $\phi_{LO}(t)$ and $\phi_{IF}(t)$, are the phase noise of the 92GHz LO source and 3.2GHz IF source, respectively, and τ_R is the round trip propagation delay of the folded LoS propagation link. Since the Tx and Rx branches share a common LO source, their phase noise is correlated and self-cancels after the down-conversion. The residual receiver system phase noise is thus dominated by the IF source (Fig. 4.5).

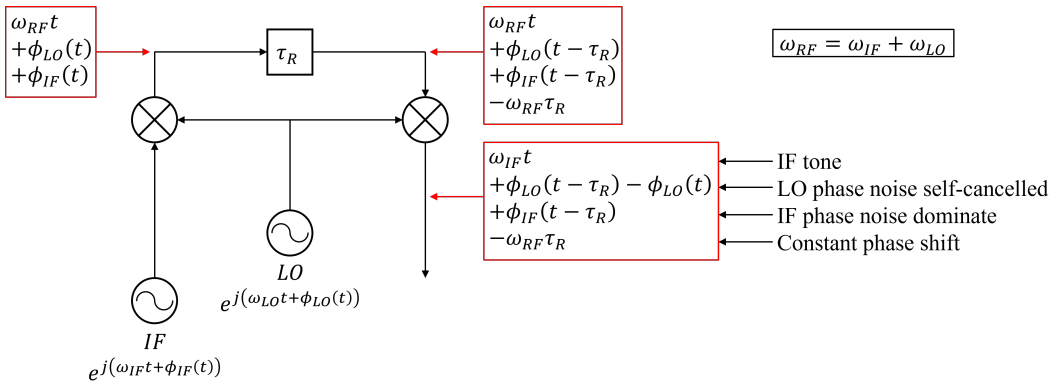

Figure 4.5: Total phase noise contributions at various points in a single heterodyne architecture. The difference of $\phi_{LO}(t - \tau_R) - \phi_{LO}(t)$ causes the LO phase noise to be self-cancelled at the receiver, so the close-in phase noise at the receiver is dominated by the IF source.

In the frequency domain, the phase noise self-cancellation can be understood by considering that the transfer function of the difference of the two processes in which one is just a time delayed version of the other:

$$H(j\omega) = e^{-j\omega\tau_R} - 1 \tag{4.2}$$

This results in the output PSD of the system as [40]:

$$\begin{aligned} S(f) &= |H(j\omega)^2| S_{LO}(f) + S_{IF}(f) \\ &= 2S_{LO}(f)(1 - cos(2\pi f \tau_R)) + S_{IF}(f) \end{aligned} \tag{4.3}$$

Therefore, the CMOS 92GHz LO source demonstrates phase noise self-cancellation at the receiver, resulting in negligible contributions at close-in frequencies.

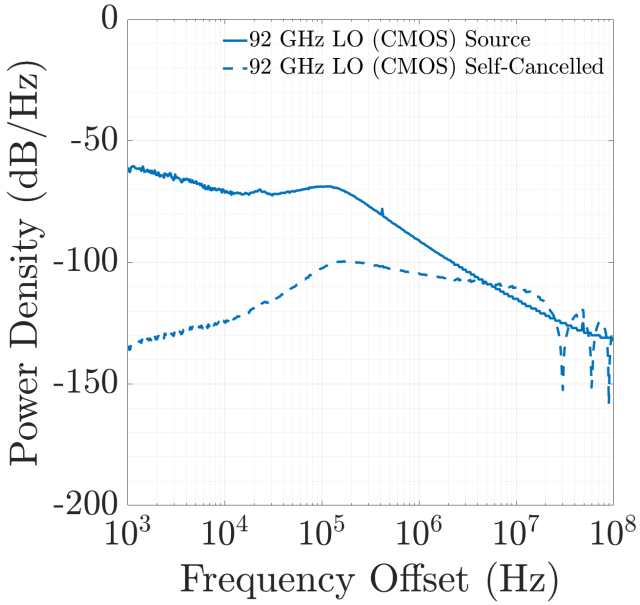

Figure 4.6: Phase noise of 92GHz LO in a single heterodyne architecture. The measured phase noise of the 92GHz LO CMOS source (solid blue trace) becomes self-cancelled at the receiver (dashed blue trace), using a round trip propagation distance of $R = 10m$ and a delay of $\tau_R = R/c = 33.3ns$.

Second Heterodyne Stage

Two modifications were made to the original architecture to further suppress system phase noise at the receiver: (i) the 92GHz CMOS source was replaced, and (ii) a second heterodyne stage was appended to the W-band stage to down-convert the 3GHz signal to 200MHz (Fig. 4.7).

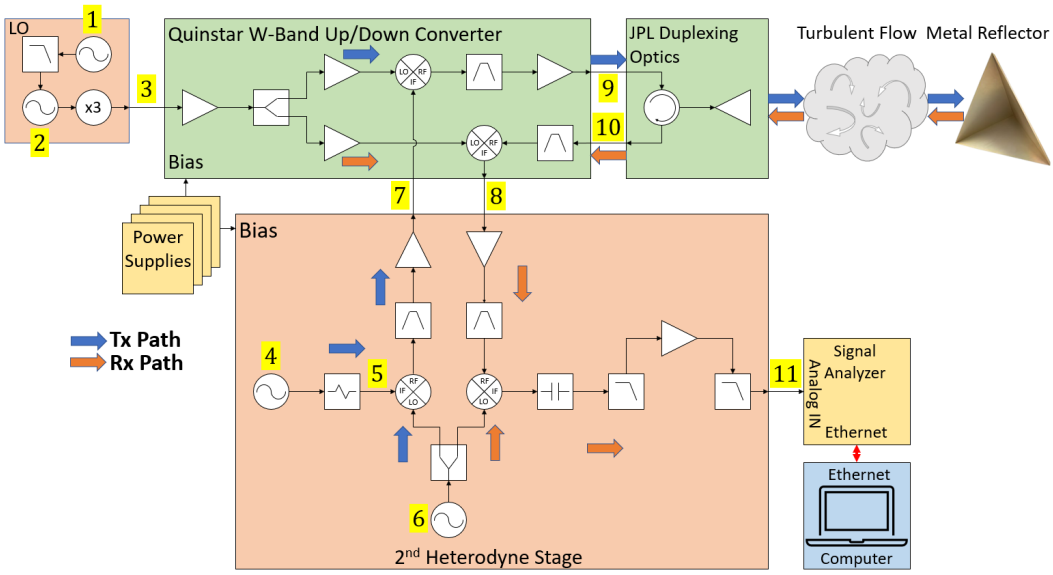

Figure 4.7: Double heterodyne stage transceiver architecture. The W-band LO source is replaced with a 30.8GHz PLDRO fed into a passive tripler to generate a phase-locked 92.4GHz LO source with significantly lower phase noise compared to the CMOS synthesizer (Fig. 4.4). The double heterodyne architecture results in significantly lower system phase noise at the receiver, since sources in the hundreds of MHz range can achieve lower phase noise compared to GHz or W-band range, allowing for better analysis and characterization of scintillation. The frequencies and power levels at the highlighted positions are summarized (Table 4.2).

Position	Frequency (GHz)	Power (dBm)
1	0.100	13
2	30.80	17
3	92.4	0
4	0.200	13
5	0.200	-10
6	3.22	15
7	3.02	-4
8	3.02	-
9	95.42	18
10	95.42	-
11	0.200	-

Table 4.2: Frequencies and power levels at highlighted positions in the double heterodyne architecture (Fig. 4.7).

The 92GHz CMOS LO source was replaced with a 30.80GHz PLDRO (Exodus Dynamics EDPLO-2000), followed by a passive frequency tripler (Eravant SFP-103KF-S2). The EDPLO-2000 uses the 100MHz output from an ultra-low phase noise Oven Controlled Crystal Oscillator (OCXO) (Wenzel 501-25469). The 3GHz signal is

generated by mixing a 200MHz 'BB' source with a 3.2GHz 'IF' source. The 3.2GHz source is first passed through a power divder (RF-Lambda RFLT2W2G04G). In the Tx path, this 3.2GHz signal is used as the LO input of the upconversion mixer (Marki Microwave MM1-0212LS), and the 200MHz source is used as the IF input. The resulting RF output is passed through a bandpass filter (BPF) consisting of back-to-back lowpass filter (LPF) (RF-Lambda RLPF13G03) and highpass filter (HPF) (RF-Lambda RHPF23G03G12), both with a stopband of 3GHz. This allows a single 3GHz tone to pass through, filtering out all images and harmonics. The 3GHz output is passed through an amplifier (Mini-Circuits ZJL-4HG+) to achieve the required input power of the W-band stage. A 200MHz OCXO is used for the BB source (Wenzel 501-28309), with attenuators placed at the output to set the desired power level, along with an LPF to reduce the effect of spurious harmonics.

At the Rx branch of the second heterodyne stage, the same amplifier and BPF combination as the Tx branch are used to amplify and filter the received 3GHz signal. This signal is passed into the RF port of the downconversion mixer, with the LO port being the other output of the 3.2GHz power divider. The IF output is passed through a DC block (Pasternack PE8212), followed by an LPF (Pasternack PE8726) to filter out images, amplifier (Mini-Circuits ZKL-1R5+) to boost signal strength, and an antialiasing filter (Pasternack PE8722). The 3.2GHz source is generated by a dual frequency synthesizer (Valon 5009a), to leverage the programmability and use it to produce specific frequency outputs at decent phase noise performance. The output phase noise of the 5009a is not the lowest option, but the performance of the IF source is ultimately inconsequential since it is self-cancelled after the second down-conversion mixer. The 5009a utilizes a 20MHz internal reference for the frequency generation. However, the internal reference results in significant spurious tones at harmonics of the reference. This resulted in an undesirable tone to linger near the 200MHz received signal, appearing in the initial measurements. To fix this, a 70MHz external reference from another 5009a is used instead. 70MHz was selected so that the resulting harmonic spurs would not appear close to 200MHz, thus eliminating any unwanted tones appearing in the close-in phase noise measurements. The second heterodyne stage is implemented on a rigid aluminum sheet with the commercial components securely mounted (Fig. 4.8).

In this double heterodyne architecture, the phase noise contributions from both the 92GHz LO and 3.2GHz IF sources self cancel, allowing the 200MHz BB phase noise to dominate at the receiver (Fig. 4.9). The simulated phase noise at each stage

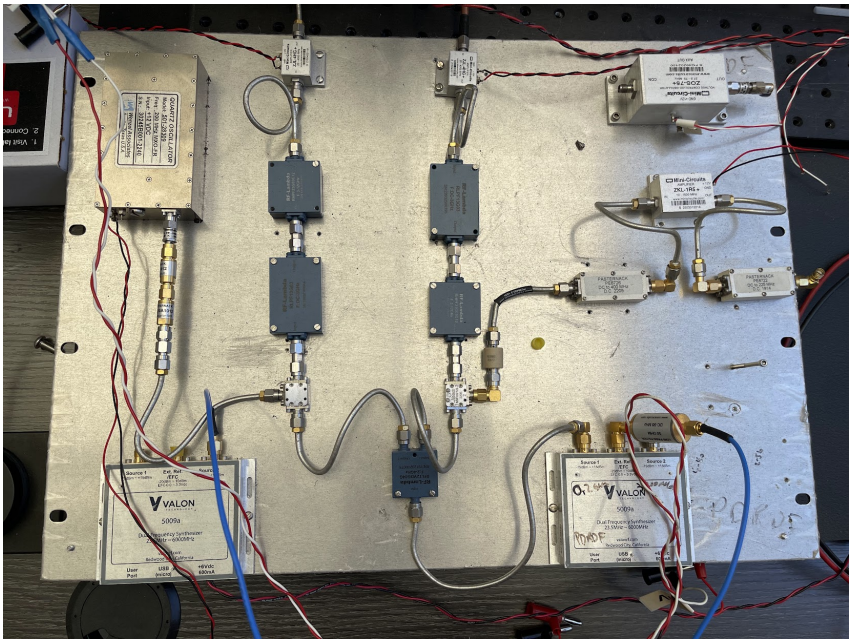

Figure 4.8: Second heterodyne stage built with commercial components. This 2nd heterodyne stage introduces a 200MHz BB source, mixed with a 3.2GHz LO to create the 3GHz IF tone to be fed into the W-band stage. The resulting received 200MHz signal has significantly lower system phase noise and its PSD is analyzed to characterize the scintillation.

of the system confirms that scintillation effects dominate at close-in frequencies due to the phase noise self-cancellation (Fig. 4.10).

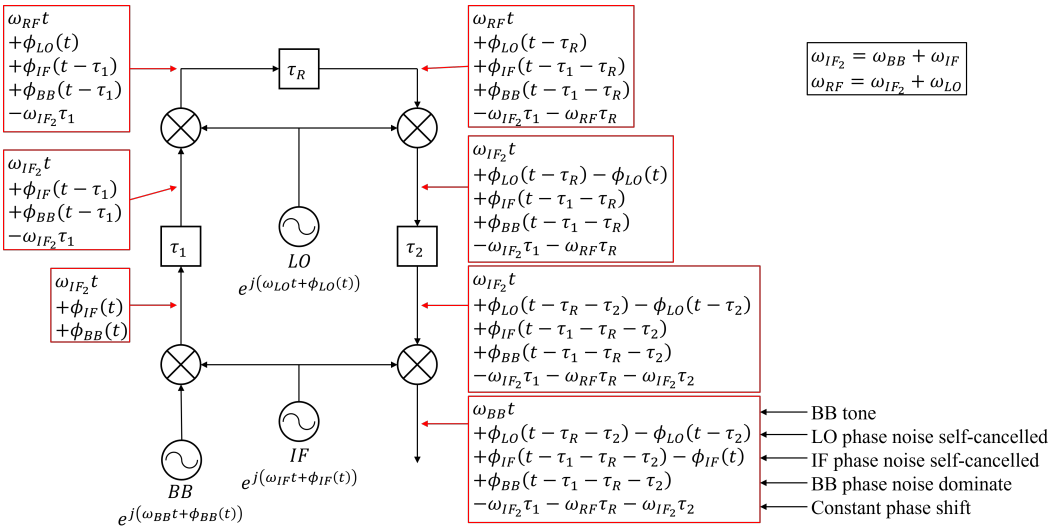

Figure 4.9: Total phase noise contributions at various stages of the double heterodyne architecture. At the receiver, the IF and LO phase noises are self-cancelled due to the difference between their time-shifted versions, leaving the BB source as the dominant contributor to the overall phase noise.

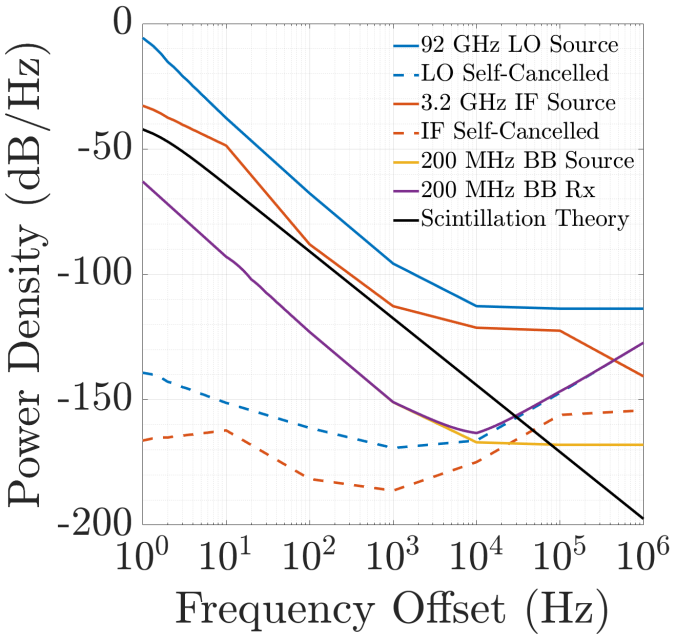

Figure 4.10: Phase noise in the double heterodyne architecture. The blue and orange solid traces represent the phase noise of the 92GHz LO and 3.2GHz IF sources, respectively, while the dashed traces show their self-cancelled contributions at the receiver. The 200MHz BB Rx phase noise is dominated by the BB source. The theoretical scintillation PSD is included for comparison, and is observed to dominate over the BB Rx phase noise, enabling scintillation to be measured.

The hardware components require 3 different voltage levels: 6V, 12V, and 15V. These are supplied by a triple output power supply. The entire system is placed on an adjustable height desk with wheels for ease of mobility during testing (Fig. 4.11).

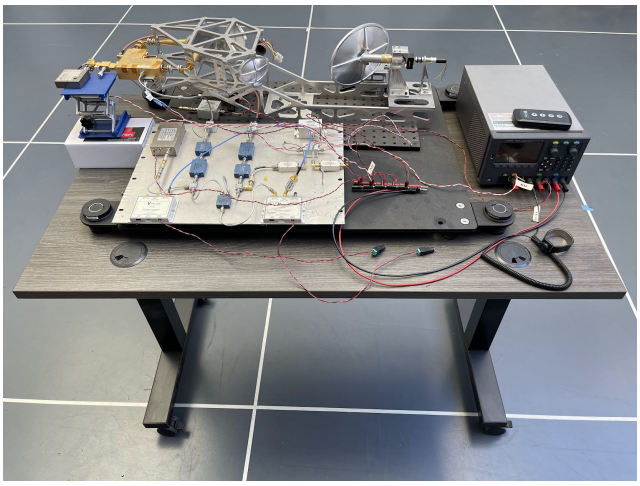

Figure 4.11: Overall transceiver hardware system with both heterodyne stages and power supply. The hardware is placed on top of a vibration isolation platform to minimize mechanical vibrations.

Additional Supplementary Components

To minimize the effect of mechanical vibrations, the transceiver is placed on a vibration isolation platform (Newport VIP320X2430-00100) (Fig. 4.12).

Figure 4.12: Vibration isolation platform supporting the transceiver to minimize the mechanical vibration effects. The platform is 30"x24", with a load capacity of 100lbs, and horizontal and vertical resonances of 3.25Hz and 4.75Hz, respectively.

Preliminary experiments relied on reflections from the electrical panels in the CAST facility to create a folded LoS propagation link. However, this approach proved to be unreliable, as the absence of a well defined reflector led to significant scattering and made characterization difficult. To address this, dedicated target reflectors were introduced (Fig. 4.13). A 1mx1m sheet of Holland Shielding Microwave Absorber Foam 3500 was placed behind the reflector to suppress potential multipath reflections. Sandbags were used to stabilize both the tripod and the table supporting the transceiver, to further mitigate mechanical vibrations.

(a)

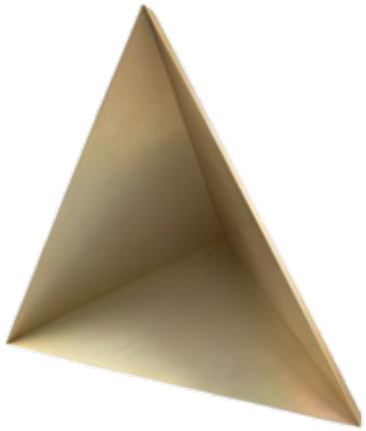

(b)

Figure 4.13: Reflectors used to create a folded LoS propagation link with the transceiver. The initial (a) flat aluminum sheet was replaced with (b) a trihedral corner reflector (Eravant SAJ-160-S1) to achieve better performance and minimize scattering. The trihedral shape reflects all of the incident EM energy with minimum scattering. It is mounted on a tripod at the same height as the transceiver parabolic reflector, 5m across the facility on the other side of the FAWT.

4.3 Temperature

Several approaches were explored to generate a large temperature gradient in a safe and practical way. The goal was to establish a uniform gradient that was cost effective, feasible, and minimally disruptive to the CAST environment to allow convenient setup and removal of the components. Convection heaters were selected over radiative heaters, as direct heating of the air in the flow was required.

Finned Channel Strip Heaters

The first heating approach implemented was using a finned channel strip heater (Fig. 4.14). The high surface area and resilience enabled these strip heaters to achieve very high temperatures for a wide range of industrial applications. The strip heaters were mounted on a metal truss made of 80/20 extrusions, and placed horizontally across the full length of the FAWT (Fig. 4.15).

Figure 4.14: Finned channel strip heater used to generate temperature gradient uniformly across the full length of the FAWT. The strip heaters constructed with nickel-plated steel fins, with electrical specifications of 208V, 3400W, 1-phase, T3 termination and a custom size of 1.375"x2"x120".

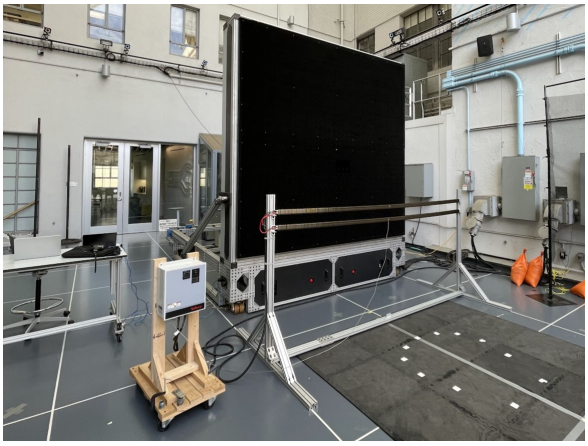

Figure 4.15: Finned channel strip heaters mounted on a metal truss and positioned in front of the FAWT in the CAST arena, along with a temperature control panel (PCM10082) and ring thermocouple (TRW00127) used to power and set the operating temperature, respectively. The strip heaters are powered using the 3-phase power panel in the CAST facility.

Although extending the strip heaters across the full length of the FAWT was appealing for generating a uniform temperature gradient, measurements presented in the following chapter demonstrate the limitations of these strip heaters to generate a sufficiently large gradient. Therefore, the strip heaters are replaced in favor of utility heaters in subsequent experiments.

Utility Heaters

The PKB Platinum Model PKB2015-3-P utility heater was chosen for its power and portability to replace the strip heaters (Fig. 4.16). 3 heaters were installed due to the limited number of electrical panels available in the CAST arena.

Figure 4.16: PKB2015-3-P electronic portable utility heater, used to generate large temperature gradients in place of the strip heaters. Each heater is controlled by a remote, and has internal fans to blow the hot air which is generated by an electric coil. The front grill of the heater has fins to direct the heat flow.

Thermal Screen and IR Camera

Temperature measurements of the flow are performed with the objective of achieving high spatial and temporal resolution by leveraging the compactness of the proposed experimental setup to determine the absolute temperature profile and resulting temperature gradients. Installing multiple individual sensors at various locations in the flow was deemed inefficient, since the number of sensors required to achieve a sufficient spatial resolution would be impractical. Instead, a large thermal screen made of a material with an emissivity close to 1 is employed, allowing the temperature of the screen to closely mimic the temperature of the heater airflow. Upon reaching a steady state in the flow, an IR camera is to capture the resulting temperature profile of the flow efficiently avoiding the need for an excessive number of sensors.

Several materials were tested as potential candidates for the thermal screen, including plastic, fiberglass, acrylic, and glass. Key factors considered were emissivity, size, cost, and practicality for ease of handling and setup (Table 4.3).

Specification	Plastic	Fiberglass	Acrylic	Glass
Emissivity	0.84	0.75	0.94	0.92
Dimensions	48"x96"x0.157"	96"x100’	48"x96"x0.125"	30"x36"x0.092"
Price	$22.74	$129.99	$136.00	$17.59

Table 4.3: Overview of specifications for different candidates for the thermal screen.

Glass was the first to be dismissed due to its fragility and sharp edges, which made it both unsafe and impractical. Acrylic was also rejected because it was difficult to support in a rigid and stable manner. The initial tests were conducted with fiberglass, which is lightweight and convenient to handle and roll up. The fiberglass was clamped onto a large adjustable frame to stretch it taut and allow it to stand upright in the strong winds generated by the FAWT (Fig. 4.17).

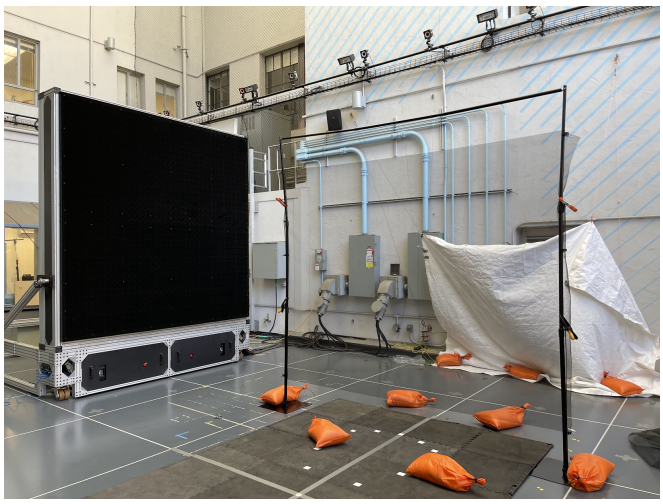

Figure 4.17: Fiberglass thermal screen propped up using a 10’x10’ drape stand for temperature measurements using the IR camera. The temperature of the fiberglass heats us with the airflow, allowing the IR camera to measure the temperature profile of the flow. Measurement results show that the transparency of the fiberglass make it a non-ideal candidate for the thermal screen.

However, the flimsiness of the fiberglass made it difficult to achieve a consistently taut and stable screen that does not flutter in the flow. Furthermore, the mesh structure allowed the background to be visible to the IR camera, causing the measured temperature to include contributions from the surroundings rather than solely from the screen. As a result, this method produced inaccurate temperature profiles of the flow, which will be discussed further in the measurement results.

Ultimately, plastic was chosen as the best option for the material of the thermal screen. With a relatively high emissivity, lightweight construction, sturdiness, and opacity, it proved to be the most practical option that delivered the most reliable results. The plastic screen is mounted on an adjustable frame with Velcro straps (Fig. 4.18). Because it is not fully opaque, additional plastic sheets were placed behind the screen to make a more uniform background, ensuring the IR camera measurements isolate the temperature effects of the air flow.

Figure 4.18: Plastic thermal screen strapped to an adjustable 10'x8' backdrop stand.

Finally, the temperature of the thermal screen is measured using a FLIR T560 IR camera. This camera records radiometric data and provides adjustable settings to accurately measure temperature values based on ambient conditions, distance to the object, and emissivity of the object. The camera has a $24° \times 18°$ field of view, with 640×480 pixel resolution and $< 40mK$ thermal sensitivity at $30°C$. The IR camera is mounted on a tripod, and the distance to the thermal screen and height are recorded to be able to calculate the dimensions and relative positioning of the measured temperature profile of the flow.

4.4 Humidity

In addition to large temperature gradients, generating and measuring a humidity gradient was considered as another approach to modulate the value of C_n^2 in the flow. This section summarizes the attempt to create a humidity gradient using an fogger machine, as well as the devices employed to measure the resulting humidity.

Fogger

One method for generating a humidity gradient involved using a fogger machine to spray a fine mist that would inject moisture into the flow (Fig. 4.19). A single fogger was initially purchased to test the feasibility. Measurement results presented in the following chapter demonstrate the challenges of this method, as the water droplets were too large and tended to condense on the measurement devices, preventing accurate humidity characterization.

Figure 4.19: Fogger machine for generating humidity gradient.

Hygrometers

Humidity measurements are made using multiple hygrometers positioned at various locations in the flow to characterize the humidity under different FAWT and heater configurations. Several devices were tested with and iterated through (Fig. 4.20).

(a) (b) (c)

Figure 4.20: Hygrometers used for humidity measurements. The first device tested was (a) Extech 445815 lacked data logging capabilities and was therefore replaced by the (b) Extech 42270 which enabled temperature and humidity measurements with data logging. This was subsequently replaced with the (c) TandD TR-73U USB connectable logger for temperature, humidity, and barometric data logging. The sensors were more exposed, allowing for potentially more accurate measurements facing the wind flow. The relative humidity, temperature, and pressure measurements are used to calculate the specific humidity.

4.5 Wind Speed

Wind speed measurements of the flow are essential for determining the statistical distributions and dynamics relevant to both turbulence and scintillation modeling. The mean wind speed is particularly important for the application of Taylor's frozen flow hypothesis, while the frequency content obtained from high speed measurements provides valuable insight on the turbulent intensity and characteristic scales. The anemometers used for wind speed measurements are detailed in this section.

Vane Anemometer

Initial wind speed measurements were made in various locations in the flow using a data logging vane anemometer, the REED R4000SD (Fig. 4.21). The data logging capability enabled the recording of wind speeds over extended durations to quantify the changes over time for different FAWT intensities. However, with a maximum sampling rate of 1Sa/s, the instrument provided limited statistical information and was unable to capture any significant frequency content of the flow.

Figure 4.21: REED R4000SD data logging vane anemometer for wind speed measurements. The vane anemometer is placed in various positions in the flow to characterize the mean wind speed v over time for different FAWT and heater configurations.

Combination Anemometer

To capture the frequency content of the flow, high speed wind measurements were obtained using a combination of a sonic anemometer and a constant temperature anemometer (CTA) (Fig. 4.22) [41]. The sonic anemometer is beneficial since it

does not require any calibration, however the sampling speed is limited to 100Sa/s. On the other hand, the CTA provides a much higher sampling rate of 10kSa/s but requires extensive calibration. The large temperature fluctuations caused by the utility heaters make calibrating the CTA particularly challenging in this experimental setup. To address this, measurements are made with both anemometers operating in tandem, and the values of the sonic anemometer are used as the ground truth for the CTA. A curve fitting algorithm is applied to calculate the wind speed values of the CTA during post-processing, eliminating the need for conventional calibration procedures [42], [43].

Figure 4.22: Combination of sonic anemometer (Campbell Scientific CSAT3B) and CTA (Dantec Dynamics MiniCTA 54T42, with probe TSI 1201-20W) for high speed wind fluctuation measurements. The CTA probe is positioned in the center between the transducers of the sonic anemometer to ensure co-located measurements. The entire apparatus is deployed at multiple locations within the flow to characterize the turbulent dynamics along the EM beam propagation path of the beam.

Chapter 5

MEASUREMENTS RESULTS

This chapter provides a detailed explanation of the experiments conducted and corresponding measurement results. It begins with the preliminary measurements that did not yield significant results, but motivated iterative improvements to the experimental setup. The chapter then presents transceiver measurements performed to verify the phase noise self-cancellation, followed by results from the 2 primary configurations: heaters in front of the FAWT, and heaters on the sides of the FAWT. Both transceiver measurements and meteorological measurements are described, and they are tied together to compare with scintillation theory. The development of an empirical model that builds on top of the the theoretical framework is presented. The significance and interpretation of the measurement results is discussed.

5.1 Preliminary Measurements

This section presents the preliminary measurement techniques that did not yield significant results, thus motivating the development of more effective methods.

Strip Heater Measurements

The initial method for generating a temperature gradient employed the finned channel strip heaters mounted on the metal truss, in combination with the fiberglass screen and an IR camera to measure the resulting temperature profile (Fig. 5.1).

A FLIR T450SC IR camera, borrowed from the JPL loan pool, was used to perform these measurements since the FLIR T560 was not yet available. The temperature of the fiberglass screen was captured with different FAWT intensities (Fig. 5.2). These measurement results clearly demonstrate that, although the strip heaters themselves achieve high surface temperatures, they were unable to generate a significant temperature gradient in the surrounding air flow. Once the FAWT was activated, the heat produced by the strip heaters was negligible compared to the strong winds from the FAWT, rendering this method ineffective. Consequently, the strip heaters were replaced with the heavy duty utility heaters. In addition, the transparency of the fiberglass screen is apparent in these measurements, as the electrical panels of the CAST facility appear in the background of the IR camera measurements.

Figure 5.1: Experimental setup for temperature measurements using the finned channel strip heaters, fiberglass thermal screen, and IR camera. The strip heaters are positioned in front of the FAWT, extending across its entire length. The fiberglass screen is placed perpendicular to the face of the FAWT to capture the temperature profile of the flow, while the IR camera is mounted on a tripod outside the flow region to perform the measurements.

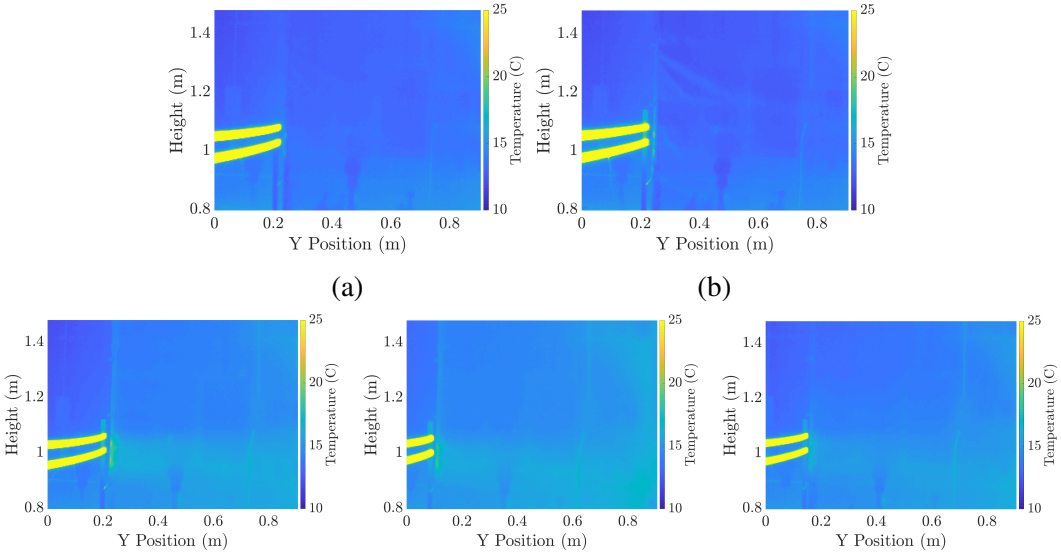

Figure 5.2: Temperature measurement results for finned channel strip heater with fiberglass thermal screen with FAWT intensities at (a) 0%, (b) 20%, (c) 40%, (d) 60%, (e) 80%. Although the actual strip heaters achieve temperature up to 650°C, the actual temperature increase of the air flow is insignificant.

VNA and Utility Heater Measurements

Prior to appending the second heterodyne stage, initial measurements were conducted using only the W-band heterodyne stage. One approach for capturing the data employed a vector network analyzer (VNA) (Fig. 5.3). This setup was tested using the utility heaters and fiberglass thermal screen (Fig. 5.4).

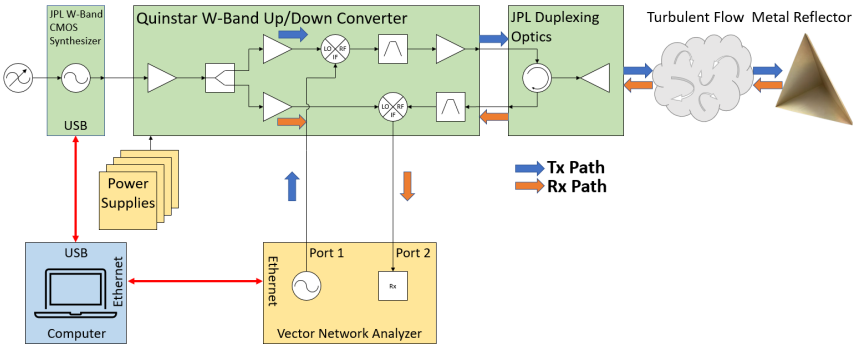

Figure 5.3: Single heterodyne architecture used for VNA measurements. In this configuration, port 1 of the VNA provides the 3GHz IF source, while port 2 serves as the receiver. The magnitude and phase of S_{21} provided statistical information about the signal, and theoretically contains both amplitude and phase information of the transceiver chain, including the effects of scintillation.

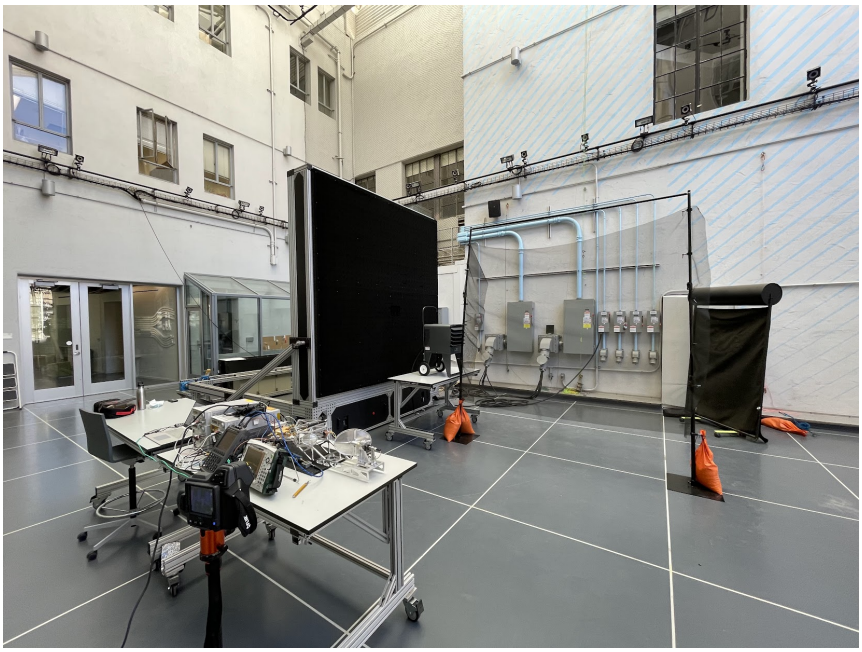

Figure 5.4: Experimental setup for VNA measurements using the utility heaters, fiberglass thermal screen, and IR camera. The transceiver propagates EM energy through the turbulent flow, which then reflects off the electrical panels located at the far end of the CAST facility.

Measurements were conducted by sampling the magnitude and phase of S_{21} at $20Sa/s$ for 500s in each state of 3 states. The experiment was repeated with and without the fiberglass screen (Fig. 5.5). The time series data reveal a significant issue, confirming that the thermal screen must be removed during transceiver measurements and motivating the sequential, rather than concurrent, execution of transceiver and meteorological measurements in all subsequent experiments.

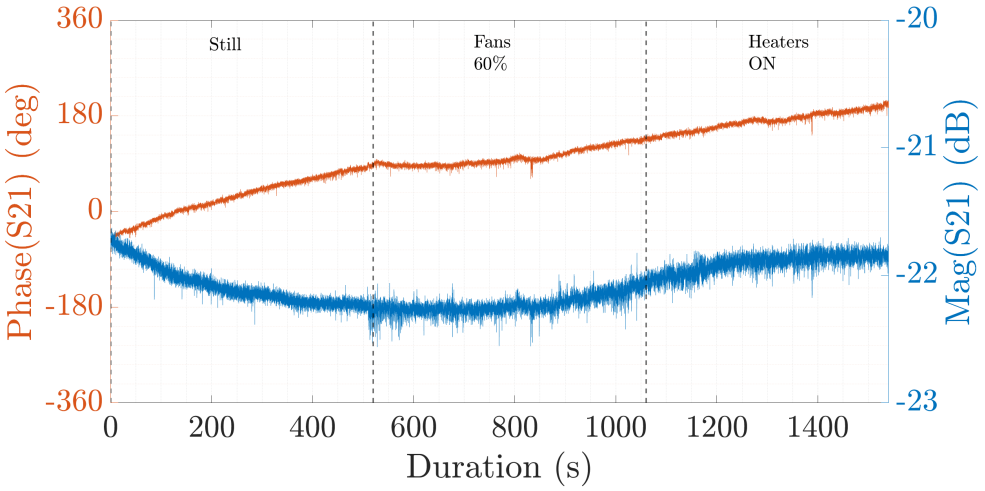

(a)

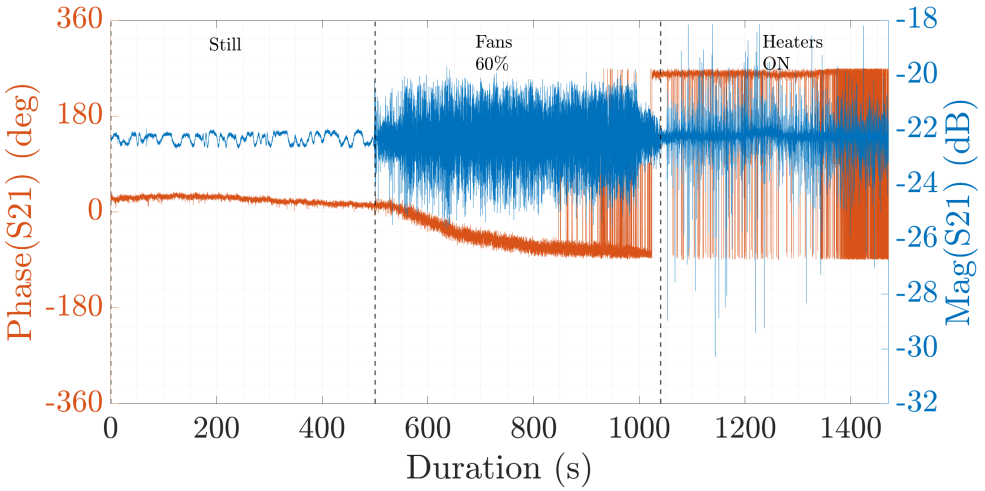

(b)

Figure 5.5: Measurement results of the magnitude and phase of S_{21} versus time for 3 different states: (i) 'Still', where both FAWT and heaters are off, (ii) FAWT at 60% intensity, and (iii) FAWT at 60% intensity with heaters on, (a) without fiberglass screen, and (b) with fiberglass screen. The inclusion of the fiberglass screen obstructs the propagation of the EM beam, causing major perturbations in both the magnitude and phase of S_{21}, particularly when the FAWT is operating which causes the screen to flutter.

From the time series data, the PSD of the phase of S_{21} was calculated, as only phase scintillation was considered at this stage (Fig. 5.6). The combination of the VNA's slow sampling rate and high phase noise of its port 1 source meant that the data provided no meaningful insight towards scintillation characterization. Therefore, the VNA based measurement setup abandoned in favor of more accurate methods.

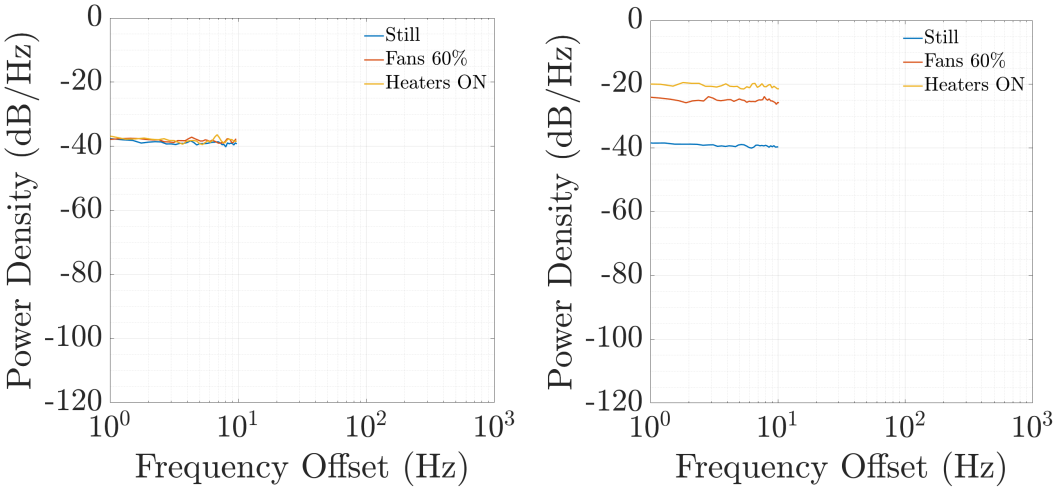

Figure 5.6: PSD of the phase fluctuations of S_{21} calculated from the time series data (Fig. 5.5) for each of the 3 states, (a) without fiberglass screen, and (b) with fiberglass screen. The VNA's slow sampling rate of $20Sa/s$ severely limits the observable frequency range. Furthermore, the internal oscillator of the VNA cannot be fully characterized and exhibits high levels of phase noise. This is undesirable, as the goal of the setup is to minimize system phase noise to allow scintillation to dominate for accurate analysis and characterization.

Temperature measurements are made using the utility heaters and fiberglass thermal screen, with the FLIR T450C IR camera (Fig. 5.7). The results demonstrate that the utility heaters generate significantly more heat than the strip heaters, and are therefore used for all subsequent experiments. In addition, the fiberglass screen was replaced with a plastic screen for future experiments, which is more opaque, exhibits less flutter, and maintains high emissivity.

Fogger and Humidity Gradient Measurements

The fogger machine was employed to generate a humidity gradient to augment C_n^2, in conjunction with the temperature gradient produced by the heaters. Multiple hygrometers were placed at various heights in the flow to characterize the humidity profile (Fig. 5.8). Inconsequential data lead to this approach being abandoned, and additional techniques for generating humidity gradients is put off to future work.

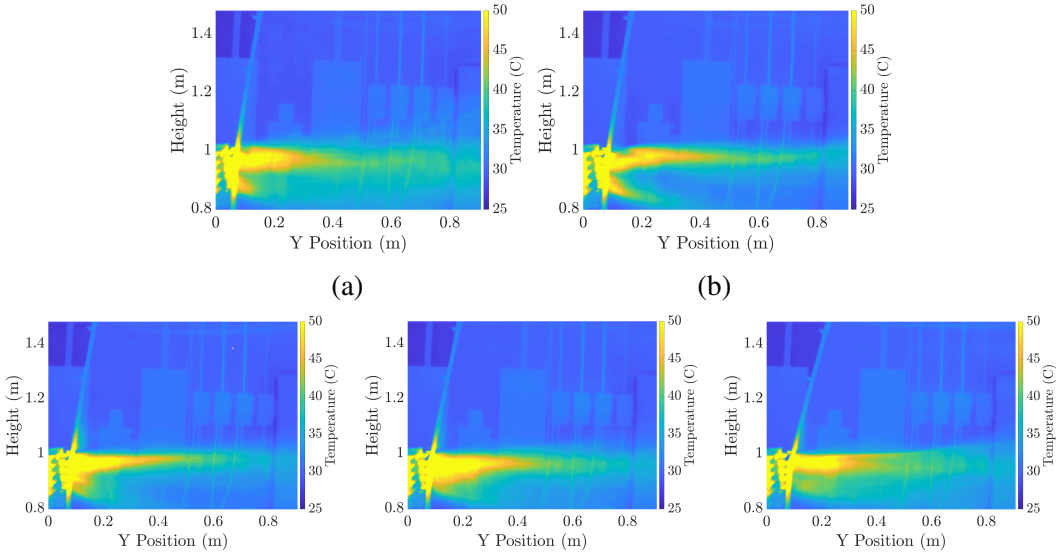

Figure 5.7: Temperature measurements using FLIR T450C IR camera with utility heaters and fiberglass thermal screen at FAWT intensities of (a) 0%, (b) 20%, (c) 40%, (d) 60%, and (e) 80%. The utility heaters themselves have internal fans that blow the hot air, so this additional wind flow must be considered when evaluating the turbulent dynamics for future experiments. These measurement results further highlight the limitation of the fiberglass screen due to its transparency, which reduces the accuracy of temperature gradient calculations. Although the fiberglass screen qualitatively demonstrates significant increases in the temperature from the utility heaters, the undesired background structures affect the quantitative analysis of the temperature profile of the flow.

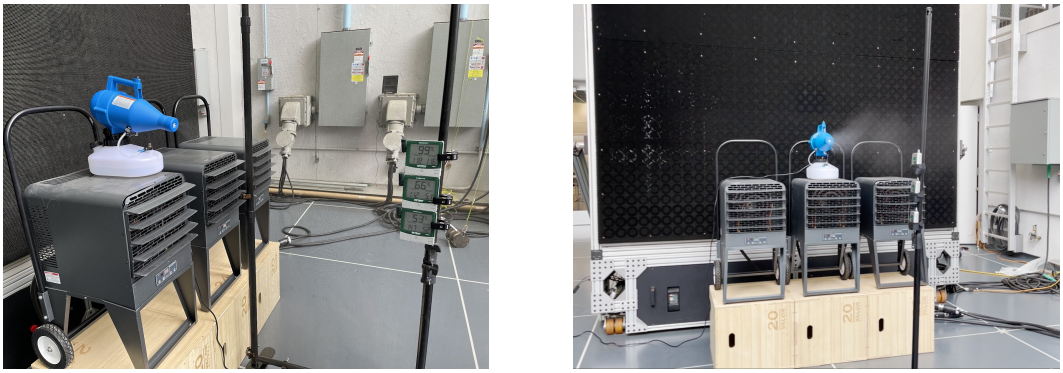

Figure 5.8: Experimental setup for testing the fogger machine and humidity measurements. Initial measurements using digital hygrometers (a) demonstrate sensor saturation due to condensation of water vapor. Another view (b) highlights the mist more clearly, but still results in saturation and condensation on the temperature and humidity data loggers.

5.2 Initial Transceiver Measurements

Preliminary transceiver measurements are made using the spectrum analyzer (SA) function on a FieldFox N9952A to capture the power spectrum of the signals (Fig. 5.9). These measurements were conducted to verify the phase noise self-cancellation of the double heterodyne transceiver, and determine if scintillation could be observed with the utility heaters and FAWT in this experimental setup.

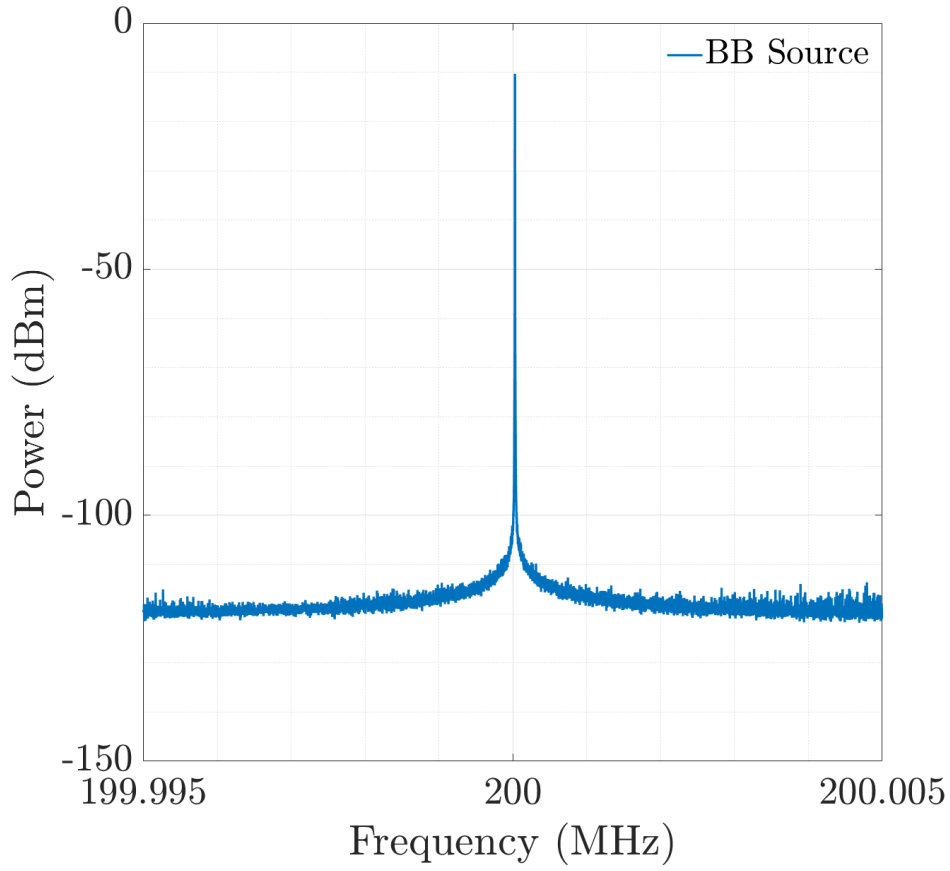

Figure 5.9: Sample power spectrum measurement of the 200MHz source using the SA. The PSD is calculated by plotting power levels relative to the carrier at frequency offsets from the center frequency. Measurements are taken with a resolution bandwidth of 1Hz, a span of 10kHz, and 20,001 points. Multiple samples are averaged to produce smoother PSD plots.

A preliminary test of the phase noise self-cancellation of the 3.2GHz IF isolates the second heterodyne stage. The 'loopback' test is performed by connecting the 3GHz Tx directly to the 3GHz Rx, and analyzing the 200MHz Rx output (Positions 7, 8, and 11, respectively, in Fig. 4.7). This configuration bypasses the W-band stage, and is used as a 'smoke test' to verify the phase noise self-cancellation of the isolated second heterodyne stage (Fig. 5.10a).

Next, the phase noise self-cancellation of both the 92.4GHz LO and 3.2GHz IF sources was tested using the trihedral reflector as the target. Since the SA input is limited to 50GHz, the 92.4GHz LO source phase noise was calculated using the measured 30.80GHz PLDRO phase noise and scaling it by a factor of 3 (equivalently adding $10 * log(3)$ in logarithmic scale). The use of the trihedral reflector verifies that the phase noise contributions from the LO and IF sources are self-cancelled at the Rx (Fig. 5.10b).

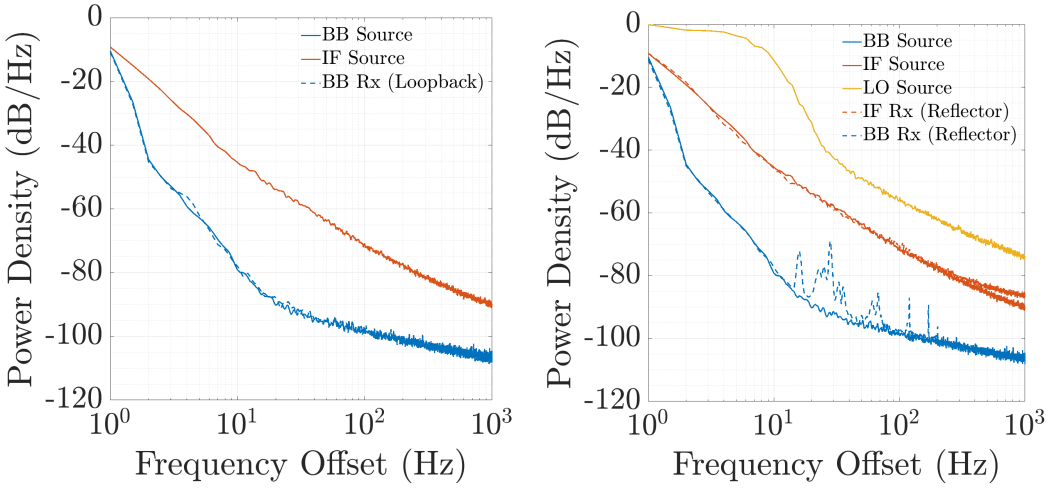

Figure 5.10: PSD measurements using the SA demonstrating the phase noise self-cancellation of the 3.2GHz IF and 92.4GHz LO sources. Solid traces represent measurements from the sources, while dashed traces are the corresponding measurements at the receiver. Preliminary measurements from (a) the isolated second heterodyne stage show that the 3.2GHz IF phase noise is fully self-cancelled at the 200MHz BB Rx, as indicated by the dashed blue trace being identical to the solid blue trace. Measurements from (b) the full double-heterodyne architecture with the trihedral reflector similarly confirm the self-cancellation of both the 3.2GHz IF and 92.4GHz LO sources, as the orange and blue dashed traces directly overlap with their respective solid traces. The small discrepancy of the 200 MHz BB Rx signal is hypothesized to be due to mechanical vibrations.

With the phase noise self-cancellation of the 3.2GHz IF and 92.4GHz LO sources confirmed, subsequent analysis focuses solely on the PSD of the 200MHz BB Rx signal. The effects of the utility heaters and FAWT are investigated under two configurations. In the first, the heaters are elevated on a platform to match transceiver height (43"), ensuring that the heated flow directly intersects the beam path (Fig. 5.11). In the second, the heaters are lowered onto the ground, where the generated heat remains below the beam, resulting in negligible temperature

gradients along the propagation path. For both configurations, measurements are performed in (i) the 'still' condition where both the heaters and FAWT are turned off, (ii) just the heaters on, (iii) the FAWT is turned on to an intensity of 40% with the heaters, and (iv) the heaters are turned off, while the FAWT is kept at 40%. Temperature measurements are made using the plastic thermal screen positioned at the center of the FAWT and the FLIR T560 IR camera.

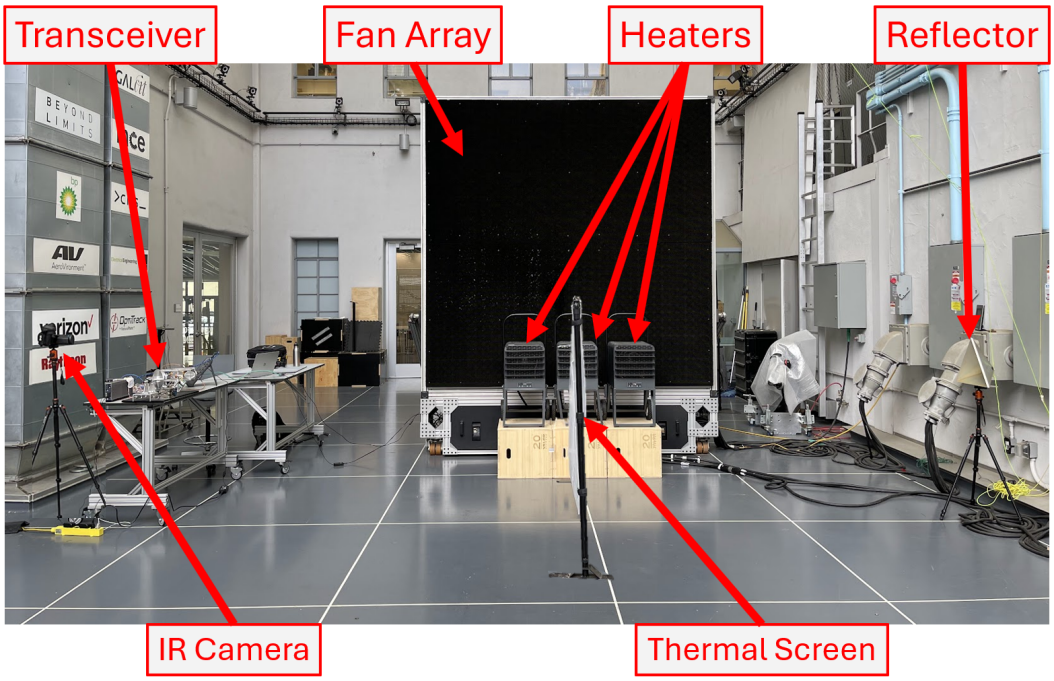

Figure 5.11: Experimental setup in CAST with the heaters elevated in front of the FAWT, along with (i) the transceiver and trihedral reflector, and (ii) IR camera and plastic thermal screen for temperature measurements. This is used to conduct preliminary measurements of the effect of the utility heaters and FAWT on the PSD of the 200MHz BB Rx signal.

With the heaters elevated, the PSD measurements show a clear impact on the shape of the 200MHz BB Rx signal when the heaters and FAWT are operating (Fig. 5.12). These results also confirm the impact can only be observed with the double heterodyne architecture enabled by phase noise self-cancellation. The measurements also reveal the undesired effects that mechanical vibrations have on the PSD of the signal. Similar measurements are made with the heaters are lowered to the ground using the same operating states (Fig. 5.13). These results confirm that the increase in spectral energy occurs only when the temperature gradient aligns with the propagation path of the beam. They also reinforce the effects of the mechanical vibrations from the FAWT.

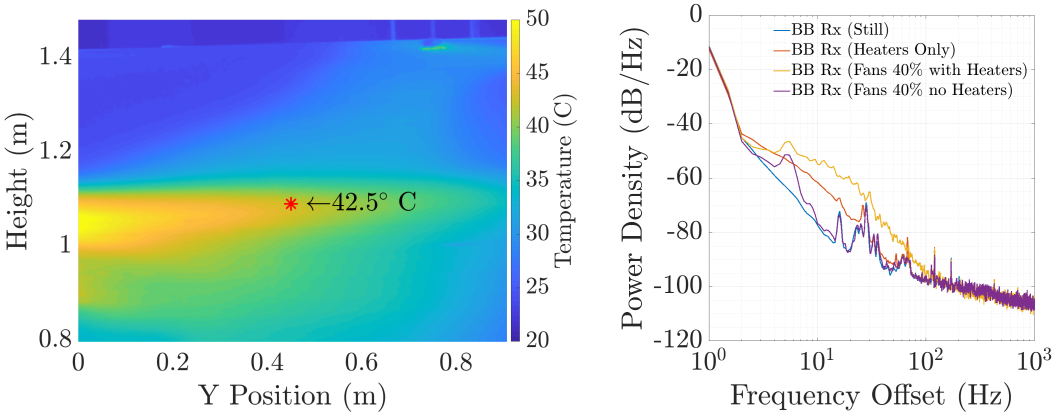

(a) (b)

Figure 5.12: Measurement results from the experimental setup in Fig. 5.11. (a) Temperature profile from the IR camera with the heaters on and FAWT intensity at 40%. The red asterisk marks the beam location and corresponding temperature. The 'Y Position' denotes the relative downstream position of the flow. (b) PSD of the 200MHz BB Rx signal under different operating states. The temperature gradient introduced from the heaters, along with their internal fans, increases the PSD relative to the 'still' state (orange vs. blue trace). With the FAWT intensity at 40%, the PSD shifts towards higher frequencies (yellow trace). When the heaters are off but the FAWT remains at 40%, a distinct bump appears near 7Hz, and is attributed to mechanical vibrations (purple trace).

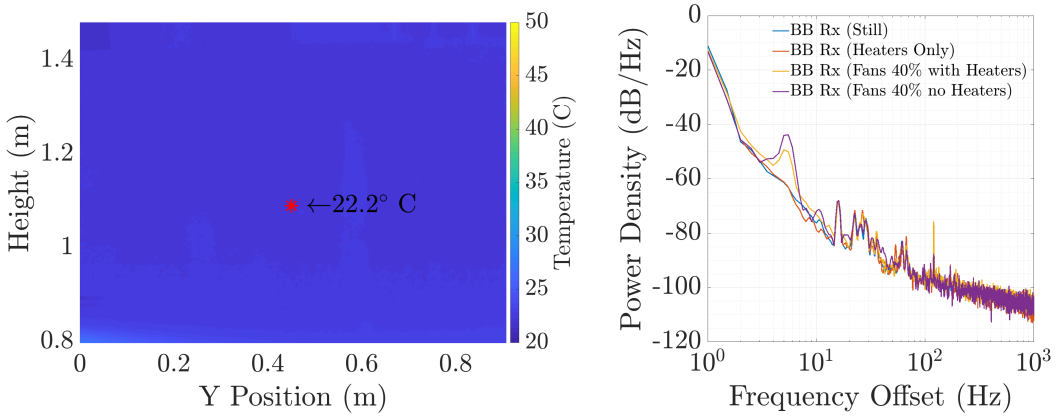

(a) (b)

Figure 5.13: Measurement results when the heaters are lowered in Fig. 5.11. The (a) temperature profile and (b) PSD measurements are similar to Fig. 5.12. With the heaters turned on but positioned below the beam path, no significant increase in spectral energy is observed in the received signal since the temperature gradients is negligible along the propagation path. Mechanical vibration effects are still present producing the distinct bump near 7Hz, but are only observed when the FAWT is operating, and not the heaters since the FAWT is significantly more powerful.

Additional tests were done to see the effect of the propagation direction relative to the wind flow. 3 measurements were performed by steering the beam orthogonal, diagonal, and parallel to the wind flow, and positioning the trihedral reflector accordingly (Fig. 5.14). The measurement results highlight a large increase in the effect of the mechanical vibrations of the FAWT felt by the reflector, since when it is placed at the diagonal and parallel positions, it is further downstream and more in line with the flow generated by the FAWT. They also reinforce the contribution of the temperature gradient, as the hot air cools further downstream resulting in less impact on the signal in the diagonal case, and no impact in the parallel case.

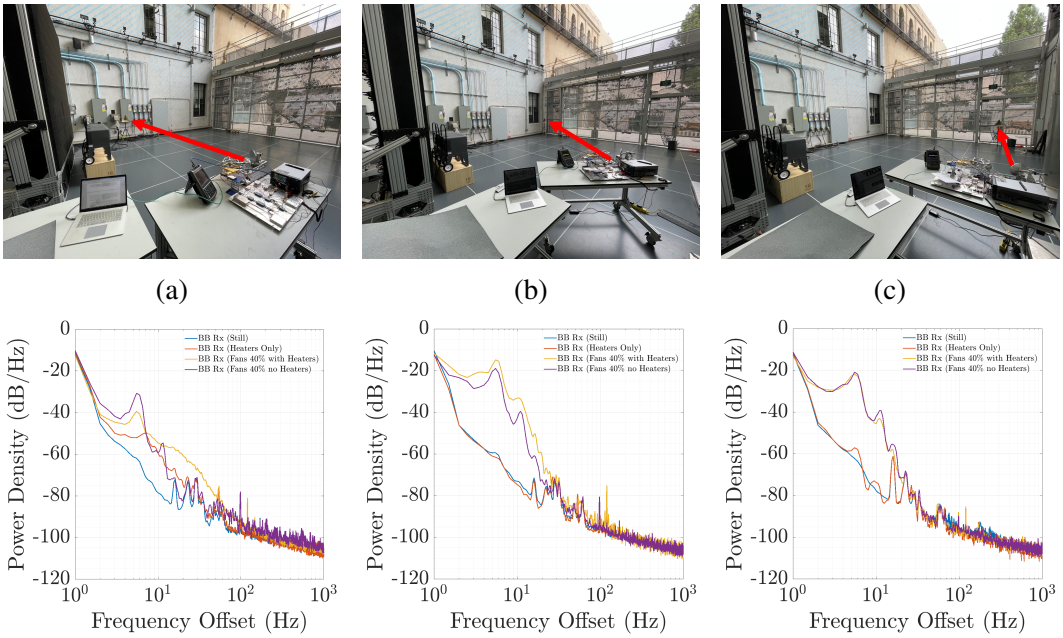

Figure 5.14: Experimental setup showing different EM beam propagation directions relative to the wind flow: (a) perpendicular, (b) diagonal, and (c) parallel, with the red arrow indicating the propagation path of the beam. Corresponding PSD measurement results are shown for (d) perpendicular, (e) diagonal, and (f) parallel propagation directions. In the perpendicular case, scintillation is maximized and mechanical vibrations effects are minimized since the beam propagation path is closest to the heaters. In the diagonal case, mechanical vibrations are very significant, with substantially less scintillation since the propagation path is further downstream and the hot air from the heaters has cooled down. In the parallel case, no scintillation is observed since the propagation path does not encounter any temperature gradients, although mechanical vibration effects remain significant. The direct impact of the wind stream from the FAWT causes the reflector to vibrate and results in significant increases in the PSD at the close-in frequencies.

All of the previous measurements were done with the gates of the CAST facility closed, which contributed significantly to mechanical vibrations since the airflow generated by the FAWT bounced off the gates and back towards the equipment. To mitigate this, all subsequent experiments were performed with the gates fully opened, allowing the flow to continue outdoors. A test to mitigate the effect of mechanical vibrations was conducted by comparing the PSD of the 200MHz BB Rx signal when the transceiver is anchored down in the 'still' condition (Fig. 5.15). The observed reduction in mechanical vibration effects motivates the use of the vibration isolation platform in subsequent experiments, along with sandbags to anchor down both the desk supporting the transceiver and the tripod of the trihedral reflector.

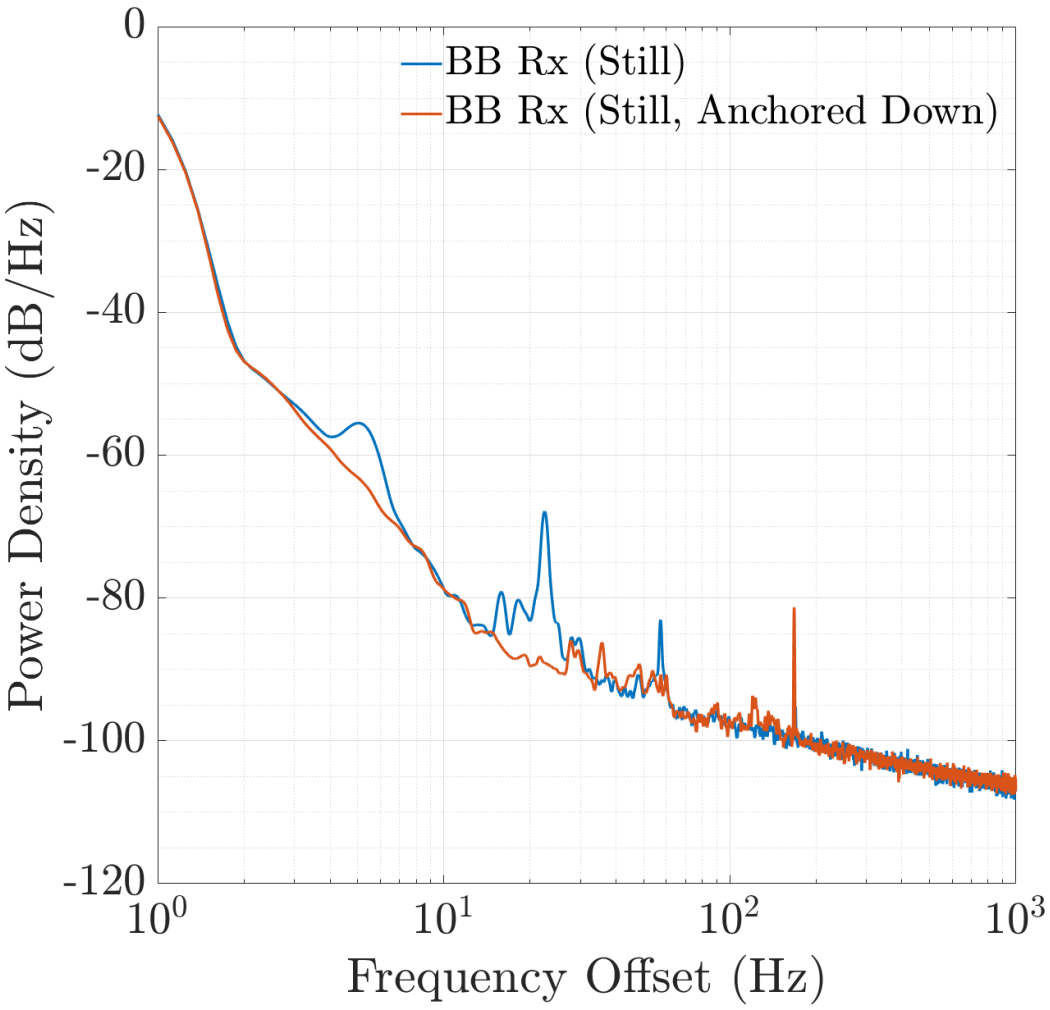

Figure 5.15: PSD measurements of 200 MHz BB Rx signal in the 'still' state without the hardware anchored down (blue trace), and with the hardware anchored down (orange trace). Anchoring the hardware significantly reduces the effects of mechanical vibrations on the PSD.

5.3 Heaters in Front

After identifying that the heaters and FAWT intensities significantly impact on the PSD of the EM signal, a series of detailed experiments were done to further analyze and characterize these effects. The first set of experiments, kept the heaters elevated on blocks and positioned in a line at the center of the FAWT (Fig. 5.16).

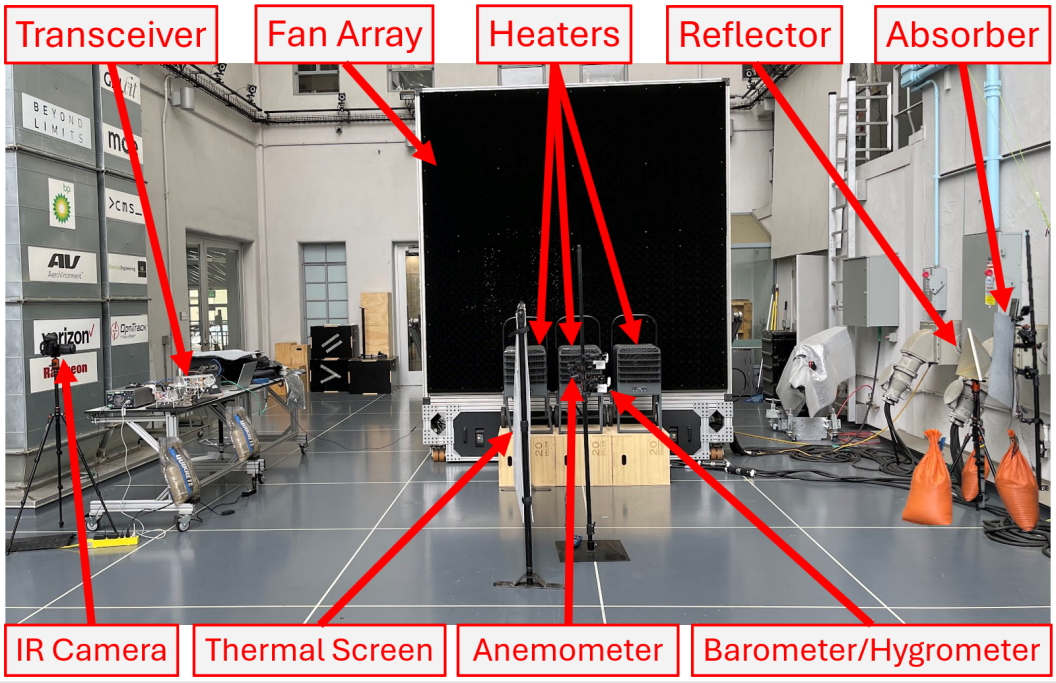

Figure 5.16: Experimental setup in CAST with heaters placed elevated in front of the FAWT, along with (i) the transceiver, reflector, and absorber, (ii) IR camera and plastic thermal screen for temperature measurements, and (iii) other meteorological sensors for pressure, humidity, and wind speed measurements. By elevating the heaters in front of the FAWT, the hot air is aligned with the propagation path of the beam. The heat distribution in the region in front of the 3 heaters was assumed to be uniform. The thermal screen and IR camera were set up in front of the heaters to capture the temperature profile. The hygrometer and vane anemometers were also placed in front of the heaters, at 2 distinct heights (43" in line with the EM beam, and 53") to measure the temperature gradient, humidity, and wind speed.

Meteorological Measurements

For simplicity, initial meteorological measurements are made from the data loggers and the IR camera and thermal screen are ignored. The devices made measurements of the temperature, relative humidity, and wind speed at 1 second intervals for 90 minutes. Every 10 minutes, the heater and FAWT state would change. The value of C_n^2 is estimated using the resulting measurements and the gradient model (Fig. 5.17).

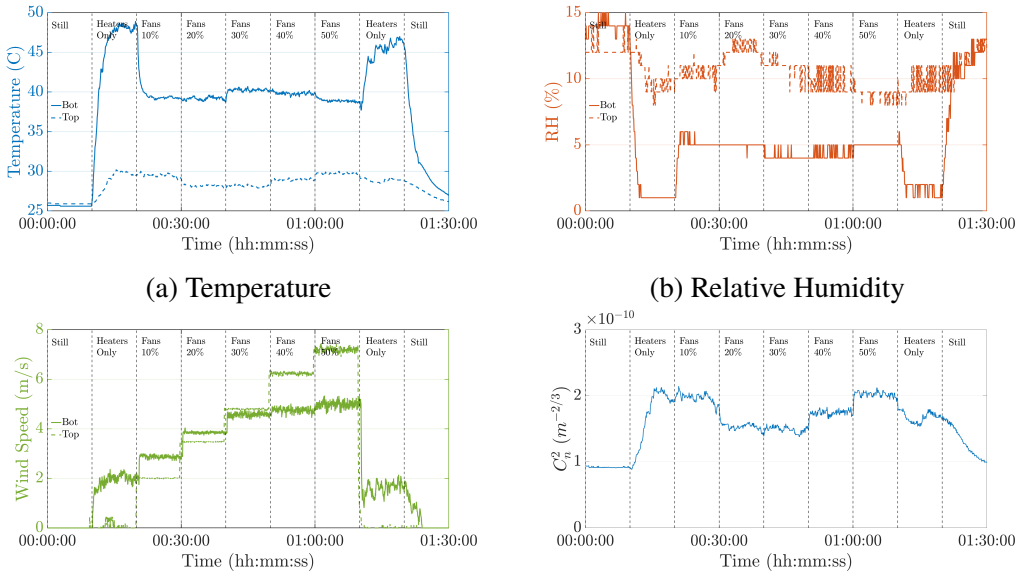

(a) Temperature

(b) Relative Humidity

(c) Wind Speed

(d) C_n^2

Figure 5.17: Meteorological measurements versus time for (a) temperature, (b) relative humidity, (c) wind speed at 2 heights (43" 'Bot' and 53" 'Top') for heaters elevated in front of the FAWT. The corresponding value of C_n^2 (d) is calculated from the temperature and relative humidity measurement results using the gradient method (Eq. 3.14). The measurements were conducted over a 90 minute period, with the heater and FAWT operating states changed every 10 minutes. The sequence begins with all equipment off to establish ambient conditions. Then, the heaters were turned on, followed by the FAWT operating at intensities from 10% to 50% in 10% increments. Finally, the FAWT is turned off, followed by the heaters being switched off to return the environment to ambient conditions.

Transceiver Measurements

Measurements of the power spectrum of the 200MHz BB Rx signal with the SA were subsequently made following the same sequence of state transitions. From these measurements, the PSD relative to the center frequency was calculated (Fig. 5.18). The results confirm that temperature gradients and wind speeds cause scintillation, which increases the PSD of the signal over and above the system phase noise, as well as causing a rightward shift towards higher frequencies for higher FAWT intensities.

The heating element of the utility heaters can be toggled on and off. The heaters themselves have a cooling mode, in which the heating element is shut off and only the fans are active. Additional measurements are made comparing the PSD in different operating states with the heating element toggled on and off (Fig. 5.19). This definitively confirms that the increase in spectral energy of the BB Rx signal is caused by the temperature gradient of the flow introduced by heating.

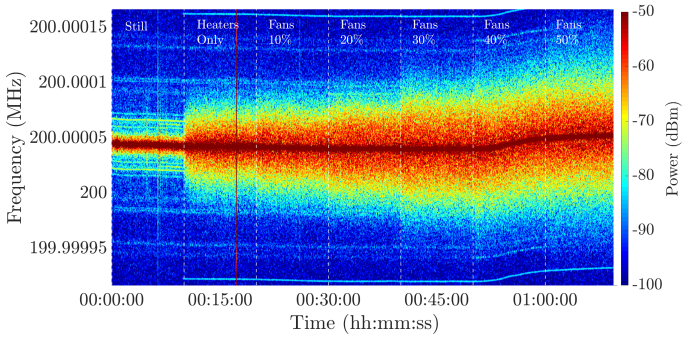

(a)

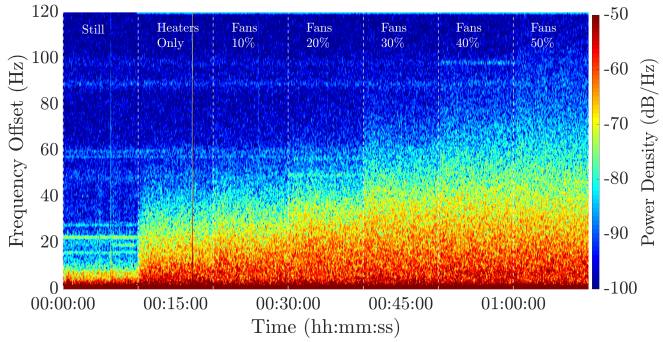

(b)

Figure 5.18: SA measurement results of the 200MHz BB Rx signal with heaters in front showing (a) the absolute power spectrum, and (b) the PSD relative to the carrier, for the same operating states in Fig. 5.17. For each state, the resulting power spectrum measurements are aggregated to produce the smoothed PSD. The drift of the carrier frequency over the measurement duration is minimal, and there is spread of spectral energy as the heaters turn on and FAWT intensity increases due to the temperature gradient and higher wind speeds.

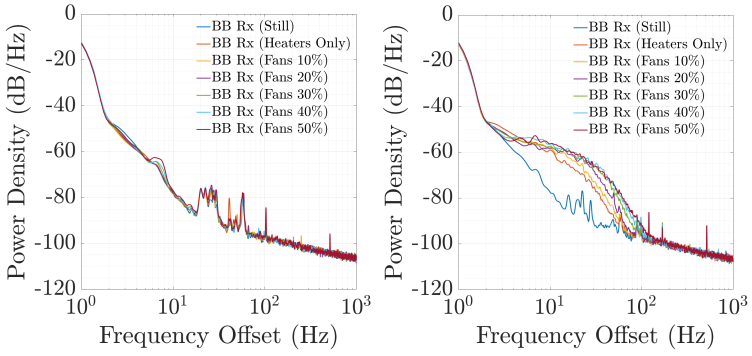

(a) (b)

Figure 5.19: SA measurement results of the 200MHz BB Rx signal PSD with heaters in front and the heating element (a) off, and (b) on. No scintillation is observed when the heating element is off and the heaters blow cool air.

Comparison with Theory

Using the averaged values of C_n^2 and wind speed from the bottom vane anemometer in each operating state, the PSD of amplitude (Eq. 3.11) and phase (Eq. 3.12) scintillations are calculated and compared with the measured PSD (Fig. 5.20).

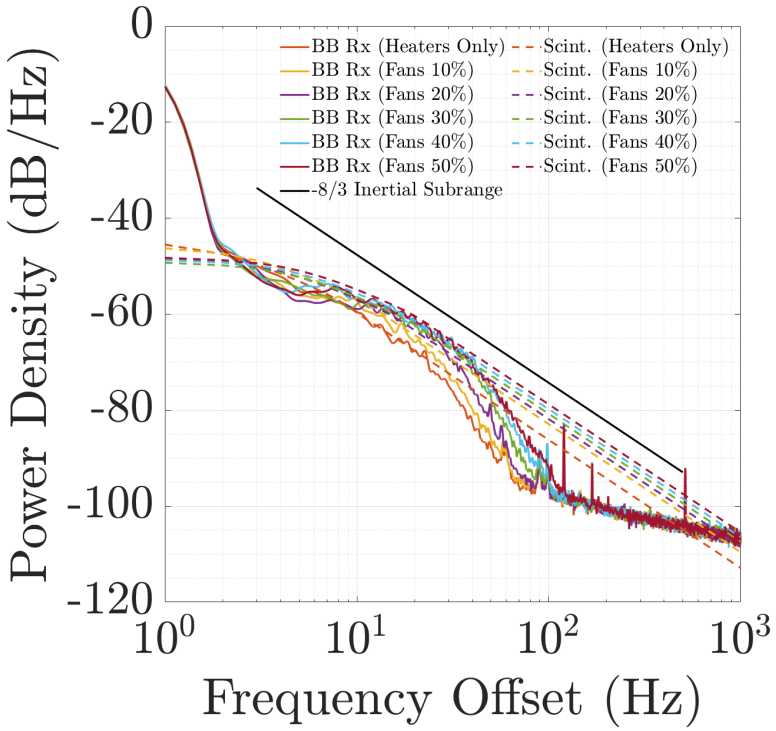

Figure 5.20: Comparison of SA PSD measurements with scintillation theory for heaters elevated in front and FAWT intensities from 0-50% in 10% increments. The solid colored traces are measured results, while the dashed traces are the corresponding scintillation PSD from the theoretical models, using the measured values of C_n^2 and v for each state. The outer scale length L_o is assumed to lie between 0.08m and 2.88m, corresponding to the characteristic dimensions of the individual fan units and overall FAWT length. Based on the measured PSD, L_o is estimated to be 0.8m. The inertial subrange with slope of -8/3 is included for comparison.

The comparison between measurement and theory show good agreement only in the 10-20Hz, and the results highlight 2 key considerations. First, the PSD at close-in frequencies below 5Hz is dominated by the internal oscillator phase noise of the SA. Second, for frequencies above 20Hz, the measured PSD falls off at a rate faster than the theoretical -8/3 slope predicted by scintillation theory in the inertial subrange, before flattening out at the thermal noise floor above 100Hz. These observations motivated improvements to both the experimental setup and theoretical modeling. A more accurate instrument was required to measure the close-in frequencies, and the scintillation model was updated to includes the dissipation region of turbulence.

FSPN and Vibration Isolation Platform

To address the challenge of accurately measuring the PSD at close-in frequencies, the Rohde&Schwarz FSPN phase noise analyzer was employed, which utilizes the cross-correlation method to measure very low levels of phase noise. A comparison of the measurement capabilities between the SA and the FSPN highlights the limitations of the SA (Fig. 5.21). Therefore, all subsequent measurements were done using the FSPN, which accurately measures the PSD in the close-in frequency range.

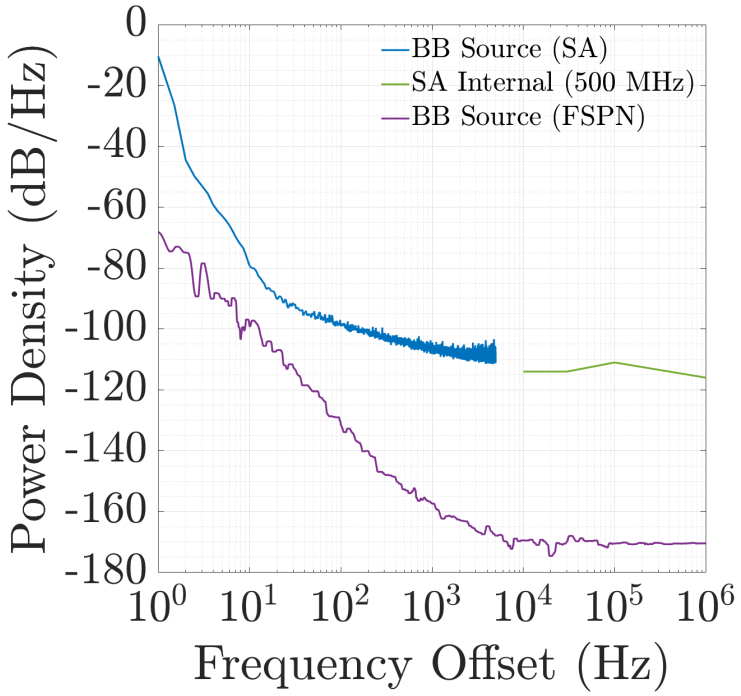

Figure 5.21: Comparison of the measured PSD of the 200MHz BB source using the SA (blue trace), and the FSPN (purple trace). The internal oscillator phase noise of the SA at 500MHz, the closest frequency reference to 200MHz available in the datasheet, is shown for comparison (green trace). This provides insight into the limited measurement capabilities of the SA. Although the datasheet only reports phase noise values for offset frequencies above 10kHz, interpolation indicates that the SA measurements are limited by the instrument's internal phase noise rather than the actual source phase noise. In contrast the FSPN reveals the much lower true phase noise of the BB source.

To further improve the accuracy of the PSD measurements, the vibration isolation platform is added to the experimental setup for subsequent measurements. PSD measurements are made for the different operating states using the FSPN, with and without the vibration isolation platform (Fig. 5.22).

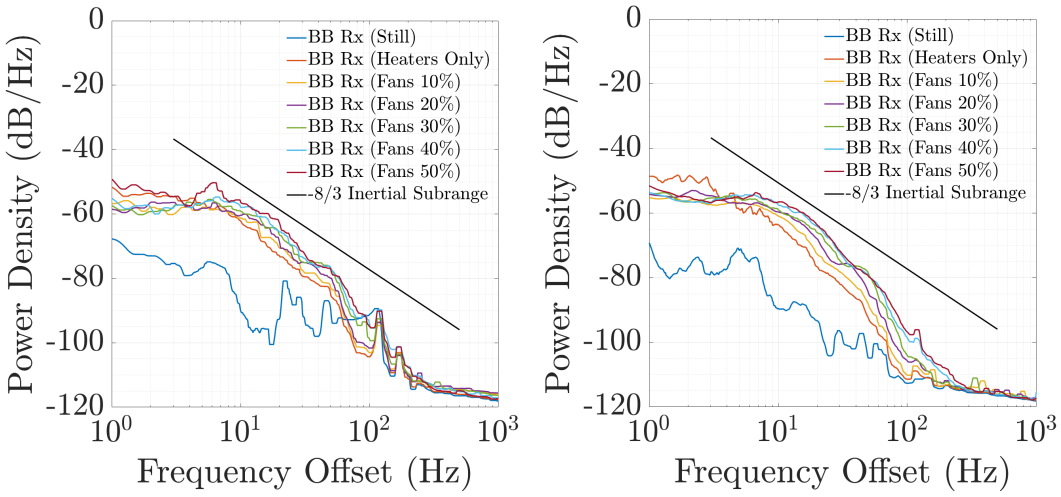

Figure 5.22: PSD measurements using the FSPN with heaters elevated in front (a) without and (b) with the vibration isolation platform. The vibration isolation platform is able to filter out the effect of mechanical vibrations at frequencies above 7Hz. The inertial subrange with -8/3 slope is included for reference.

Combination Anemometer Measurements

To address the steeper dropoff of the PSD relative to the -8/3 slope predicted by the inertial subrange, it is necessary to characterize the dynamics of the flow and the associated turbulent scales. Measurements from the vane anemometer lack sufficient frequency resolution to provide meaningful insight into the turbulence dynamics of the flow. Therefore, the combination anemometer is employed to perform high speed wind measurements within the flow (Fig. 5.23).

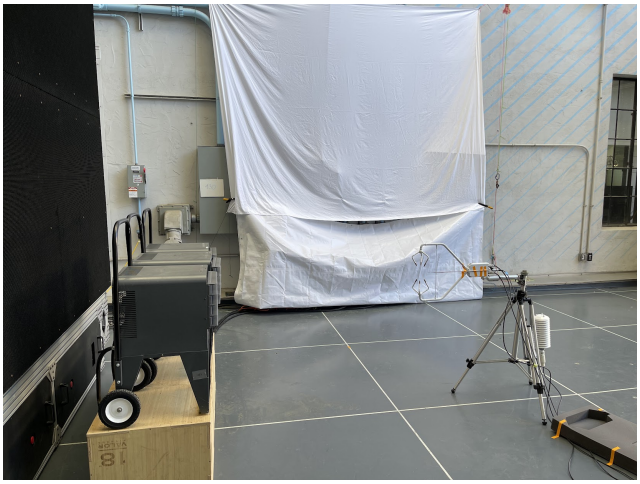

Figure 5.23: Experimental setup for combination anemometer with heaters elevated in front. The anemometer is positioned in the center of the FAWT at a height of 43".

Measurements are done in the same states as the transceiver experiments, both with and without the heaters (Fig. 5.24). The PSD of wind speed fluctuations confirms that the eddies dissipate rapidly in the flow, indicating that the dissipation region must be accounted for in the theoretical model. Furthermore, positioning the heaters elevated in front of the FAWT obstruct the flow, reducing the controllability, versatility, and configurability of the FAWT. This motivates the subsequent experiments in which the heaters are positioned on the sides of the FAWT to allow more effecting manipulation of the flow.

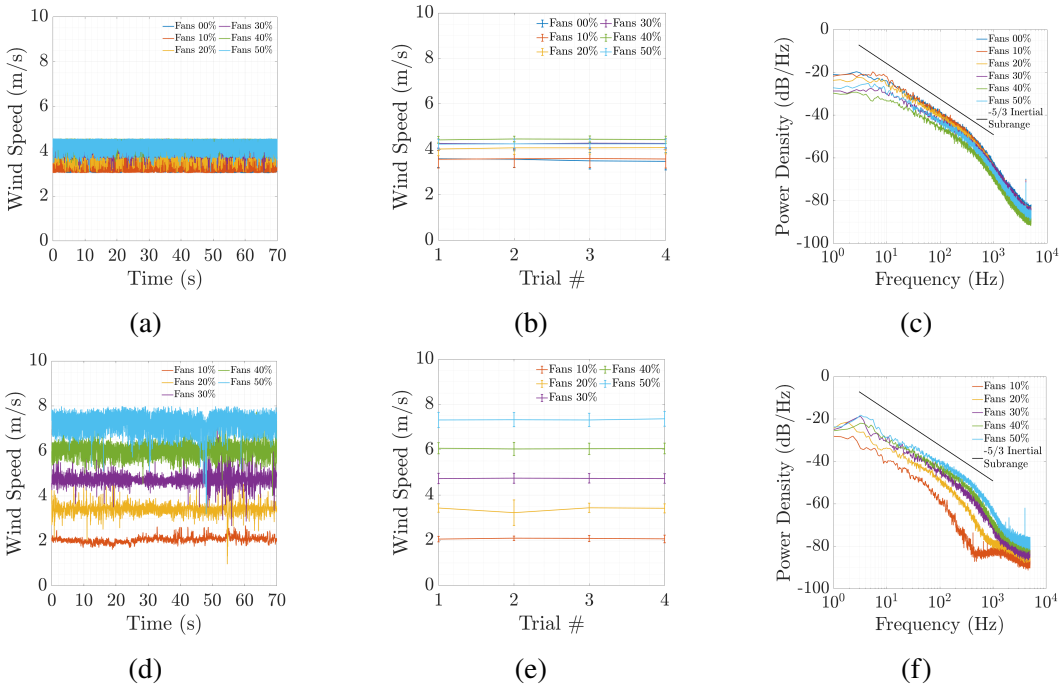

Figure 5.24: Combination anemometer measurement results for (a) time domain, (b) statistics, and (c) PSD for heaters elevated in front of the FAWT, and for (d) time domain, (e) statistics, and (f) PSD in the absence of the heaters. Measurements of FAWT 0% isolate the internal heater fans. 4 measurement trials are performed for each operating state, with each trial lasting 70s at a sampling rate of 10kS/s. The time domain and PSD plots show a single trial, while the statistics represent all 4 trials. The PSD illustrate all 3 regions of turbulence: energy input region, inertial subrange, and dissipation region, with the Kolmogorov model for the inertial subrange (black trace with -5/3 slope) included for reference. The elevated heaters in front of the FAWT obstruct the airflow, shown by the negligible increase in both mean wind speed and PSD with increasing FAWT intensity. In contrast, when the heaters are absent, the mean wind speed and PSD increase monotonically with FAWT intensity, confirming the unobstructed influence of the FAWT on the flow.

5.4 Heaters Aside

The second experimental configuration placed 2 heaters on the sides of the FAWT, both directed inwards towards the center (Fig. 5.25). This section presents the transceiver PSD measurement results and multiday experiments that demonstrate the consistency and repeatability of this experimental setup. The corresponding meteorological measurements are detailed and applied to the theoretical scintillation model, enabling accurate characterization of the measured PSD.

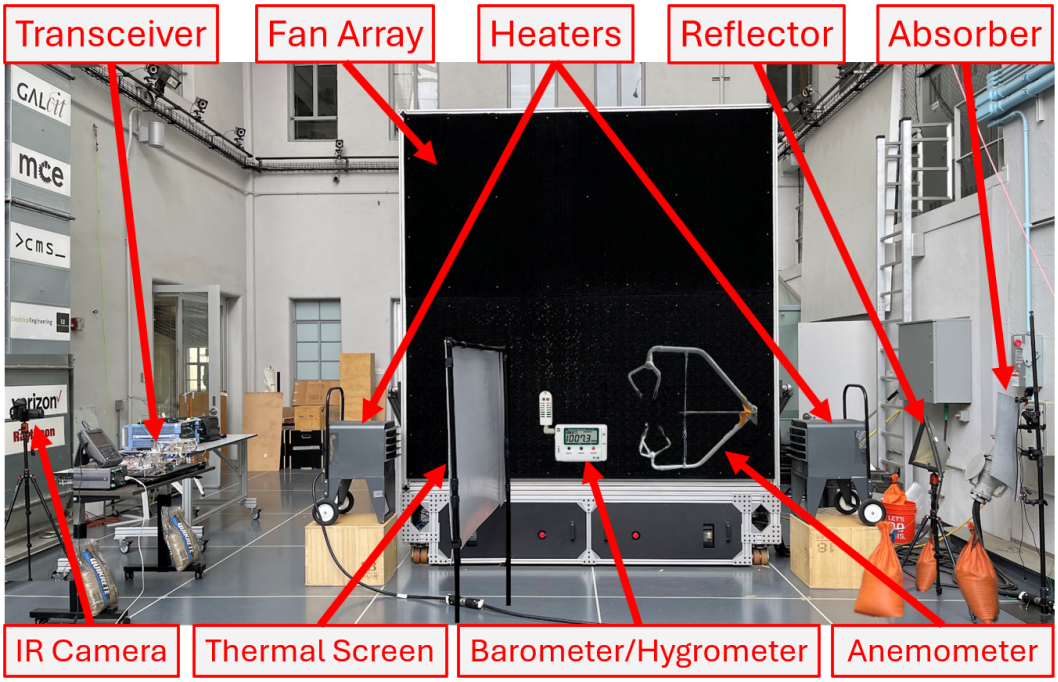

Figure 5.25: Experimental setup in CAST with heaters placed at the sides of the FAWT, along with (i) the transceiver, reflector, and absorber, (ii) IR camera and plastic thermal screen for temperature measurements, and (iii) meteorological sensors for pressure, humidity, and wind speed measurements. By placing the heaters on the sides of the FAWT facing towards the center, the flow from the FAWT is unobstructed while still inducing a large temperature gradient in the flow.

Transceiver Measurements

Transceiver measurements are made in the 'Still' state, as well as with the heaters turned on and the FAWT operated at intensities from 10-50% in 10% increments (Fig.5.26). In this configuration, there is no 'Heaters Only' state, since the hot air is directed towards the center of the FAWT rather than across the propagation path of the beam. As a result, no significant scintillation is observed with just the heaters. To smooth out the spurious fluctuations due to mechanical vibrations and additional noise, a custom floor filter is applied to the PSD measurements (Fig. 5.27).

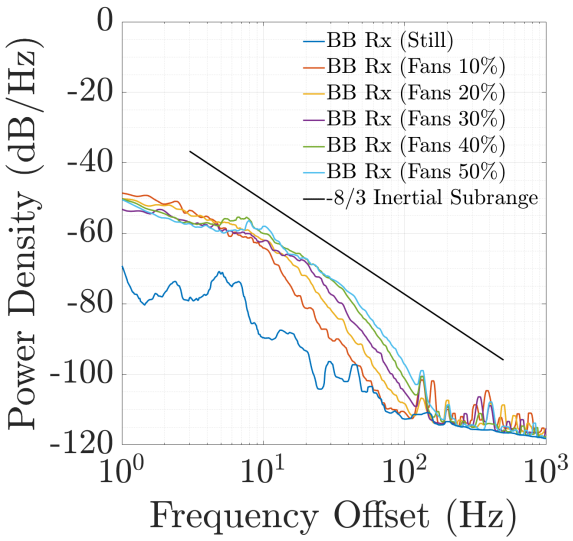

Figure 5.26: PSD measurements for heaters aside, illustrating the contributions from scintillation over an above system noise. The PSD increases and shifts rightward towards higher frequencies with increasing FAWT intensities. This is consistent with theory, as faster wind speeds produce higher frequency turbulent eddies. The steeper dropoff at larger frequencies corresponds to eddies entering the dissipation region. The inertial subrange with -8/3 slope is included for reference.

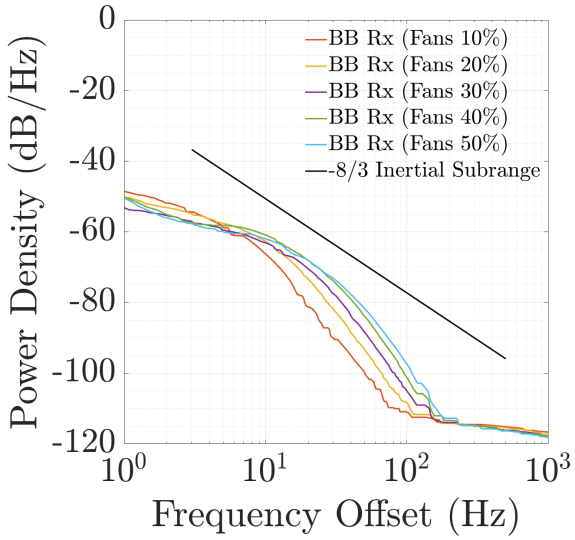

Figure 5.27: PSD measurements for heaters aside after applying a custom floor filter, which operates by retaining the minimum value of the PSD as the frequency is swept from low to high. This approach leverages the fact that both $S_\chi(f)$ and $S_\varphi(f)$ are strictly decreasing functions, so any upward deviations are due to undesired effects such as mechanical vibrations and noise. These plots provide a better physically representative spectrum is captured which isolates the effects of turbulence-induced scintillation. The inertial subrange with -8/3 slope is included for reference.

The FSPN is capable of measuring both amplitude noise and phase noise of the analog input signal (Fig. 5.28). The total amplitude and phase noise is measured to include the effects of $S_\chi(f)$ and $S_\varphi(f)$ (Eq. 3.6).

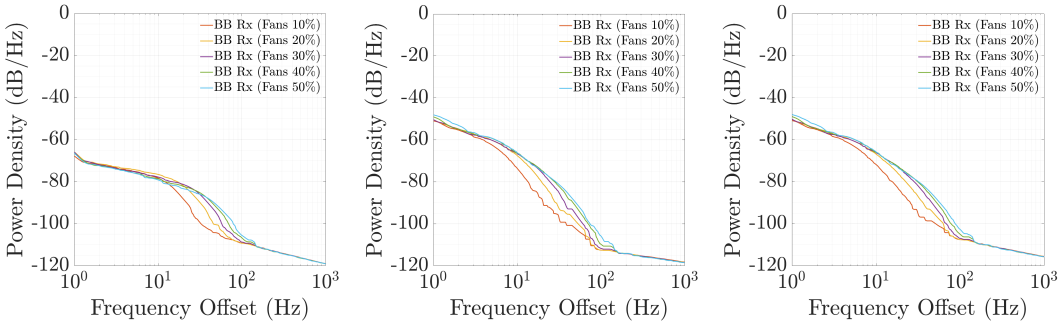

(a) (b) (c)

Figure 5.28: PSD measurements with heaters aside for (a) amplitude, (b) phase, and (c) total (amplitude + phase) noise. The phase noise dominates over the amplitude noise, which is consistent with $S_\chi(f)$ and $S_\varphi(f)$ from the theory (Fig. 3.2).

Multi-Day Experiments

To verify the consistency and repeatability of this experimental setup, multiple experiments were done across 6 separate days using the heaters aside configuration (Appendix A.4). For each experiment, the setup was fully cleared and reassembled to determine how much human error and variations in ambient conditions impacted the measurement results. This procedure was also necessary because the CAST facility is a shared research space for a wide range of projects, and no single experiment can permanently occupy the facility that could disrupt other research activities.

To quantify the consistency of the experimental results across multiple days, 2 metrics are used. The first metric is the integral of the PSD over a truncated frequency range, which serves as a proxy for the variance of scintillation:

$$\sigma^2(f_1, f_2) = \int_{f_1}^{f_2} PSD(f)df \tag{5.1}$$

Ideally, integrating the scintillation PSD across all frequencies yields the variance, which is independent of the mean wind speed [33]. In this experimental setup, however, close-in frequencies are corrupted by mechanical vibrations, while higher frequencies are dominated by the residual system phase noise floor. Therefore, the integral is computed between intermediate frequencies $f_1 = 20Hz$ and $f_2 = 100Hz$, after first applying the floor filter (Fig. 5.29a).

The second metric is the frequency at which the PSD curve crosses the -90dB/Hz level. This value gives insight into the mean wind speed of the turbulent flow, since for a fixed C_n^2, the mean wind speed shifts the PSD curve left and right. The -90dB/Hz level is chosen as a convenient threshold that lies sufficiently above the noise floor (Fig. 5.29b).

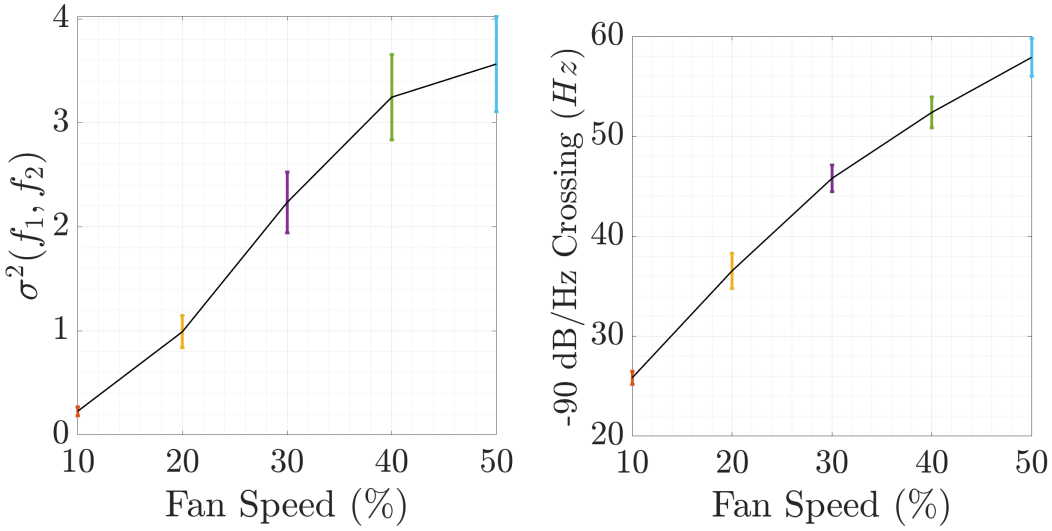

(a) (b)

Figure 5.29: Statistics of PSD curve characteristics across 6 days of experiments: (a) integral of the PSD over a truncated range, and (b) the -90dB/Hz crossing point. The error bars can be due to minor setup differences or changing background conditions such as ambient temperature, humidity, and wind. The general trend indicates that the experiment is repeatable and consistent, particularly for lower fan speeds in (a) and all fan speeds in (b).

Temperature Measurements

Temperature measurements were made by placing the plastic thermal screen in 3 different positions in the flow, along the propagation path of the beam (Fig. 5.30). This is because the heat flow is not uniform across the entire FAWT when the heaters are placed on the sides. So, to capture more spatial resolution, temperature profiles of the flow are made in multiple positions in order to obtain an average value of the temperature gradients along the propagation path of the beam.

The corresponding temperature gradient is then calculated at each pixel in the IR camera measurement (Fig. 5.31). The resulting values of C_n^2 at each position for different FAWT intensities are averaged to give a representative value to be applied to the scintillation PSDs (Fig. 5.32).

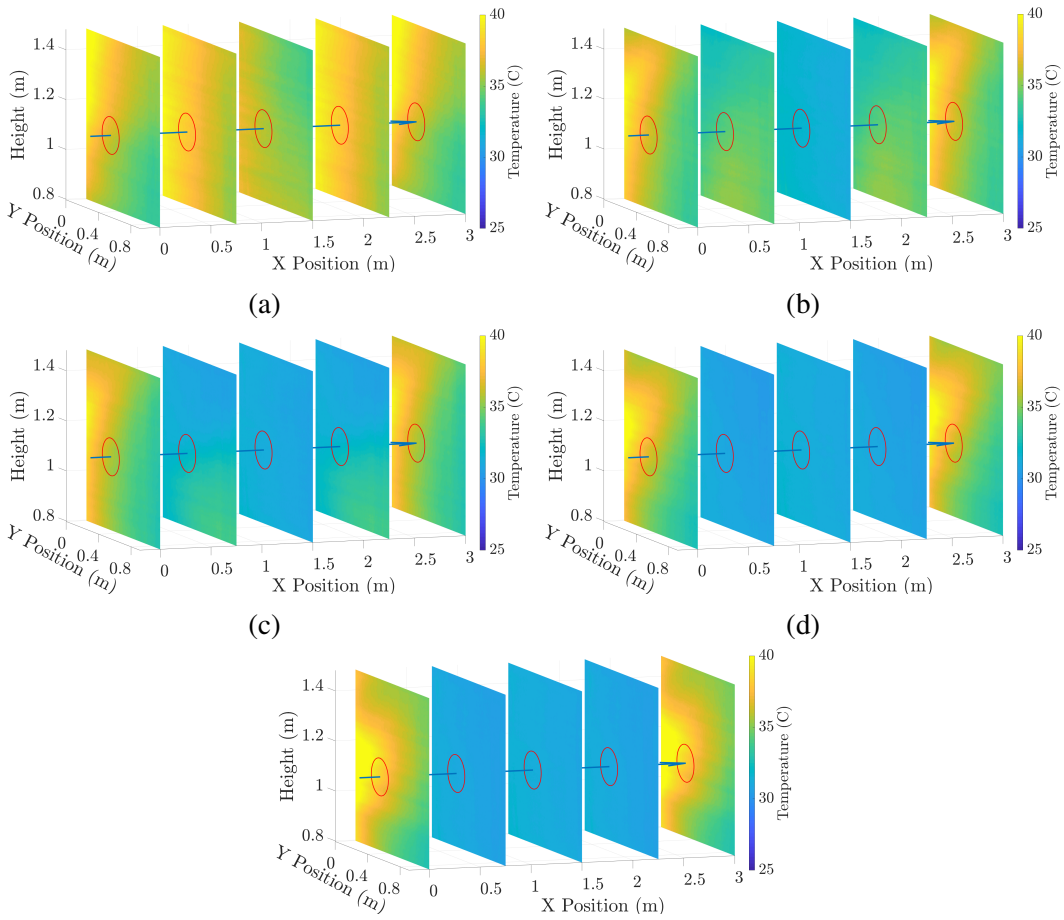

Figure 5.30: Temperature measurements at 5 positions within the flow for heaters aside and FAWT intensities of (a) 10%, (b) 20%, (c) 30%, (d) 40%, and (e) 50%. The 'X' position is referenced to the left edge of the FAWT in Fig. 5.25, while the 'Y' position is the downstream distance from the face of the FAWT. The red circle denotes the cross sectional area of the EM beam, and the blue arrow indicates its propagation path through the flow. The flow is assumed to be symmetric, so the temperature profiles at X=0m is mirrored at X=3m, and those at X=0.75m are mirrored at X=2.25m. As the FAWT intensity increases, the central regions of the flow cool due to the FAWT overpowering the heaters, with the majority of the temperature gradient concentrated at the edges closest to the heaters.

Wind Speed Measurements

Wind speed measurements were made by placing the combination anemometer at the same 3 'X' positions as the thermal screen (Fig. 5.33). Previously, a single measurement at the center of the FAWT was sufficient to represent the entire flow, since the flow was assumed to be uniform (Fig. 5.24). However, now it is important to determine how the flow dynamics are affected by the heaters on the sides.

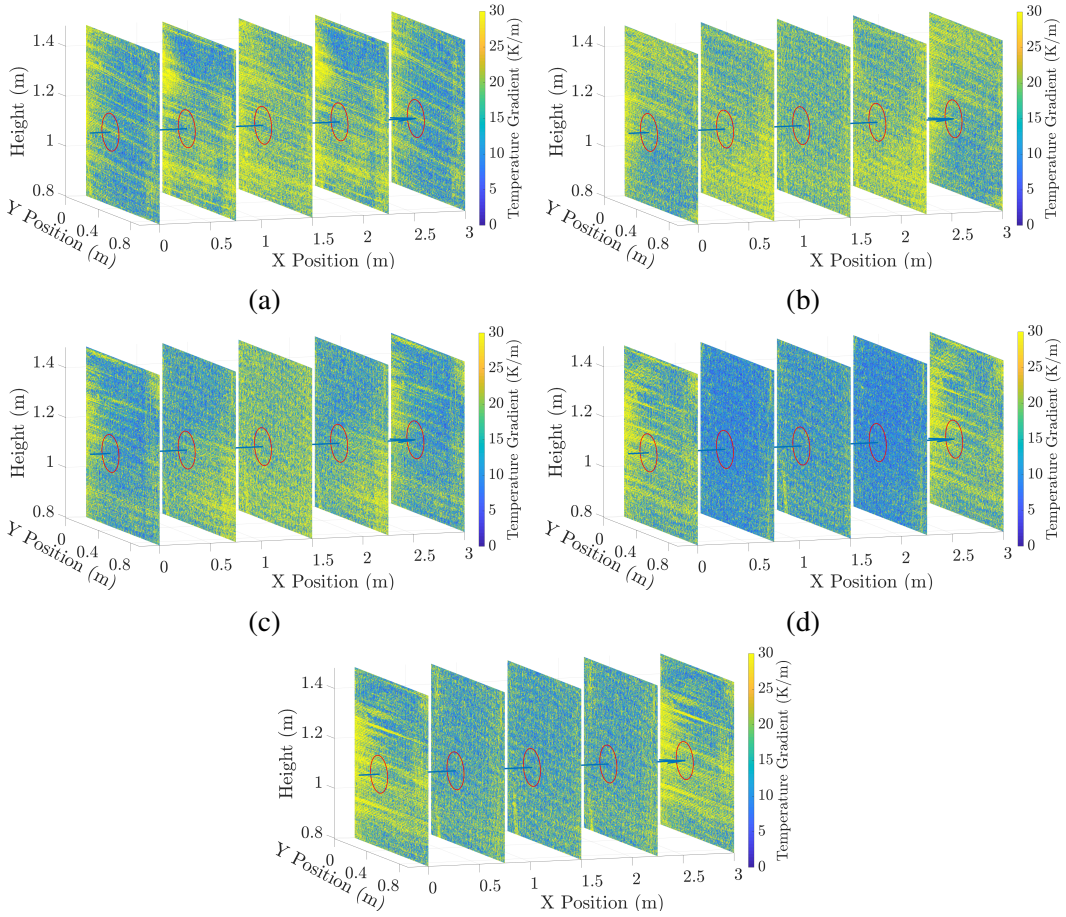

Figure 5.31: Temperature gradients at 5 positions within the flow for heaters aside and FAWT intensities of (a) 10%, (b) 20%, (c) 30%, (d) 40%, and (e) 50%, with 'X' and 'Y' positions, red circle, and blue arrow defined in Fig. 5.30. The overall magnitude of the temperature gradient is averaged across the cross sectional area of the beam and used to calculate C_n^2 using the gradient method (Eq. 3.14).

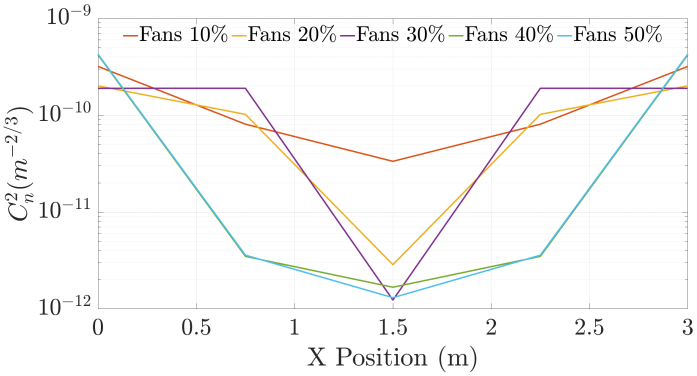

Figure 5.32: Estimate of C_n^2 at each position in the flow for different FAWT intensities using the gradient method (Eq. 3.14). The 'X' position is defined in Fig. 5.30.

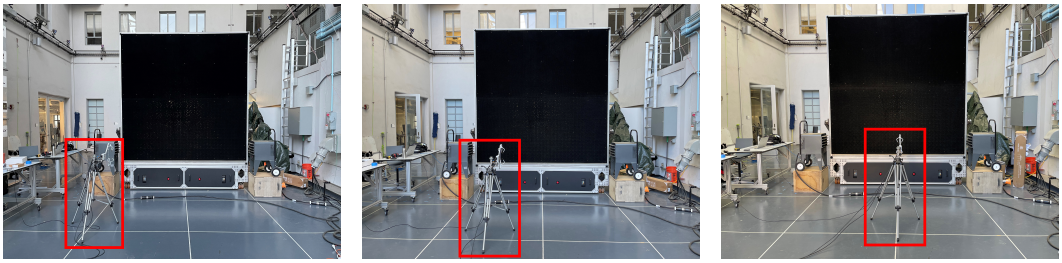

(a) (b) (c)

Figure 5.33: Positioning of combination anemometer, at 'X' positions defined in Fig. 5.30: (a) at X=0m to capture the shear layer boundary of the FAWT, (b) X=0.75m to capture the effects of both the heaters and the FAWT, and (c) X=1.5m at the very center of the FAWT. The flow is assumed to be symmetrical across the length of the FAWT, so only the left side is measured.

Measurement results are presented at each position for the time domain (Fig. 5.34), statistics (Fig. 5.35), and PSD (Fig. 5.36), with the heating element of the heaters turned on and off in order to gain insight on whether or not the temperature is acting as an active or passive quantity in terms of the flow dynamics.

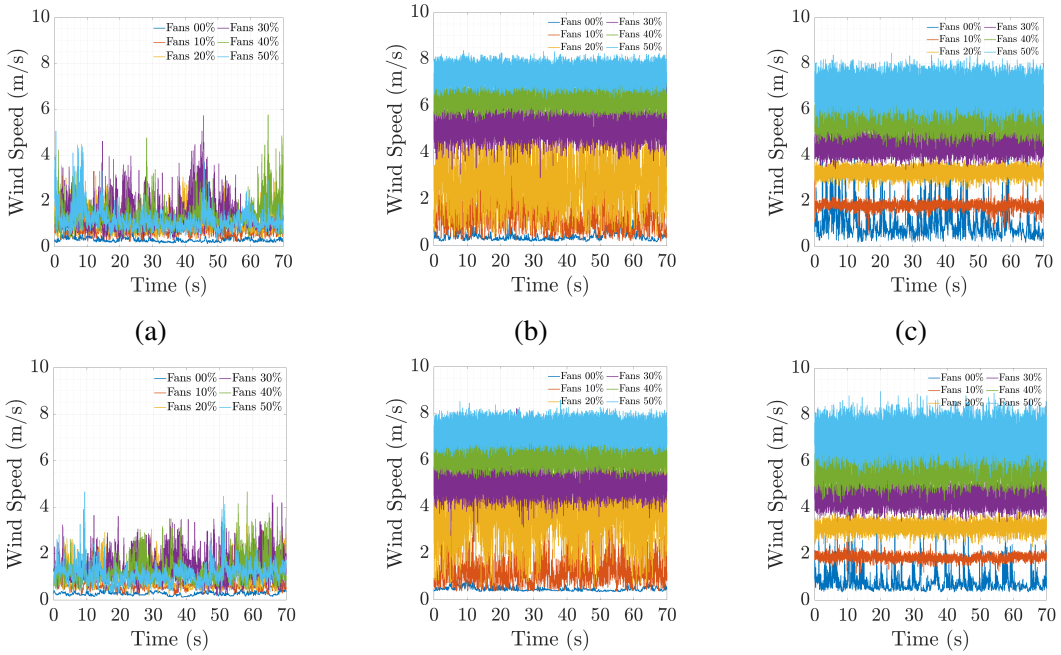

Figure 5.34: Time domain wind speed measurements for heaters aside with the heating element on, blowing hot air, at 'X' positions (a) 0m, (b) 0.75m, and (c) 1.5m, and with the heating element off, blowing cool air, at 'X' positions (d) 0m, (e) 0.75m, and (f) 1.5m. 4 measurement trials are performed for each operating state, with each trial lasting 70s at a sampling rate of 10kS/s. A single trial is shown.

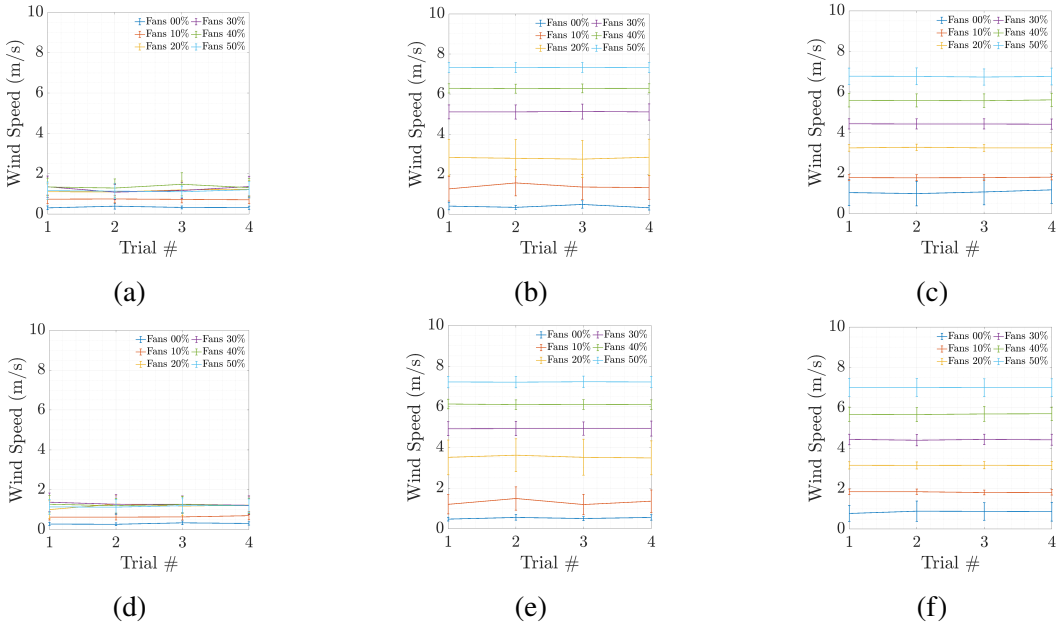

Figure 5.35: Statistics of wind speed measurements for heaters aside with the heating element on, blowing hot air, at 'X' positions (a) 0m, (b) 0.75m, and (c) 1.5m, and with the heating element off, blowing cool air, at 'X' positions (d) 0m, (e) 0.75m, and (f) 1.5m. 4 measurement trials are performed for each operating state, with each trial lasting 70s at a sampling rate of 10kS/s.

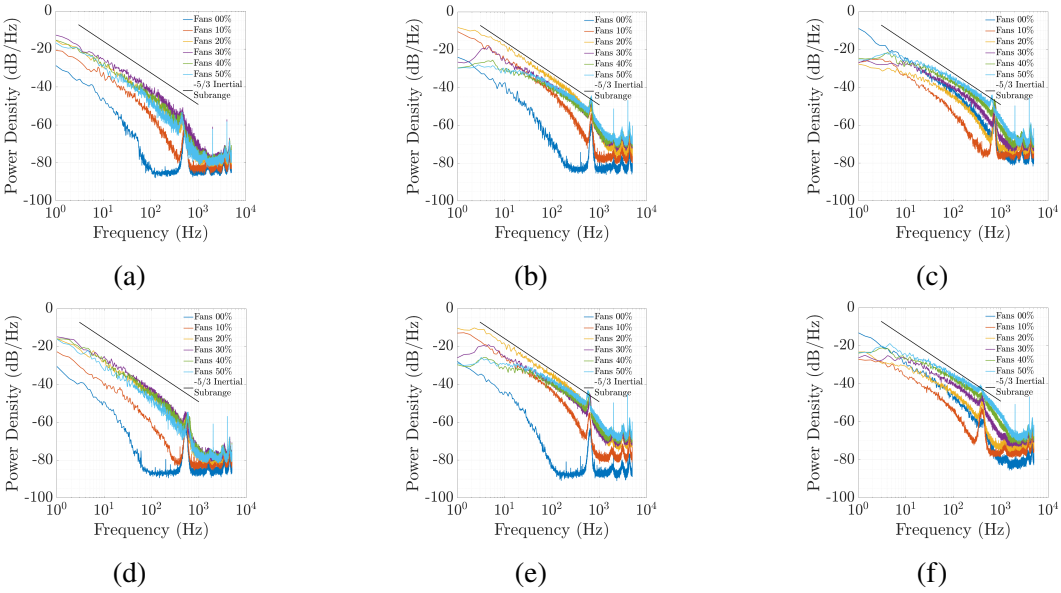

Figure 5.36: PSD of wind speed measurements for heaters aside with the heating element on, blowing hot air, at 'X' positions (a) 0m, (b) 0.75m, and (c) 1.5m, and with the heating element off, blowing cool air, at 'X' positions (d) 0m, (e) 0.75m, and (f) 1.5m. 4 measurement trials are performed for each operating state, with each trial lasting 70s at a sampling rate of 10kS/s. A single trial is shown.

The following insights are obtained from these measurement results. First, measurements at X=0m show negligible increases in mean wind speed when the FAWT is activated. This suggests that the measurement location lies slightly outside the main flow path of the FAWT, resembling a wake region. Therefore these measurements provide limited information, aside from capturing minor interactions at the boundary of the FAWT. Second, measurements at X=0.75m highlight the influence of the heaters, especially at FAWT intensities of 10-20%. At these lower intensities, the internal fans of the heaters produce flows of comparable strength to the FAWT. The interaction between the orthogonal flows from the heaters and FAWT enhances mixing and leads to larger fluctuations in the measured wind speed. This behavior represents a new observation that was not captured in the previous measurements without the heaters (Fig. 5.24). Third, the measurement results at X=1.5m closely resemble the previous measurements without the heaters, except when the FAWT is off only the heaters are operating. In this case, the 2 opposing heater flows collide at the center of the FAWT and spread out towards the combination anemometer, resulting in stronger turbulence. However, once the FAWT is activated, its flow redirects the flow from the heaters perpendicular to the beam propagation path, leaving the central region dominated by the FAWT.

Furthermore, there is insignificant differences between when the heating element is turned off or on. To show this more clearly, the PSDs are smoothed out and the plots with and without the heating element are plotted together (Fig. 5.37). This is an indication that the flow is dominated by forced convection of the flow itself, rather than natural convection from heat transfer. An estimate of the Richardson number (<0.04) also confirms this. Finally, The value of ε is calculated using spectral curve fitting with the Kolmogorov 5/3 power law at each location, and a representative value is calculated using a weighted average (Fig. 5.38).

5.5 Comparison with Theory and Development of Empirical Model

To establish an accurate quantitative link between the measured transceiver PSD and the meteorological parameters, the theoretical models of $S_\chi(f)$ (Eq. 3.7) and $S_\varphi(f)$ (Eq. 3.8) are employed. The refractive index structure constant C_n^2 along the propagation path is obtained from the IR camera temperature measurements (Fig. 5.32), while the representative value of the energy dissipation rate ε (Fig. 5.38) and mean wind speed v are derived from the combination anemometer measurements. The computed values of $S_\chi(f)$ and $S_\varphi(f)$ are compared with the measured PSD of the 200MHz BB Rx signal (Fig. 5.39).

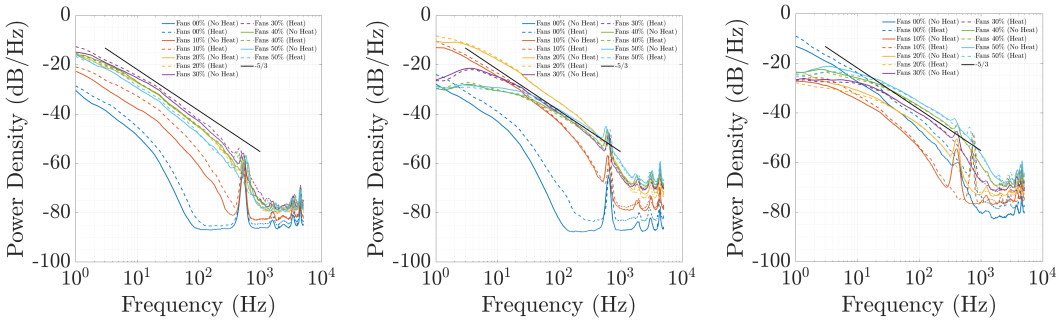

Figure 5.37: Comparison of wind speed PSDs with the heating element on and off at 'X' positions (a) 0m, (b) 0.75m, and (c) 1.5m. The PSDs are smoothed for better comparison. Near identical PSDs across all FAWT intensities suggests that temperature acts as a passive scalar, and the flow dynamics are dominated by forced convection of the FAWT.

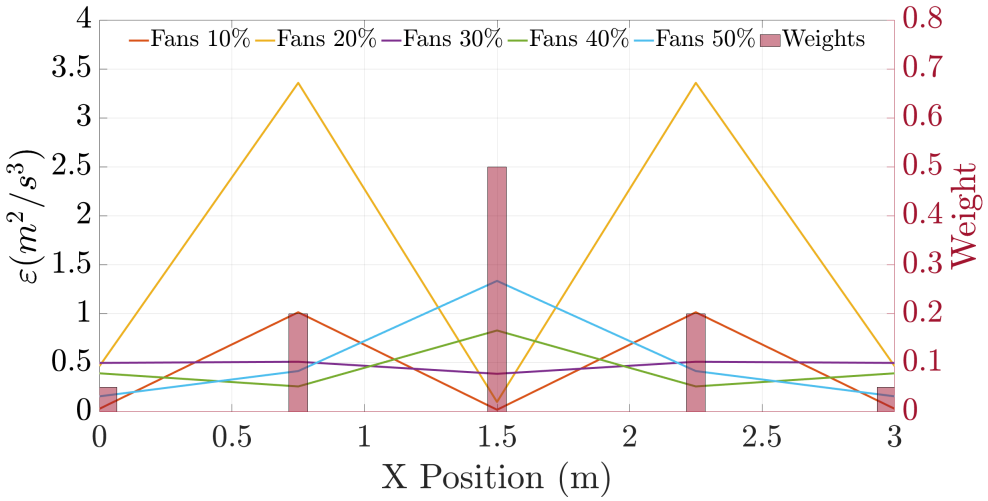

Figure 5.38: Estimated energy dissipation rate ε at different 'X' positions in the flow with heaters aside for different FAWT intensities. The relative weights used at each position for the weighted average is also shown. Note that, only for Fans 10%, the weights at 0.75m and 2.25m are 0.4, and the weight at 1.5m is 0.1. This is estimated for the portion of the propagation path that is dominated by each CTA measurement. At low FAWT intensities, the majority of the flow has dynamics similar to CTA measurements at 'X'=0.75m. Once the FAWT intensity increases, the FAWT overpowers the internal fans of the heaters and thus more of the flow is similar to CTA measurements at 'X'=1.5m.

The importance of resolving the flow dynamics at finer spatial resolution, rather than assuming uniform conditions along the entire propagation path, is demonstrated by the discrepancy between measurement and theory when using the ε values calculated in the absence of the heaters (Fig. 5.40).

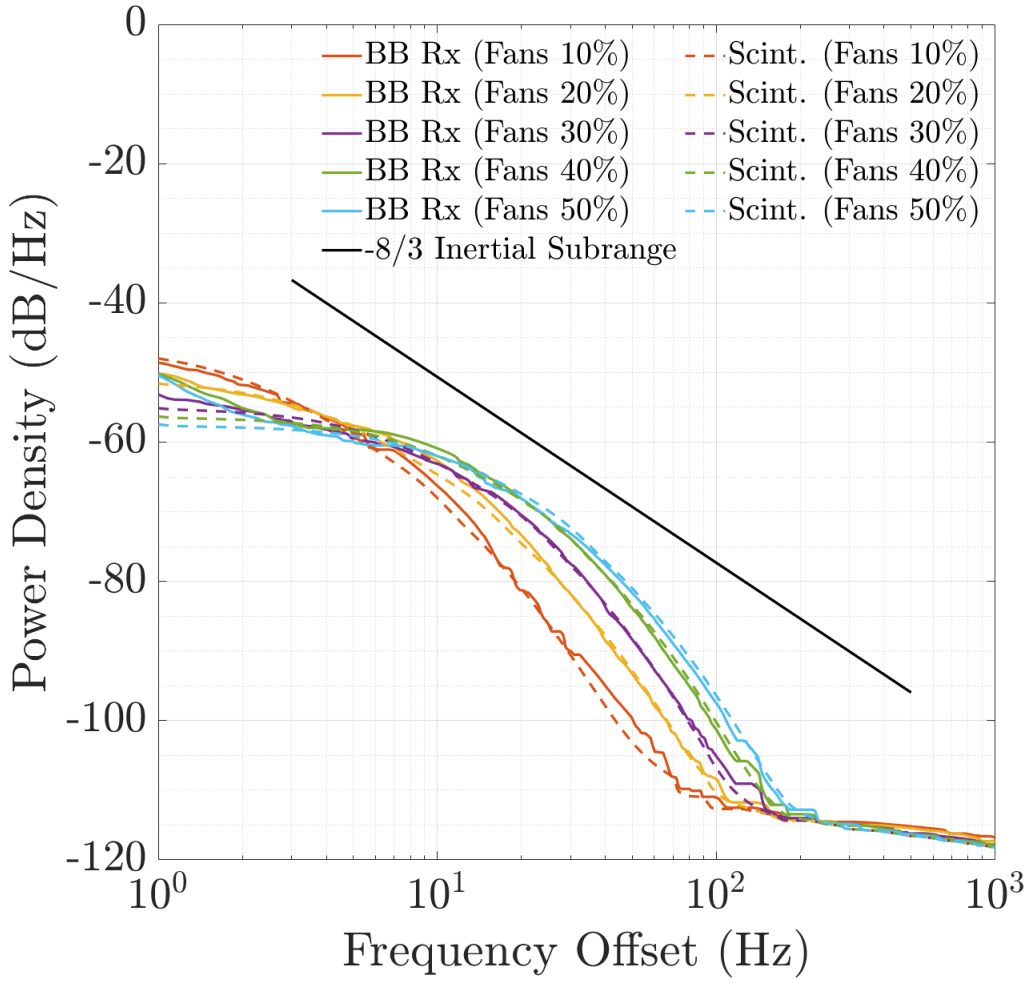

Figure 5.39: Measured PSD (solid traces) vs scintillation theory (dashed traces), where the energy dissipation rate ϵ is estimated from combination anemometer measurements in the presence of heaters (Fig. 5.38), C_n^2 is estimated from temperature measurements (Fig. 5.30), and $\alpha = 130$ in the dissipation function (Eq. 3.21) is empirically determined to best fit the measurements. Inertial subrange with -8/3 slope is included for comparison. The results show a good fit across all fan intensities. The discrepancies at the lower frequencies are due to unfiltered mechanical vibrations that could not be mitigated by the custom floor filter nor the vibration isolation platform.

Furthermore, the inclusion of the dissipation region is necessary. As discussed previously with the heaters in front using the SA measurements, the steeper dropoff of the PSD compared to the -8/3 slope predicted in the inertial subrange at higher frequencies indicates that the higher frequency eddies are leaving the inertial subrange (Fig. 5.41). Therefore, the energy input region, inertial subrange, and dissipation region, must be included to accurately model the scintillation effects in this experimental setup.

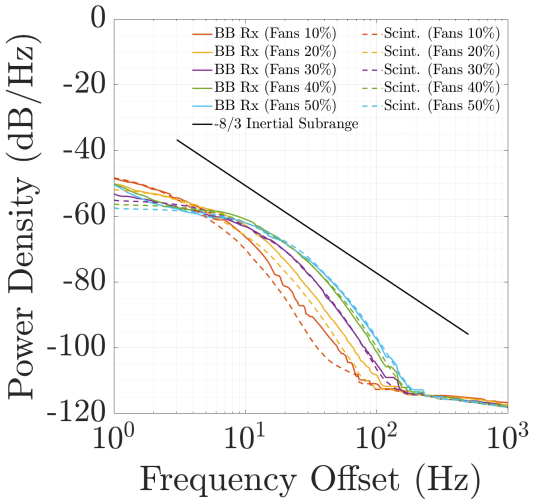

Figure 5.40: Measured PSD (solid traces) compared with scintillation theory (dashed traces), where the energy dissipation rate ε is estimated from combination anemometer measurements in the absence of heaters (Fig. 5.24f), and C_n^2 is estimated from temperature measurements (Fig. 5.30). The theoretical plots exhibit a larger deviation from the measured plots for FAWT intensities of 10-20% This is because the heaters increase turbulence intensity and the value of ε at the lower fan speeds, which is not captured in these theoretical estimates. Inertial subrange with -8/3 slope is included for comparison.

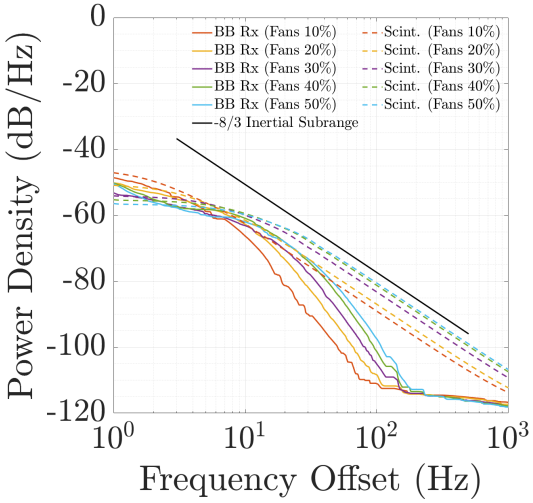

Figure 5.41: Measured PSD (solid traces) compared with scintillation theory (dashed traces), where the model is calculated without including the dissipation region, using only the mean wind speed v from vane anemometer measurements, and C_n^2 estimated from temperature measurements (Fig. 5.30). The theoretical model without the dissipation region diverges significantly from the measured results at higher frequencies. Inertial subrange with -8/3 slope is included for comparison.

The consistency and controllability of this experimental setup resulted in the establishment of an accurate empirical model to describe the measured PSD. The distinct characteristics of the PSD provides a unique opportunity for the remote sensing of turbulence. Quantitative parameters can be extracted from the shape and characteristics of the measured PSD. The 4 main quantities that determine the shape of the PSD when dominated by scintillation are C_n^2, v, L_o, and ε (Fig. 5.42). Since C_n^2 and v are measured more easily, the values of L_o and ε can be deduced from the characteristics of the measured PSD.

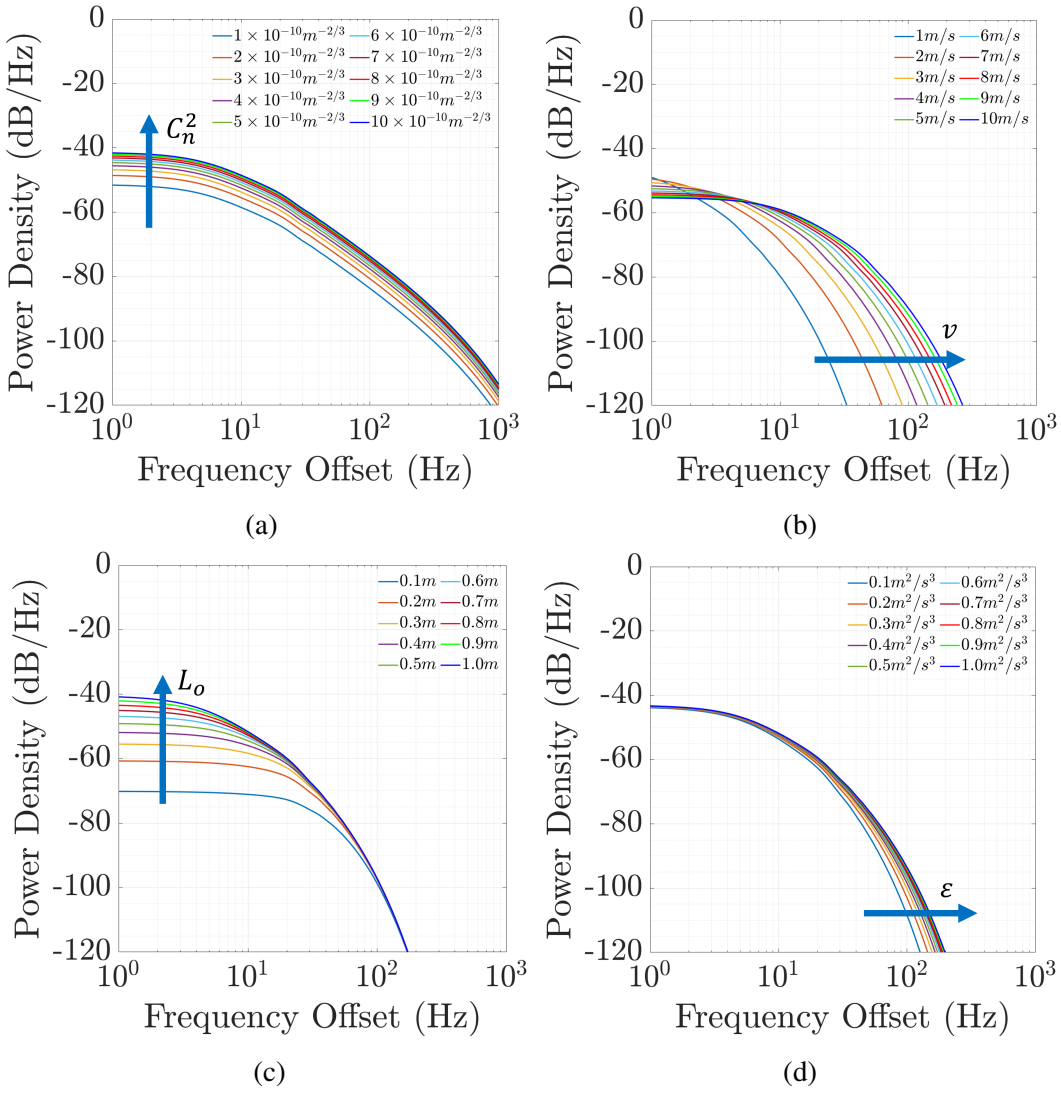

Figure 5.42: Overview of model parameters (a) refractive index structure constant C_n^2, (b) mean wind speed v, (c) outer scale length L_o, and (d) energy dissipation rate ε, and their effects on the shape of the scintillation PSD curve. Insight of the flow can be gain from the characteristic curves and fitting the model parameters. The blue arrows point towards how the curves change as the parameter increases.

Chapter 6

CONCLUSION AND FUTURE WORK

6.1 Conclusion

This thesis has presented a novel experimental setup for characterizing the effects of atmospheric turbulence on a 95GHz signal. Temperature gradients were shown to increase the power spectrum, while controlled wind speeds generated by the fan array wind tunnel shifted the spectrum toward higher frequencies. Scintillation effects were consistently verified across multiple heater configurations and wind conditions, demonstrating the robustness and versatility of this experimental setup. An empirical model was developed, extending existing theoretical frameworks by incorporating meteorological measurements to characterize scintillation. Establishing this setup in a controlled environment enables reliable study of atmospheric effects on mmWave propagation, and opens new opportunities for consistent, repeatable investigations of scintillation.

6.2 Future Work

The work presented in this thesis highlights the cumulative iterations, analyses, and measurement results, demonstrating the promise of this novel experimental setup. While significant progress has been achieved in its development, implementation, and modeling, several improvements and future directions remain to be pursued.

The most important improvement to this setup is the development of a method to generate a uniform temperature gradient without obstructing the FAWT. The initial plan was to position the heaters in a row behind the FAWT so that the hot air would be entrained into the flow along its entire length, thereby producing a uniform temperature gradient and a flow field purely dictated by the FAWT without any obstructions. However, this approach was not permitted by CAST management due to the risk of overheating the computer modules controlling the fans, which are located at the rear of the FAWT. If an alternative method for generating a uniform heat flow along the entire length of the FAWT can be developed, it would enable a broad range of new experiments. In particular, the ability to fully leverage the spatial programmability of the FAWT would provide deeper insight into the effects of different types of turbulent flows. This would enable controlled investigations of shear flows, random turbulence across different length scales, and vortex shedding

generated by a cylindrical object in the flow, all of which could be studied with precise and systematic measurements.

Future work could also focus on reintroducing the effects of humidity gradients. In this work, humidity was largely neglected due to challenges in controlled generation and limitations in spatial measurement resolution. Developing a method to accurately generate and characterize measurable humidity gradients would incorporate it into the C_n^2 model, providing an additional parameter for analysis. According to the gradient model, specific humidity gradients could significantly increase C_n^2, allowing improved characterization across a broader frequency range.

A minor improvement would be to replace the 3.2GHz source a low phase noise PLDRO, rather than replying on the Valon 5009a. This substitution would ensure the phase noise contributions from all sources in the double heterodyne system in minimized, thereby improving overall measurement accuracy.

One aspect of the measurement results that is still unclear is determining which temperature gradient direction primarily induces the observed scintillation. In the experimental configuration with the heaters aside, the overall flow is not uniform along the entire propagation path, so it is unclear whether the values of C_n^2 or ε can be meaningfully averaged over the propagation path. In a more uniform flow that can be approximated as homogeneous and isotropic, the orthogonal component of the refractive index fluctuations is expected to induce scintillation. However, in this setup it is unclear whether the vertical temperature gradient or flow-wise temperature gradient that is the main contributor. Furthermore, the role of the boundary layers between hot and cool air is not well understood, and their influence on the scintillation intensity remains an open question.

Although the repeatability and consistency of the experimental setup have been investigated, a deeper study of long term measurements would be valuable. Throughout this work, ambient conditions were documented but their effects were not explicitly analyzed. The results indicate that the observed scintillation was primarily induced by the overall temperature gradient, however ambient conditions could also play a role. Investigating how the measurement results vary over diurnal or even seasonal shifts could provide further insight into the influence of environmental factors. Such studies are challenging in this particular experimental setup because CAST is a shared facility, making it difficult to reserve the space for extended periods due to ongoing projects from multiple groups.

Another aspect of improving the experimental setup is to explore different carrier frequencies or modulation schemes. In this work, only a single tone at 95.4GHz was used, primarily due to the availability of W-band hardware and simplicity required during the initial bring-up of this novel experiment. Extending the model to other frequency bands would provide insight into how smaller scale eddies affect different wavelengths. Furthermore, incorporating modulation scheme, such as adding a chirp to the carrier signal or some other spectral broadening approaches, would enable more sophisticated measurement techniques. The use of a single CW tone was chosen for simplicity, and the inclusion of frequency modulation could allow investigation of backscattering phenomena. Additionally, this setup could be adapted to explore higher frequencies regimes, including sub-THz, THz, and free space optical bands, offering opportunities for broader characterization of turbulence effects across the EM spectrum.

Finally, while the experimental setup presented here is novel, the practical applicability in isolation is limited. The primary benefit lies in providing a controlled laboratory environment to characterize turbulent effects, but the scalability of this approach requires further investigation. Future work should focus on extending the model and insights gained from this experimental setup to real world scenarios, assessing how these controlled measurements can inform practical applications.

BIBLIOGRAPHY

[1] H. J. Liebe, "Mpm—an atmospheric millimeter-wave propagation model," *International Journal of Infrared and Millimeter Waves*, vol. 10, no. 6, pp. 631–650, Jun. 1989, ISSN: 1572-9559. DOI: 10.1007/BF01009565. [Online]. Available: https://doi.org/10.1007/BF01009565.

[2] T. Alberti, D. Faranda, L. Rapella, *et al.*, "Impacts of changing atmospheric circulation patterns on aviation turbulence over europe," *Geophysical Research Letters*, vol. 51, no. 23, e2024GL111618, 2024, e2024GL111618 2024GL111618. DOI: https://doi.org/10.1029/2024GL111618. eprint: https://agupubs.onlinelibrary.wiley.com/doi/pdf/10.1029/2024GL111618. [Online]. Available: https://agupubs.onlinelibrary.wiley.com/doi/abs/10.1029/2024GL111618.

[3] J. Teixeira, J. R. Piepmeier, A. R. Nehrir, *et al.*, *Toward a global planetary boundary layer observing system: The nasa pbl incubation study team report*, 2021.

[4] M. Azouit, J. Vernin, R. Barletti, G. Ceppatelli, A. Righini, and N. Speroni, "Remote sensing of atmospheric turbulence by means of a fast optical method: A comparison with simultaneous in situ measurements," *Journal of Applied Meteorology and Climatology*, vol. 19, no. 7, pp. 834–838, 1980. DOI: 10.1175/1520-0450(1980)019<0834:RSOATB>2.0.CO;2. [Online]. Available: https://journals.ametsoc.org/view/journals/apme/19/7/1520-0450_1980_019_0834_rsoatb_2_0_co_2.xml.

[5] R. W. McMillan, "Atmospheric turbulence effects on radar systems," in *Proceedings of the IEEE 2010 National Aerospace Electronics Conference*, 2010, pp. 1–153. DOI: 10.1109/NAECON.2010.5712909.

[6] M. Giordani and M. Zorzi, "Satellite communication at millimeter waves: A key enabler of the 6g era," in *2020 International Conference on Computing, Networking and Communications (ICNC)*, 2020, pp. 383–388. DOI: 10.1109/ICNC47757.2020.9049651.

[7] S. Aliaga, V. Petrov, T. Singh, *et al.*, "Analysis of scintillation effects in terahertz band satellite communications for 6g and beyond," in *2025 IEEE 22nd Consumer Communications Networking Conference (CCNC)*, 2025, pp. 1–6. DOI: 10.1109/CCNC54725.2025.10976007.

[8] R. H. Ratul, S. M. Mehedi Zaman, H. A. Chowdhury, M. Z. Hassan Sagor, M. T. Kawser, and M. Muntasir Nishat, "Atmospheric influence on the path loss at high frequencies for deployment of 5g cellular communication networks," in *2023 14th International Conference on Computing Communication and Networking Technologies (ICCCNT)*, 2023, pp. 1–6. DOI: 10.1109/ICCCNT56998.2023.10307972.

[9] M. Thompson, H. Janes, L. Wood, and D. Smith, "Phase and amplitude scintillations at 9.6 GHz on an elevated path," *IEEE Transactions on Antennas and Propagation*, vol. 23, no. 6, pp. 850–854, 1975. DOI: 10.1109/TAP.1975.1141188.

[10] K. A. Norton, J. W. Herbstreit, H. B. Janes, *et al.*, *An experimental study of phase variations in line-of-sight microwave transmissions:* en, 1961-01-01 05:01:00 1961. DOI: https://doi.org/10.6028/NBS.MONO.33.

[11] M. C. Thompson Jr., H. B. Janes, and A. W. Kirkpatrick, "An analysis of time variations in tropospheric refractive index and apparent radio path length," *Journal of Geophysical Research (1896-1977)*, vol. 65, no. 1, pp. 193–201, 1960. DOI: https://doi.org/10.1029/JZ065i001p00193. eprint: https://agupubs.onlinelibrary.wiley.com/doi/pdf/10.1029/JZ065i001p00193. [Online]. Available: https://agupubs.onlinelibrary.wiley.com/doi/abs/10.1029/JZ065i001p00193.

[12] M. Thompson, L. Wood, H. Janes, and D. Smith, "Phase and amplitude scintillations in the 10 to 40 GHz band," *IEEE Transactions on Antennas and Propagation*, vol. 23, no. 6, pp. 792–797, 1975. DOI: 10.1109/TAP.1975.1141196.

[13] H. Janes, M. Thompson, and D. Smith, "Tropospheric noise in microwave range-difference measurements," *IEEE Transactions on Antennas and Propagation*, vol. 21, no. 2, pp. 256–260, 1973. DOI: 10.1109/TAP.1973.1140460.

[14] H. Janes, M. Thompson, D. Smith, and A. Kirkpatrick, "Comparison of simultaneous line-of-sight signals at 9.6 and 34.5 GHz," *IEEE Transactions on Antennas and Propagation*, vol. 18, no. 4, pp. 447–451, 1970. DOI: 10.1109/TAP.1970.1139715.

[15] R. Hill, R. Bohlander, S. Clifford, R. McMillan, J. Priestly, and W. Schoenfeld, "Turbulence-induced millimeter-wave scintillation compared with micrometeorological measurements," *IEEE Transactions on Geoscience and Remote Sensing*, vol. 26, no. 3, pp. 330–342, 1988. DOI: 10.1109/36.3035.

[16] S. Clifford, R. Hill, R. Lataitis, R. Bohlander, and R. McMillan, "Millimeter wave propagation turough the turbulent atmosphere," in *[Conference Digest] International Conference on Millimeter Wave and Far-Infrared Technology: ICMWFT '90*, 1989, pp. 1–4. DOI: 10.1109/ICMWFT.1989.763737.

[17] R. A. Bohlander, R. W. McMillan, V. T. Brady, *et al.*, "Observations of amplitude and angle of arrival scintillation in millimeter wave propagation caused by turbulence in clear air near the ground," in *1983 Eighth International Conference on Infrared and Millimeter Waves*, 1983, pp. 1–2. DOI: 10.1109/IRMM.1983.9126521.

[18] R. A. Bohlander, R. W. McMillan, D. M. Guillory, *et al.*, "Fluctuations in millimeter wave signals," in *1985 Tenth International Conference on Infrared and Millimeter Waves*, 1985, pp. 25–26. DOI: 10.1109/IRMM.1985.9126551.

[19] R. Bohlander, R. McMillan, E. Patterson, *et al.*, "Fluctuations in millimeter-wave signals propagated through inclement weather," *IEEE Transactions on Geoscience and Remote Sensing*, vol. 26, no. 3, pp. 343–354, 1988. DOI: 10.1109/36.3036.

[20] R. W. McMillan, R. A. Bohlander, R. J. Hill, and S. F. Clifford, "The Effects Of Turbulence In Clear And Turbid Atmospheres On Millimeter Wave Propagation," in *13th Intl Conf on Infrared and Millimeter Waves*, R. J. Temkin, Ed., International Society for Optics and Photonics, vol. 1039, SPIE, 1989, pp. 162–163. DOI: 10.1117/12.978384. [Online]. Available: https://doi.org/10.1117/12.978384.

[21] K. Ho, N. Mavrokoukoulakis, and R. Cole, "Wavelength dependence of scintillation fading at 110 and 36 GHz," *Electronics Letters*, vol. 13, pp. 181–183, 7 1977. DOI: 10.1049/el:19770133. eprint: https://digital-library.theiet.org/doi/pdf/10.1049/el%3A19770133. [Online]. Available: https://digital-library.theiet.org/doi/abs/10.1049/el%3A19770133.

[22] K. Ho, N. Mavrokoukoulakis, and R. Cole, "Determination of the atmospheric refractive index structure parameter from refractivity measurements and amplitude scintillation measurements at 36 GHz," *Journal of Atmospheric and Terrestrial Physics*, vol. 40, no. 6, pp. 745–747, 1978, ISSN: 0021-9169. DOI: https://doi.org/10.1016/0021-9169(78)90133-2. [Online]. Available: https://www.sciencedirect.com/science/article/pii/0021916978901332.

[23] K. Ho, N. Mavrokoukoulakis, and R. Cole, "Propagation studies on a line-of-sight microwave link at 36 GHz and 110 GHz," *IEE Journal on Microwaves, Optics and Acoustics*, vol. 3, pp. 93–98, 3 1979. DOI: 10.1049/ij-moa.1979.0022. eprint: https://digital-library.theiet.org/doi/pdf/10.1049/ij-moa.1979.0022. [Online]. Available: https://digital-library.theiet.org/doi/abs/10.1049/ij-moa.1979.0022.

[24] R. Cole, K. Ho, and N. Mavrokoukoulakis, "The effect of the outer scale of turbulence and wavelength on scintillation fading at millimeter wavelengths," *IEEE Transactions on Antennas and Propagation*, vol. 26, no. 5, pp. 712–715, 1978. DOI: 10.1109/TAP.1978.1141917.

[25] N. Mavrokoukoulakis, K. Ho, and R. Cole, "Temporal spectra of atmospheric amplitude scintillations at 110 GHz and 36 GHz," *IEEE Transactions on Antennas and Propagation*, vol. 26, no. 6, pp. 875–877, 1978. DOI: 10.1109/TAP.1978.1141961.

[26] M. Herben, "Amplitude and phase scintillation measurements on 8.2 km line-of-sight path at 30 GHz," *Electronics Letters*, vol. 18, pp. 287–289, 7 1982. DOI: 10.1049/el:19820196. eprint: https://digital-library.theiet.org/doi/pdf/10.1049/el%3A19820196. [Online]. Available: https://digital-library.theiet.org/doi/abs/10.1049/el%3A19820196.

[27] M. H. A. J. Herben and W. Kohsiek, "A comparison of radio wave and in situ observations of tropospheric turbulence and wind velocity," *Radio Science*, vol. 19, no. 4, pp. 1057–1068, 1984. DOI: https://doi.org/10.1029/RS019i004p01057. eprint: https://agupubs.onlinelibrary.wiley.com/doi/pdf/10.1029/RS019i004p01057. [Online]. Available: https://agupubs.onlinelibrary.wiley.com/doi/abs/10.1029/RS019i004p01057.

[28] M. H. A. J. Herben, "Multipath propagation experiments on 8.2-km line-of-sight path at 30 GHz," *Radio Science*, vol. 23, no. 3, pp. 419–427, 1988. DOI: https://doi.org/10.1029/RS023i003p00419. eprint: https://agupubs.onlinelibrary.wiley.com/doi/pdf/10.1029/RS023i003p00419. [Online]. Available: https://agupubs.onlinelibrary.wiley.com/doi/abs/10.1029/RS023i003p00419.

[29] I. Otung and B. Evans, "Short term distribution of amplitude scintillation on a satellite link," *Electronics Letters*, vol. 31, pp. 1328–1329, 16 1995. DOI: 10.1049/el:19950900. eprint: https://digital-library.theiet.org/doi/pdf/10.1049/el%3A19950900. [Online]. Available: https://digital-library.theiet.org/doi/abs/10.1049/el%3A19950900.

[30] I. Otung, "Prediction of tropospheric amplitude scintillation on a satellite link," *IEEE Transactions on Antennas and Propagation*, vol. 44, no. 12, pp. 1600–1608, 1996. DOI: 10.1109/8.546246.

[31] I. Otung, M. Al-Nuaimi, and B. Evans, "Extracting scintillations from satellite beacon propagation data," *IEEE Transactions on Antennas and Propagation*, vol. 46, no. 10, pp. 1580–1581, 1998. DOI: 10.1109/8.725292.

[32] A. D. Wheelon, "Electromagnetic scintillation," in Cambridge University Press, 2001, vol. 1, ch. Waves in Random Media, pp. 5–108.

[33] A. D. Wheelon, "Electromagnetic scintillation," in Cambridge University Press, 2001, vol. 1, ch. The Temporal Variation of Phase, pp. 240–316.

[34] A. D. Wheelon, "Electromagnetic scintillation," in Cambridge University Press, 2003, vol. 2, ch. The Power Spectrum and Autocorrelation, pp. 167–187.

[35] E. Martini, A. Freni, F. Cuccoli, and L. Facheris, "Derivation of clear-air turbulence parameters from high-resolution radiosonde data," *Journal of Atmospheric and Oceanic Technology*, vol. 34, no. 2, pp. 277–293, 2017. DOI: 10.1175/JTECH-D-16-0046.1. [Online]. Available: https:

//journals.ametsoc.org/view/journals/atot/34/2/jtech-d-16-0046.1.xml.

[36] E. K. Smith and S. Weintraub, "The constants in the equation for atmospheric refractive index at radio frequencies," *Proceedings of the IRE*, vol. 41, no. 8, pp. 1035–1037, 1953. DOI: 10.1109/JRPROC.1953.274297.

[37] *U.S. Standard Atmosphere: Temperature, Pressure, and Air Properties vs. Altitude — engineeringtoolbox.com*, https://www.engineeringtoolbox.com/standard-atmosphere-d_604.html, [Accessed 28-08-2025].

[38] S. B. Pope, "Turbulent flows," in Cambridge University Press, 2000, ch. The scales of turbulent motion, pp. 182–263.

[39] K. B. Cooper, R. Rodriguez Monje, R. J. Dengler, *et al.*, "A compact, low power consumption, and highly sensitive 95 GHz doppler radar," *IEEE Sensors Journal*, vol. 20, no. 11, pp. 5865–5875, 2020. DOI: 10.1109/JSEN.2020.2972535.

[40] G. Brooker, "Understanding millimetre wave fmcw radars," *1st International Conference on Sensing Technology*, Jan. 2005.

[41] R. H. Goldshmid, E. Winiarska, and D. Liberzon, "Next generation combined sonic-hotfilm anemometer: Wind alignment and automated calibration procedure using deep learning," *Experiments in Fluids*, vol. 63, no. 1, p. 30, Jan. 2022, ISSN: 1432-1114. DOI: 10.1007/s00348-022-03381-1. [Online]. Available: https://doi.org/10.1007/s00348-022-03381-1.

[42] E. Kit, A. Cherkassky, T. Sant, and H. J. S. Fernando, "In situ calibration of hot-film probes using a collocated sonic anemometer: Implementation of a neural network," *Journal of Atmospheric and Oceanic Technology*, vol. 27, no. 1, pp. 23–41, 2010. DOI: 10.1175/2009JTECHA1320.1. [Online]. Available: https://journals.ametsoc.org/view/journals/atot/27/1/2009jtecha1320_1.xml.

[43] E. Kit and B. Grits, "In situ calibration of hot-film probes using a collocated sonic anemometer: Angular probability distribution properties," *Journal of Atmospheric and Oceanic Technology*, vol. 28, no. 1, pp. 104–110, 2011. DOI: 10.1175/2010JTECHA1399.1. [Online]. Available: https://journals.ametsoc.org/view/journals/atot/28/1/2010jtecha1399_1.xml.

Appendix A

ADDITIONAL EXPERIMENTS

This appendix presents supplementary experiments conducted in the CAST facility, where various configurations were tested to provide additional insight into different aspects of the measurement setup. For each experiment, the motivation and measurement results are provided. A detailed analysis of these experiments is not included here; instead, the experiments are summarized here as supporting material to document the broader range of investigations carried out during this project.

A.1 Different Flow Patterns

Early experiments with the SA and heaters in front tried to observe the effects of different flow patterns on the measured signal. In addition to the regular uniform flow, 2 others were tested: a linear shear flow, and a sinusoidal flow (Fig. A.1).

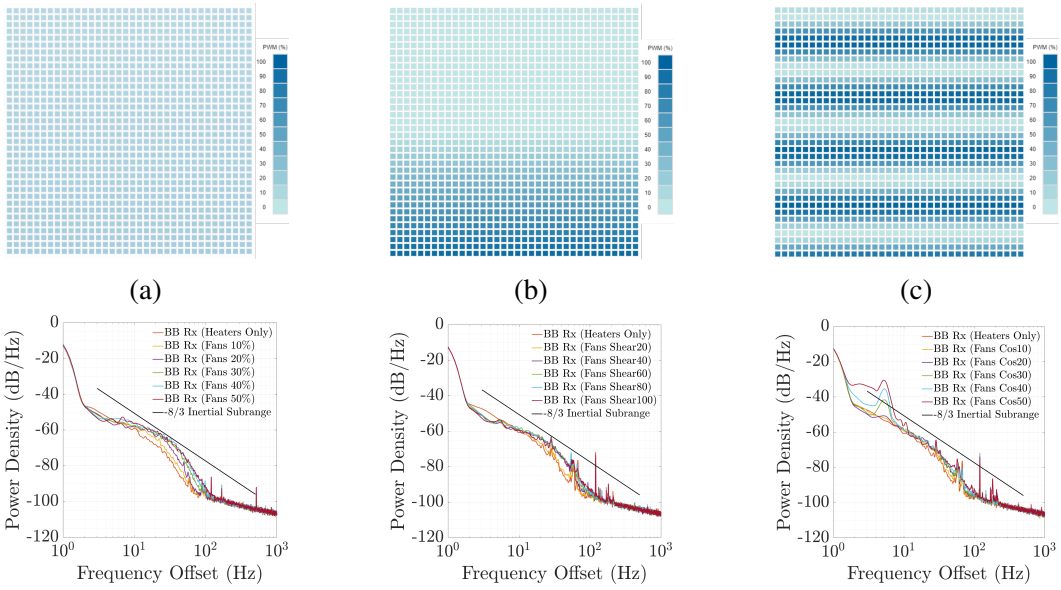

Figure A.1: FAWT flow patterns for (a) uniform flow, (b) shear flow, and (c) sinusoidal flow. The corresponding PSD measurements using the SA with heaters elevated in front for (d) uniform flow, (e) shear flow, and (f) sinusoidal flow. The shear flow is labeled as 'Shear$K$', and calculated as $K - (K/1.5)y$. The sinusoidal flow is labeled as 'Cos$K/2$', and calculated as $\frac{K}{2} + \frac{K}{2}\cos(10y)$. In both cases, K is the FAWT intensity from 20-100% in 20% increments and y is the height from the FAWT base in m. The inertial subrange of slope -8/3 is included for comparison.

A.2 Heaters in Front and Separated

To investigate whether scintillation is primarily driven by temperature gradients orthogonal to the propagation direction or the transition regions along the propagation path, the heaters were spaced apart in front of the FAWT to introduce additional transition regions (Fig. A.2). The PSD for different scenarios are measured to see if there was any effect on the measured signal (Fig. A.3).

Figure A.2: Experimental setup in CAST with heaters elevated in front of the FAWT, separated to be evenly spaced out across the length of the FAWT.

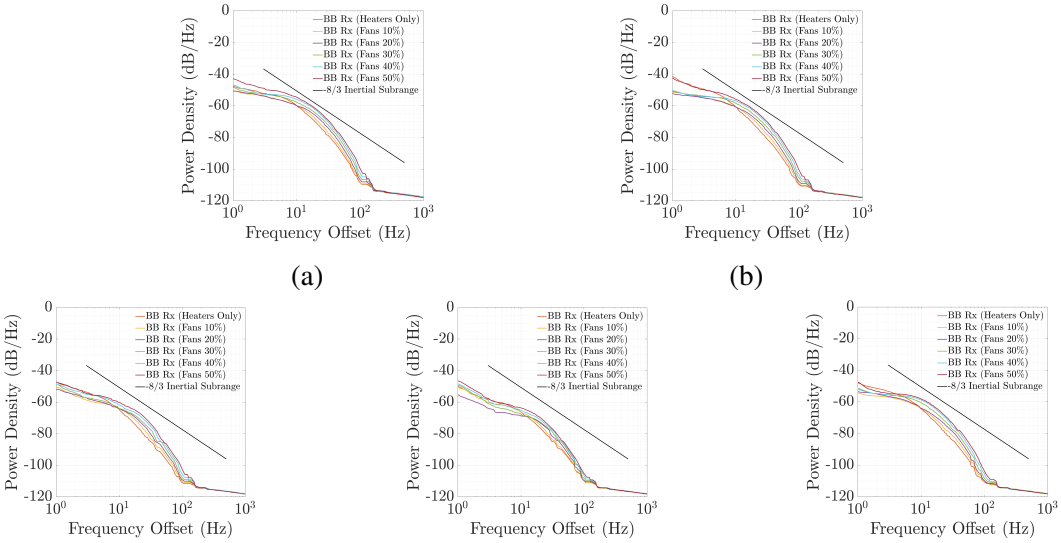

Figure A.3: PSD measurement results for heaters elevated in front and evenly spaced out with the following heaters turned on: (a) all, (b) left and right, (c) left, (d) center, and (e) right. The results show negligible differences between cases (a) and (b). In contrast, cases (c) and (e) exhibit a 5dB reduction in the scintillation PSD, while case (d) results in an 8dB reduction. This suggests that the center heater produces less heat than the outer heaters. The lack of significant increase in scintillation in (a) compared to Fig. 5.22 indicates that the scintillation is primarily induced by temperature gradients orthogonal to the propagation path.

A.3 Heaters Aside and Closer

The main disadvantage of performing experiments with heaters on the sides of the FAWT is the non-uniformity created in the flow along the beam propagation path. As seen in the temperature profile measurements, the temperature gradient is strongest at the edges of the FAWT closer to the heaters, while the center is significantly lower. To try and mitigate this, tests were done by bringing the heaters closer together, to try and create a more uniform flow. The disadvantage of doing this is that the propagation distance in which there is a temperature gradient to induce scintillation is reduced. This results in less observable scintillation, which is shown as the heaters get closer and closer together (Fig. A.4).

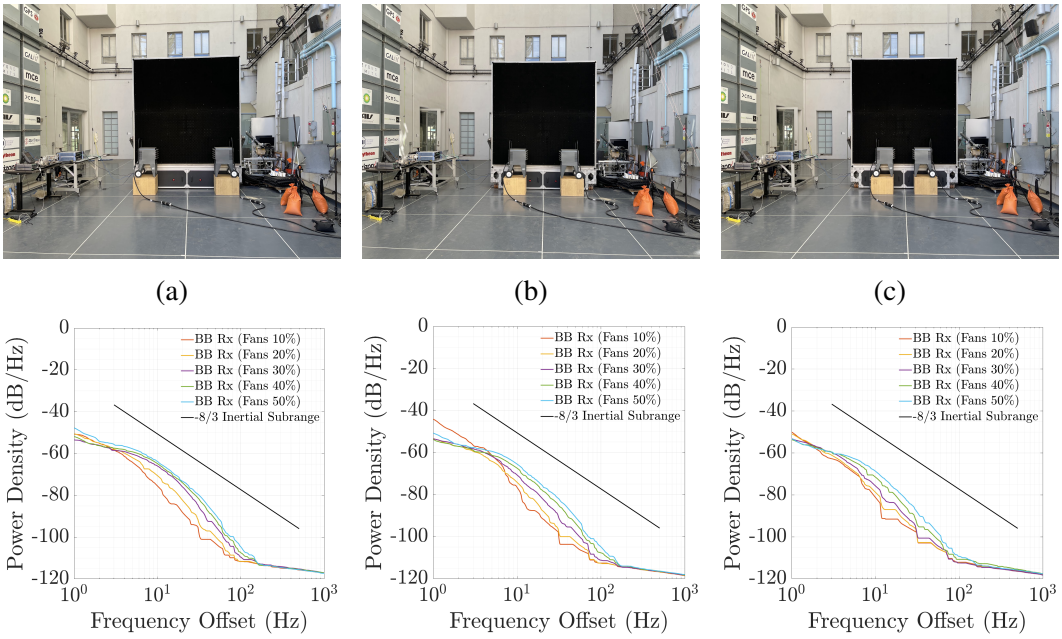

Figure A.4: Experimental setup for heaters aside positioned closer together using (a) center 18 fans, (b) center 12 fans, and (c) center 6 fans. The corresponding PSD measurements for (d) center 18 fans, (e) center 12 fans, and (f) center 6 fans, with inertial subrange -8/3 slope included for comparison.

A.4 Multi-Day Experiments

The measurement results of the multiple-day experiments demonstrate the consistency and repeatability in this laboratory setup. Since these measurements were performed further downstream compared to the main 'Heaters Aside' measurements (Fig. 5.26), the observed scintillation is reduced (Fig. A.5).

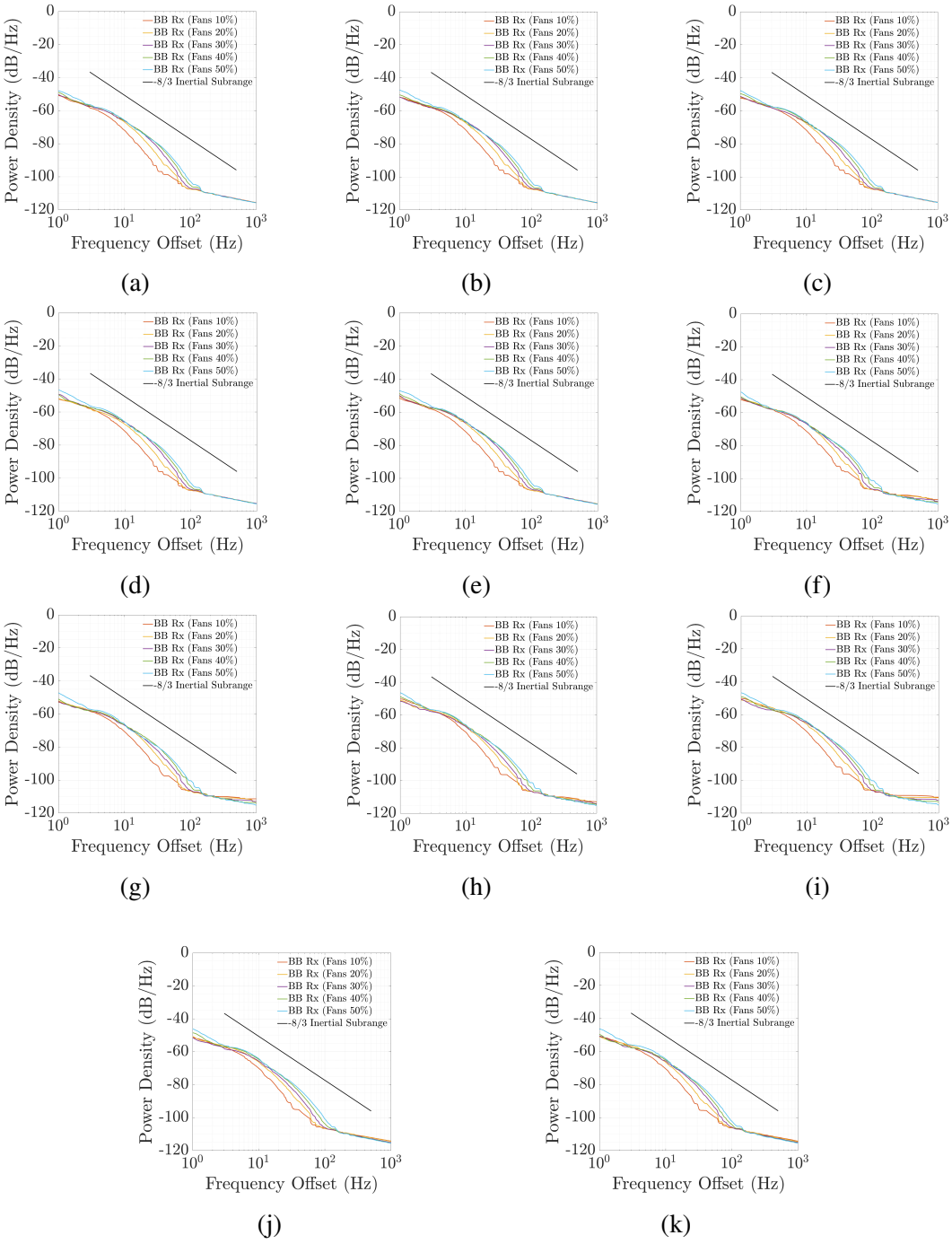

Figure A.5: Measurement results of PSD for heaters aside across multiple days showing consistency and repeatability of experimental setup. Each trace has the floor filter applied, and the inertial subrange is included for comparison. The results shown are for (a) day 1 experiment 1, (b) day 1 experiment 2, (c) day 1 experiment 3, (d) day 1 experiment 4, (e) day 1 experiment 5, (f) day 2 experiment 1, (g) day 3 experiment 1, (h) day 3 experiment 2, (i) day 4 experiment 1, (j) day 5 experiment 1, and (k) day 6 experiment 1.

A.5 Heaters in Front at Different Positions Downstream

The evaluate the changing flow dynamics when the heaters are elevated in front of the FAWT, measurements are made in 6 positions downstream (Fig. A.6). Corresponding PSD measurements using the SA (Fig. A.8) and temperature measurements using the plastic thermal screen and IR camera (Fig. A.7) are conducted.

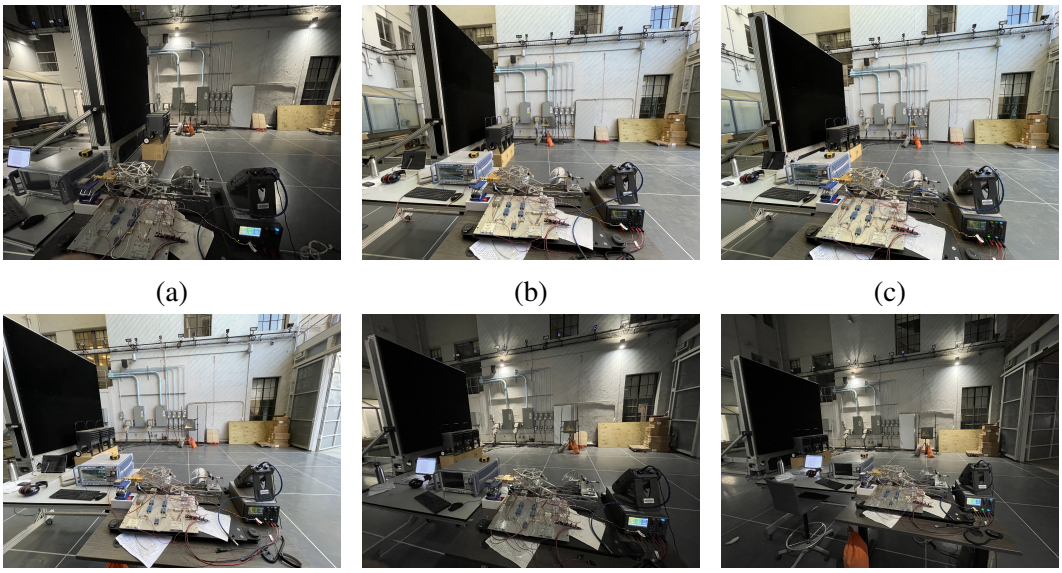

(a) (b) (c)

(d) (e) (f)

Figure A.6: Experimental setup with heaters in front and transceiver at 6 positions: (a) 0.7m, (b) 1.46m, (c) 2.22m, (d) 2.98m, (e) 3.74m, and (f) 4.5m downstream.

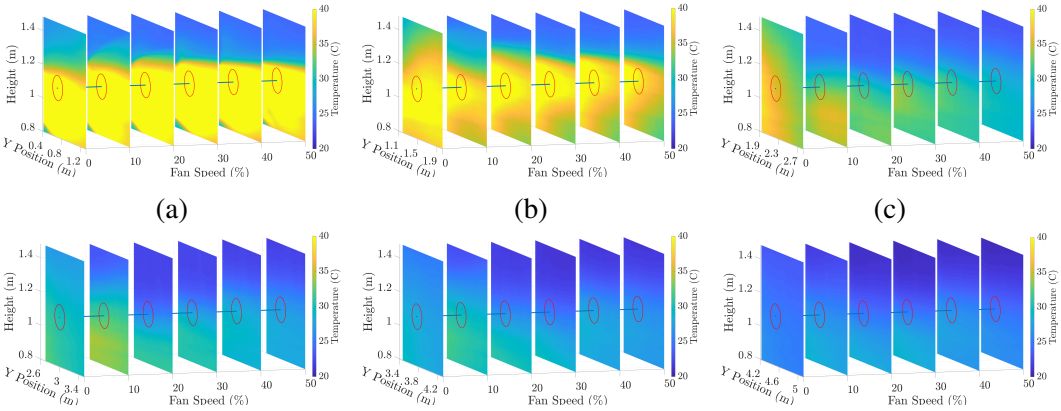

(a) (b) (c)

(d) (e) (f)

Figure A.7: Temperature measurement results with heaters in front for different FAWT intensities and transceiver at 6 positions: (a) 0.7m, (b) 1.46m, (c) 2.22m, (d) 2.98m, (e) 3.74m, and (f) 4.5m downstream.

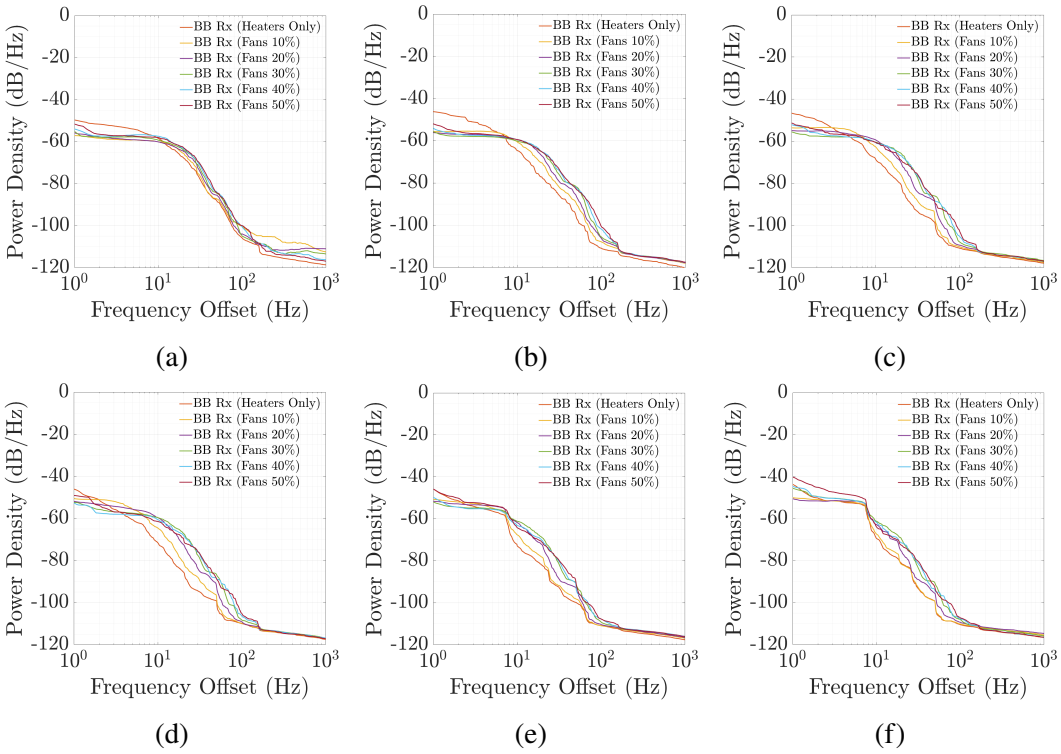

Figure A.8: PSD measurement results with heaters in front for different FAWT intensities and transceiver at 6 positions: (a) 0.7m, (b) 1.46m, (c) 2.22m, (d) 2.98m, (e) 3.74m, and (f) 4.5m downstream. The traces have a 20% smoothing filter applied, which suppresses spurious artifacts but also causes the PSD to appear less natural. Measurement results indicate decreasing scintillation at positions farther downstream, consistent with the reduction in temperature gradients. Mechanical vibration effects become more pronounced downstream, as both the transceiver and trihedral reflector are increasingly affected by the spreading FAWT flow.

A.6 Heaters on Ground

Additional experiments were done with the heaters are placed on the ground in front of the FAWT (Fig. A.9). Temperature measurements are made with the plastic thermal screen and IR camera (Fig. A.10), and the value of C_n^2 is calculated using the temperature gradients in the region the beam is propagated (Fig. A.11). The corresponding PSD measurements from the FSPN are made for various FAWT intensities (Fig. A.12).

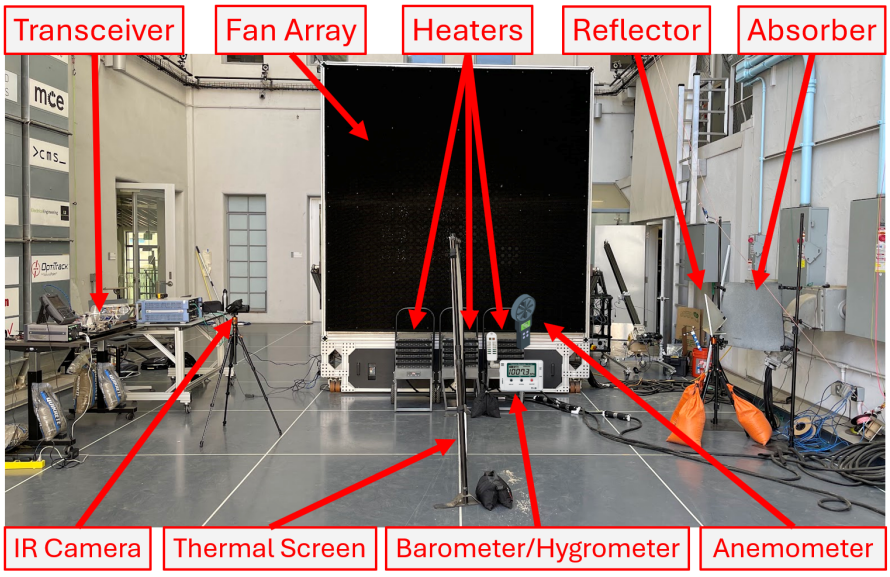

Figure A.9: Experimental setup in CAST with heaters placed on the ground in front of the FAWT with fins pointed up, along with (i) the transceiver, reflector, and absorber, (ii) IR camera and plastic thermal screen for temperature measurements, and (iii) other meteorological sensors for pressure, humidity, and wind speed measurements. Placing the heaters on the ground ensures they do not obstruct the flow from the FAWT, while keeping the hot air flow more uniform along the length of the FAWT. Each heater has fins that are angled upwards to allow the heat flow to be across the propagation path of the beam.

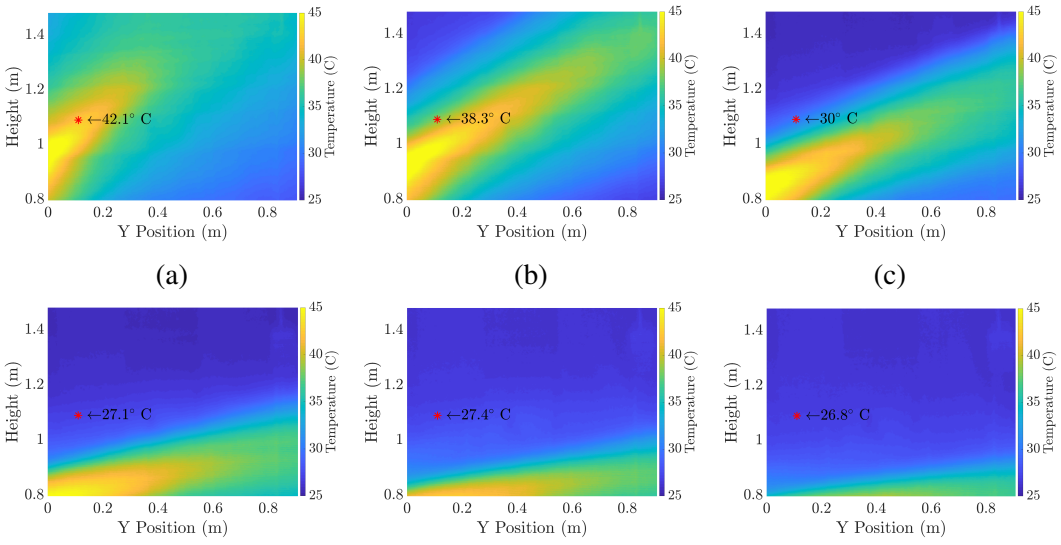

Figure A.10: Temperature measurements with heaters on the ground for FAWT intensities of (a) 0%, (b) 10%, (c) 20%, (d) 30%, (e) 40%, and (f) 50%. The red asterisk marks propagation path of the beam and the corresponding temperature. Measurement results show that, as the intensity increases, the flow from the FAWT dominates and pushes the hot air downward, out of the path of the beam.

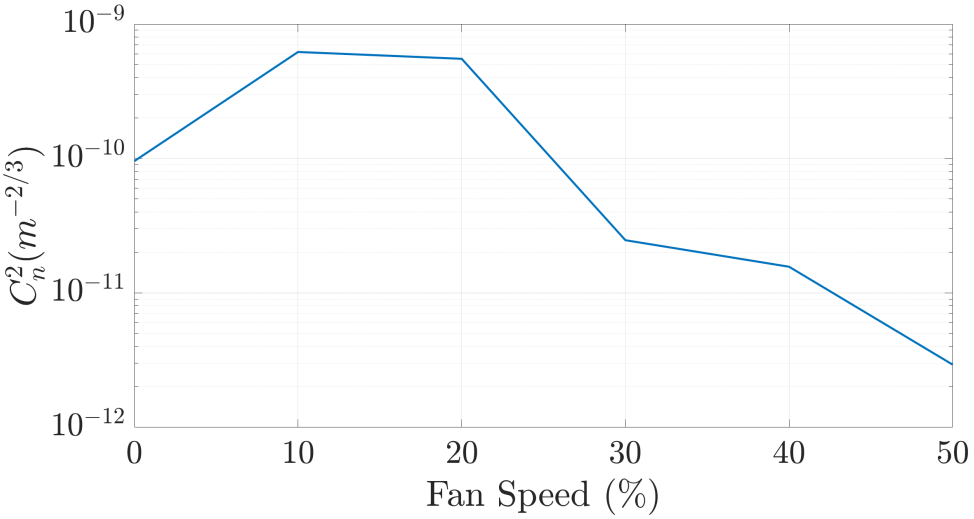

Figure A.11: Estimate of C_n^2 for different FAWT intensities with heaters on the ground, calculated using the gradient model (Eq. 3.14). For FAWT intensities above 20%, the reduced temperature gradient results in lower C_n^2 values.

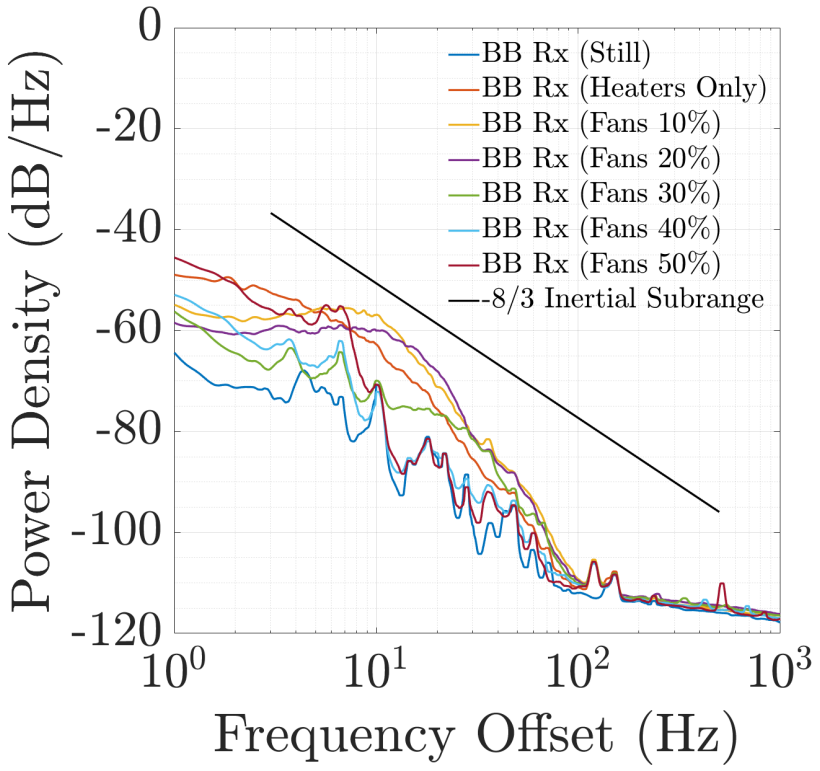

Figure A.12: PSD measurements with heaters on the ground in front of the FAWT. For the lower FAWT intensities of 10-20%, expected behavior occurs with the scintillation pushing the PSD curve towards higher frequencies. As the FAWT intensity increases to 30% and above, there is a reduction in the scintillation due to the lower temperature gradient, and mechanical vibrations are more pronounced for frequencies below 7Hz. Inertial subrange with -8/3 slope is included for comparison.